Advances in Astronomy

Challenges and Perspectives of Space Situational Awareness

Lead Guest Editor: Maria Gritsevich
Guest Editors: Michael Küppers, Elizabeth Silber, Juraj Tóth, and Josep M. Trigo-Rodríguez

Challenges and Perspectives of Space Situational Awareness

Advances in Astronomy

Challenges and Perspectives of Space Situational Awareness

Lead Guest Editor: Maria Gritsevich
Guest Editors: Michael Küppers, Elizabeth Silber, Juraj Tóth, and Josep M. Trigo-Rodríguez

Contents

Modeling of the Dark Phase of Flight and the Impact Area for Meteorites of Real Shapes
Karol Havrila, Juraj Tóth, and Leonard Kornoš
Research Article (14 pages), Article ID 5530540, Volume 2021 (2021)

On the Mass Distribution of Fragments of an Asteroid Disrupted in the Earth's Atmosphere
Irina G. Brykina and Lidia A. Egorova
Research Article (13 pages), Article ID 9914717, Volume 2021 (2021)

A Numerical Approach to Study Ablation of Large Bolides: Application to Chelyabinsk
Josep M. Trigo-Rodríguez, Joan Dergham, Maria Gritsevich, Esko Lyytinen, Elizabeth A. Silber, and Iwan P. Williams
Research Article (13 pages), Article ID 8852772, Volume 2021 (2021)

Assessment of Near-Earth Asteroid Deflection Techniques via Spherical Fuzzy Sets
M. Fernández-Martínez and J. M. Sánchez-Lozano
Research Article (12 pages), Article ID 6678056, Volume 2021 (2021)

Hindawi
Advances in Astronomy
Volume 2021, Article ID 5530540, 14 pages
https://doi.org/10.1155/2021/5530540

Research Article

Modeling of the Dark Phase of Flight and the Impact Area for Meteorites of Real Shapes

Karol Havrila, Juraj Tóth, and Leonard Kornoš

Faculty of Mathematics, Physics and Informatics of Comenius University in Bratislava, Bratislava, Slovakia

Correspondence should be addressed to Juraj Tóth; juraj.toth@fmph.uniba.sk

Received 28 January 2021; Revised 5 May 2021; Accepted 5 November 2021; Published 23 December 2021

Academic Editor: Kovacs Tamas

Aims. The complex dynamics of bodies, originating from the interplanetary matter and passing through Earth's atmosphere, defines their further position, velocity, and final location on Earth's surface in the form of meteorites. One of the important factors that affect the movement of a body in the atmosphere is its shape and orientation. Our goal is to model the interaction of real shape meteoroids with Earth's atmosphere and compare the results with the standard spherical body approach. *Methods*. In the simulation, we use 3D models of fragments of the Košice meteorite with different sizes and shapes. Using a 3D model of fragments, we consider the real shape of the body to define its resistance properties during atmospheric transition more specifically. The simulation is performed using virtual wind tunnel in the MicroCFD (Computational Fluid Dynamics) software to obtain more realistic drag coefficients and using the μ(m)-Trajectory software to model the particle trajectory in the atmosphere including the wind profile. The final outputs from these programs are the drag coefficient as a function of the altitude and the particle orientation. Using these parameters we get the more realistic body trajectory and the impact area coordinates. Comparison of the results for real and spherical model meteorite impact location is discussed. *Results*. Simulation showed significant differences in trajectory and the impact area for the different real body orientations compared to the spherically symmetric body. Also, an important result is a difference in the impact area of the real body with a specific orientation without rotation and the body with considered rotation. The significant difference between the modeled impact of a real shape body and its real place of finding compared to a spherically symmetric body indicates the importance of the method used.

1. Introduction

The components of interplanetary matter are rich sources of information that serves to describe and better understand the processes associated with the origin, evolution, structure, and dynamics of the Solar System bodies. Material from meteorites falls is still rare and its collection is important for subsequent study of physical, mineralogical, and chemical properties. The study of the meteorites is dependent on the instrumental records and following the effective determination of impact area and their recoveries.

The interaction of a meteoroid with Earth's atmosphere is associated with several phenomena related to the 4 regimes of the atmospheric motion: preheating, ablation, dark flight, and impact. An important phenomenon accompanying preheating and ablation is ionization. The dark phase of flight and impact are characterized by nonemission of radiation [1]. Based on this is a description of dynamic, geometric, and physical properties of meteoroid, during the interaction with the atmosphere, determined from instrumental observations. Detailed physical procedures and models are given in Ceplecha [2] which includes a description of a meteorite fall originating from the observation of a fireball. Despite the fact that we have tens of thousands of cataloged meteorites, there are only 38 meteorites with known heliocentric orbit, by October 2021 (https://www.meteoriteorbits.info/, Meteoritical Bulletin Database). Since 1959, there have been significant cases such as Přibram, the first meteorite with the known heliocentric orbit [3, 4], Almahata Sitta, observed before entering to the atmosphere [5], Križevci, the first meteorite fall determined from video observations with the most accurately known orbit [6], Chelyabinsk, the largest meteorite with the known heliocentric orbit [7], Neuschwanstein, almost identical orbit with the meteoroid Přibram [4], and others.

In this study, we used a detailed documented and analyzed case of the Košice meteorite fall [8] on February 28, 2010, in the area west of the town Košice in eastern Slovakia. Its trajectory, fragmentation model, orbit definition, and impact area of fragments are given in Borovička et al. [8]. A detailed analysis of the impact area is given in Tóth et al. [9]. Subsequently, the material and magnetic properties (density, porosity, magnetic susceptibility) of the Košice meteorite fragments were defined [10]. Spectroscopic analysis to determine the presence of iron-containing compounds was discussed in Sitek et al. [11]. Statistical analysis of the mass distribution for fragments can be found in Gritsevich et al. [12] and Betzler and Borges [13].

The aim of our study is to obtain more realistic shape of trajectories and impact locations of individual fragments, using dynamic interaction of the lowest part of the planetary atmosphere (the dark phase of flight) with 3D models of fragments of the Košice meteorite. The first analyses of this issue were discussed in our previous work [14, 15]. The study was done by using two software tools. To determine the resistance properties of a real body model we use the virtual wind tunnel MicroCFD. To define the shape of the trajectory during the dark phase of flight and the individual places of impact of the fragments we use the μ(m)-Trajectory program, our own software.

In the paper, we analyze the resistance properties, the drag coefficient Γ of the three real 3D scans of meteorites of different sizes and shapes (for masses of different orders, ~2000 g, ~200 g, and ~20 g). We compare the dynamic properties of the used real shapes of meteorite fragments with the standard approach from Ceplecha [2]; in which a symmetrical body shape with corresponding resistance properties is used. At the same time, we compare the places of impact obtained by the Borovička [8] model for the Košice case with the impact area of bodies with real shapes obtained by our simulations.

2. The Dark Phase of Flight

Defining the shape of meteoroid trajectory and impact area is based on the dark phase of flight modeling. Modeling of the lowest flight phase or dark phase of flight is based on a mathematical model by Ceplecha [2]. During this part of trajectory, the body and its fragments cease to emit radiation and move on ballistic trajectories under the influence of gravity and interaction with Earth's atmosphere. The body's velocity during the dark phase of flight is in the order of hundreds to tens of ms^{-1} and is significantly lower than its entry velocity. The wind field in individual level of altitudes has a significant effect on the body motion during this phase. The result of this effect is a change of the original direction of flight. The typical impact areas have dimensions of several km^2. In addition, the dark flight phase is affected by the body shape [1].

3. The Drag Force and Determination of the Drag Coefficient Γ

The study of fluid flow around the body was first investigated by Sir Isaac Newton in "Principia Mathematica" [16], where he expected a direct dependence of the fluid resistance and velocity of a moving body. Empirical studies by Stokes and Navier expanded this issue and created a set of laws of motion in a real fluid [17]. One of these laws defines the term drag force. The drag force is a resistance of the liquid or gas acting opposite to the relative motion of the body with respect to a surrounding fluid. It is well described by Newton's law (in the case of supersonic velocities by Modified Newton's law, Figure 1) and it depends on the fluid flow velocity or the relative velocity of the body [18]. The drag force is proportional to the velocity of the body for a laminar flow and the squared velocity for a turbulent flow [19, 20]. Laminar or turbulent fluid flow around a body is defined by a dimensionless variable, the Reynolds number Re, which correlates the ratio of inertial and viscous forces acting in the flow [21]. During the dark phase of flight, there is a significant change in the velocity of the meteoroid and it is necessary to take into account a broad interval of the Reynolds number. Based on experiments that analyzed the supersonic flow of fluid or air around a smooth sphere, the Reynolds number is in the interval 10^5–10^6 which represents strong turbulent flow and low viscosity [22]. Based on Newton's theory, the drag force for turbulent flow is defined as

$$F_d = \frac{1}{2}\rho u^2 \Gamma S, \tag{1}$$

where F_d is a drag force that is identical to the relative direction flow of the fluid, ρ is a density of the fluid present, u describes the relative velocity of the body with respect to a surrounding fluid, S is effective cross section, and Γ is the drag coefficient. The drag coefficient is a dimensionless quantity that is used to quantify the resistance of an object in a fluid and it is always associated with a particular surface area. The value of the drag coefficient depends on the relative velocity, orientation, and size of the body, density of the fluid present, and its viscosity [21]. We can rewrite equation (1) in the form

$$\Gamma(M) = \frac{2F_d}{\rho u^2 S}. \tag{2}$$

Equation (2) expresses the calculation of the value of the drag coefficient using the drag force. In the case of a meteorite flight through the atmosphere, the resistance properties are described by the value of the drag coefficient Γ as a function of the velocity in Mach (M) (equation (2)).

The standard model is based on certain approximations where the symmetrical shape of the body with a tabulated function of the drag coefficient (Table 1) and without rotation is considered [2]. However, most models use a constant drag coefficient Γ of 0.7, when describing meteorite falls with relatively good results (e.g., [8]). It should be remembered that the experimental data indicate the drag coefficient as a strong function of the Mach number, especially in the low supersonic and subsonic regimes [23, 24]. The search for a useful fit for this experimental data is discussed in Carter et al. [25] (see Figure 1). Experiments that define the dependence of the drag coefficient with the Reynolds number for a smooth sphere [22] are fitted in the article of Morrison [26].

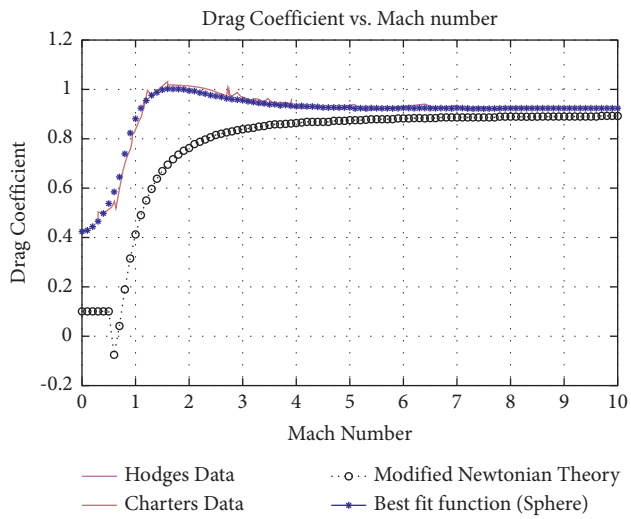

Figure 1: Drag coefficient as a function of Mach number for a sphere, the solid lines are data from two experiments designed to find the drag coefficient of smooth spheres at different Mach numbers [23, 24], the dotted blue line is the best fit function, and the line of circles is Modified Newtonian Theory [25].

Table 1: The drag coefficient Γ depending on the body speed in Mach (M) units for symmetrical shape of the body without rotation, rewritten to the table form [2].

Γ	0.328	0.351	0.389	0.441	0.504	0.552	0.596	0.632	0.618	0.580
v (M)	0.2	0.4	0.6	0.8	1	1.2	1.5	2	3	4

In our study, in the first step we focus on the use of a spherically symmetric body and constant value of the drag coefficient Γ of 0.7, and then using the steps given in Section 5, we obtain real values of the drag coefficient for real shapes of meteorites.

4. Used Software

An important factor in describing of the meteoroid dynamics during the dark phase of flight is the body shape and its rotation and orientation. The result of the specific shape of the body for a given altitude and orientation in the flight's direction is a specific value of the drag coefficient Γ. Its value or the value of the drag force can be obtained by simulating real physical conditions during the body flight through the atmosphere. For this purpose is used a virtual wind tunnel and in this paper we use the commercial program *MicroCFD* (Computational Fluid Dynamics, https://www.microcfd.com/). The functionality of the program, the physical background, practical testing, and its use are described in detail in the articles of Rohde [27–30]. The calculated values of the drag coefficient Γ as a function of altitude enter into calculation of the dark phase of flight model.

The virtual wind tunnel *MicroCFD* (Figure 2) simulates the interaction of flowing air (with realistic viscosity) with 3D models of bodies. In the interaction, it is assumed a high Reynolds number and turbulence. The input files are 3D stereolithographic models of type.stl (standard CAD format). The surface of the body in this format is made up of individual triangulating shapes. A 3D model of a real body is created by scanning of meteorite fragment over a full 360° circle with the specific angular step using tomography equipment [31]. The input parameters to the MicroCFD program are the velocity of air flow in Mach units, the fluid pressure in hPa, the temperature in K, the gas constant that describes the type of gas used for the simulation, and its average specific heat. The values of the input parameters are directly related to atmospheric conditions at selected altitudes.

The simulations in the virtual wind tunnel are taking place in lower atmosphere under 30 km. As the output of the simulation are the values of the drag force acting on the body resolved into three orthogonal components X, Y, and Z. The resulting force is the sum of aerodynamic forces acting on individual triangulating areas of the 3D body model, where their mutual orientation is considered [32]. We also obtain moment of forces acting in three orthogonal components X, Y, and Z and effective cross section of the body in two perspectives (XY, YZ).

The second software used in this work is the μ(m)-Trajectory program (Figure 3). It is a complex tool with a user interface, created in Python by the first author of the paper. The program computes the motion of a body in the atmosphere, in three orthogonal components based on the aerodynamic model of the dark phase of flight [2]. The program also works with the changing values of the drag coefficient as a function of altitude and thus enables use of the wind tunnel results.

While the standard aerodynamic model is based on the change of the body motion as a function of altitude,

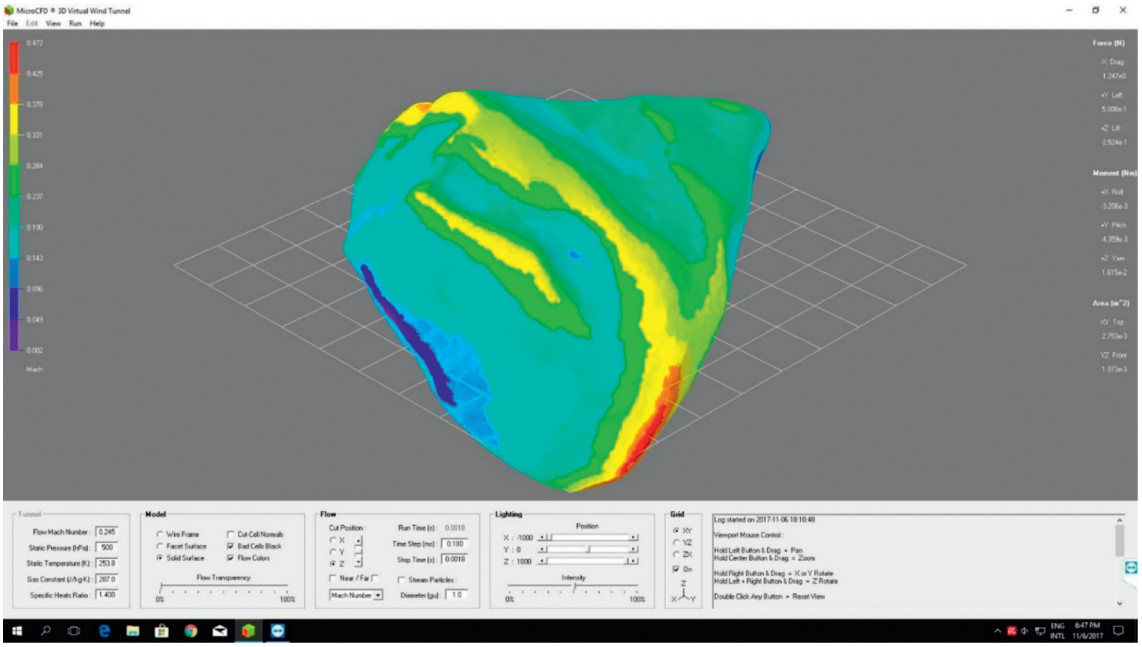

Figure 2: The MicroCFD (Computing Fluid Dynamics) software interface, which simulates conditions of supersonic flow around the body in virtual wind tunnel (http://microcfd.com/index.htm). Graphical and numerical representation of the results of drag force and moment of force for a 3D model of a real-shaped body [14].

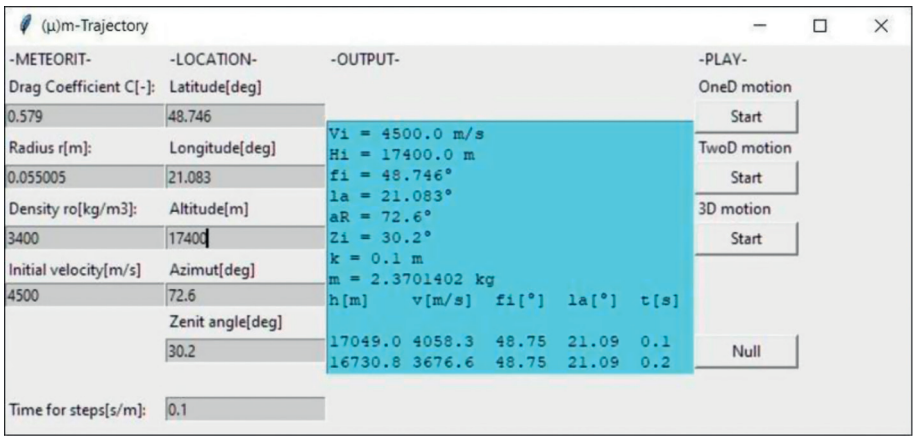

Figure 3: User interface of the μ(m)-Trajectory program with input variables and modeled values in the "output" window.

for our needs we use equations rewritten as a function of time. The primary part of the model is the equations of motion defining the change of the three orthogonal components of velocity over time. The equations of motion include gravitational and wind effects on the body, considering the presence of the Coriolis force. For each integration step, the length of the body's trajectory, the change of its geographical coordinates, and the change of its azimuth and zenith distance are calculated [2]. Our tests showed that an integration step size of 0.1 seconds is sufficient for the accuracy of the calculation. The simulation of the body motion, based on aerodynamic equations, uses the numerical method of Runge-Kutta of 4th order.

The program uses data from the MSIS-E-90 atmosphere model [33] and from University of Wyoming server (http://weather.uwyo.edu/) downloads wind altitude profiles nearest to the meteorite fall. Initial variables define location in the atmosphere (latitude, longitude, and altitude), azimuth, zenith angle, and physical conditions of the meteoroid in the beginning point of the dark phase of flight (initial velocity, density, and radius of the meteorite body). At the same time, the integration step, the body rotation velocity (if considered), and value of the drag coefficient are defined (constant or variable value). The output of the program provides data such as body position and its velocity for each integration step, the geographic coordinates of the impact area, and a graphical representation of trajectory and impact directly in Google Earth application.

5. Procedure

The simulation goes in two iterations steps, which we will call first (I.) and second (II.):

(1) We enter to the first iteration step (I.) with a symmetrical body in the form of a sphere. From the known volume and density of the fragment [10], the radius r for the spherical shape of the body with a mass equivalent to the real meteorite entered to the μ(m)-Trajectory program is determined.

(2) In the μ(m)-Trajectory program, parameters of the dark phase of flight for the spherical model are calculated using the input values (wind field, atmosphere, position of the body, etc.), the velocity of the body in the beginning point of the dark phase of flight, and the drag coefficient Γ for the spherical body.

(3) Due to unusually long calculation time in MicroCFD software (in the order of hours), three to four altitudes are selected from the dark phase model based on point 2. For each altitude, based on the model, we know the velocity of the body and we can determine the density of the atmosphere. For these selected parameters, new values of the drag coefficient Γ are determined (Section 3) using the MicroCFD wind tunnel, where 3D models of real fragment are used instead of the spherical body. This method provides more accurate values of the drag coefficient Γ for different orientations of the body during a flight.

(4) The new values of the drag coefficient Γ, for each orientation of the body, are plotted as the function of altitude, Γ(h) (e.g., Figure 4), fitted by the least squares method.

(5) We enter to the second iteration step (II.), where the new parameters of the dark phase with more precise velocity at specific altitude are calculated again using the μ(m)-Trajectory program. In this step, into the calculation enter the values of the drag coefficient obtained from the function Γ(h) (point 4). Optionally, we can define the period of the body rotation.

(6) The simulation process is repeated once again in points 3 to 5, where to the point 3 are entered the new velocities of the body in selected altitudes.

This procedure ensures the improving of the value of the drag coefficient Γ, obtaining the function Γ(h) for all defined orientations of the real 3D model of the body and impact area for the individual orientations of the fragments on the trajectory.

In the MicroCFD we create simulations of the drag coefficient in six orientations for each fragment. The first three orientations are in the direction of the X, Y, and Z axes of the body, and the remaining are in the opposite directions, which will be referred to as IX, IY, and IZ. For conditions in the specific altitude of the atmosphere, we simulate the value of the drag coefficient for four altitudes and in different orientations. So for each meteorite fragment we performed 24 simulations (6 orientations × 4 altitudes).

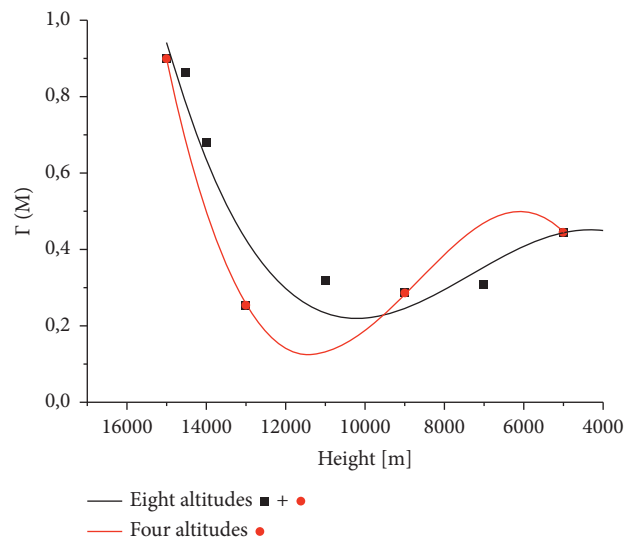

Figure 4: Comparison of the obtained curves for different selection of altitudes for the fragment no. 21 (208 g with orientation in the X axis direction, polynomial fit of the 3rd degree for default four altitudes (red curve) and for selected eight altitudes (black curve)).

At the output of the μ(m)-Trajectory we get an impact area composed of the individual impacts relating to the orientations of the body X, Y, Z, IX, IY, IZ. In addition, we obtain two impact locations for the simulated rotation of the body (links with the period of the body angular velocity, point 5) in gradual (REG) and random (RAN) setting of individual orientations in one-second interval. In this procedure, for each meteorite, we obtain at the output one impact point for the spherical body from the first iteration step (I), six impact points for individual orientations of the real body model, and two impact points for REG and RAN rotation of the real body model from the second iteration step (II).

6. Input Parameters and Used 3D Models

In our simulation we use three 3D models of the fragments of Košice meteorite representing three orders of mass: catalog no. 53 (23.2 g), no. 21 (208 g), and one uncatalogued fragment of 2370 g [9] (Figure 5).

The calculation of the dark phase of flight begins at the altitude in which the Košice meteoroid ceased emitting radiation (beginning point of the dark phase of flight, 17.4 km). We do not consider changing the shape of the body or its mass after entering the dark phase of flight. However, there is a continuing ablation (a very short time) after crossing the terminal point of the fireball visible by particular observing system [34]. In our simulation, we consider the beginning point of the dark phase of flight to be fixed and we do not work with additional ablation. In the future, it is necessary to define this beginning point in the altitude where the ablation process is definitively terminated. The velocity of the largest fragment in the beginning point has been estimated at 4.5 km/s [8]. For the meteorite models no. 21 and no. 53 we set the velocity in the beginning point to 2.5 km/s. This value is based

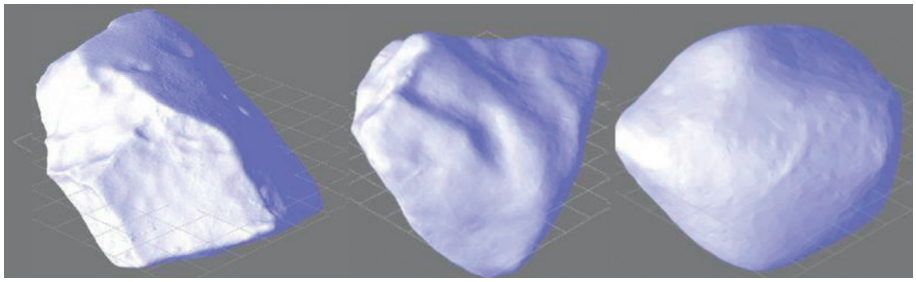

Figure 5: 3D models of meteorite Košice. In the left is the model of uncatalogued fragment (2370 g 135 × 105 × 100 mm), in the middle is model with catalog no. 21 (208 g 70 × 63 × 36 mm), and in the right is model with catalog no. 53 (23.2 g 28 × 22 × 21 mm). The model sizes in the image are not scaled.

on the fact that we cannot associate the origin of smaller fragments with a specific fragmentation, so based on Borovička et al. [8] we assume their origin at higher altitudes of the Košice fireball trajectory. Naturally, their velocity decelerated to smaller value than the velocity of the largest fragment in the beginning point of the dark phase of flight. Also, we note that the value 2.5 km/s comes from the meteoroid fragmentation model as the velocity limit for meteoroid ablation [8]. However, the presumption of the value of the initial velocity can be set arbitrary in our case, because we consider only the relative shifts of the impact points of the real body individual orientations compared to the spherical body and do not search for an absolute solution.

For the largest fragment model, we start from the original geographical position of the beginning point (48.746N, 21.083E) [8]. For the models no. 21 and no. 53, we slightly modify the real geographical location of the beginning point (at a given altitude) in order to get the closest impact point to the real place of finding the meteorite. Then we compare the relative change of dark flight simulation for spherical and real shape fragments. To determine the function of the drag coefficient Γ(h) four altitudes were chosen: 15 km, 13 km, 9 km, and 5 km.

7. Simulation Results

After performing the simulation using 3D models and passing through both iterations steps, we obtain the impact area for our meteorite fragments. For each orientation of the fragment in combination with the selected altitudes in which simulation was ongoing, we can create a function of changing the drag coefficient Γ(h) (for six different orientations). The shape of the function is obtained by fitting using the polynomial of the 2nd or 3rd degree. The choice of the fitting function in the form of a polynomial is linked with the shape of the predicted function of the drag coefficient depending on the velocity in Mach units (Figure 1). In the case of the meteorites used, the initial velocity of 4.5 km/s or 2.5 km/s represents approximately a value of 13.5 Mach or 6.5 Mach (for the altitude 17.4 km). However, in the range of altitudes of 15–13 km, the velocity of the bodies decreases to a level of approximately 1 Mach or below, which represents the left side of the function on Figure 1 and a sudden decrease in the value of the drag coefficient Γ. This is in qualitative agreement with our data depending on each individual meteorite shape and orientation. The overall physical behavior corresponds to theoretical expectations. The fitting function is based on the minimum value of root mean square deviation. Now we focus on the results of 3D models of the larger fragments in the following paragraphs.

7.1. Relevance of Fitting Function Shapes. Before moving on to simulating individual fragments, let us look at the degree of reliability of the results, using a smaller number of altitudes. To verify the objectivity of the curve shapes of individual orientations, we performed a test simulation of the body at different altitudes than the default ones (5, 9, 13, and 15 km) used. We focused on fragment no. 21 (208 g), specifically on the X orientation. Simulations were made at eight selected altitudes: 5, 7, 9, 11, 13, 14, 14.5, and 15 km. The resulting curves of the drag coefficient Γ(h) with default altitudes and new altitudes, using a polynomial of the 3rd degree (equation (3)), can be found in Figure 4.

The obtained curves in Figure 4 are slightly different. The largest relative difference between the curves of the drag coefficient Γ(h) is 0,1. This difference may be affected by the shape of the trajectory when simulating the dark phase of flight and thus change the final shape of the impact area. From the acquired results, we consider that it would be more suitable to define at least twice the number of altitudes, but based on the time-consuming simulation in the wind tunnel, we worked with default four altitudes.

7.2. Košice Meteorite, Uncatalogued Largest Fragment (2370 g). The simulation of the dark phase of flight of the largest Košice fragment was performed without complications. The resulting values of the drag coefficient Γ for 3D model of the largest fragment are given in Table 2.

For all orientation, the polynomial fitting of the 3rd degree was used (in general form, equation (3)). The obtained shape of the function is used for calculation of the values of the drag coefficient Γ in each step of the integration of the dark phase of flight (Section 5, points 4 and 5).

$$y = y_0 + B_1.x + B_2.x^2 + B_3.x^3. \quad (3)$$

The variable x represents the altitude, in which the body is located at a given time. The obtained functions of the drag

Table 2: Values of the drag coefficient Γ for individual orientation of the largest fragment of the Košice meteorite (2370 g) in selected altitudes [14].

Altitude (km)	Drag coefficient Γ for orientation					
	X	*Y*	*Z*	*IX*	*IY*	*IZ*
15	0.636	0.742	0.494	0.712	0.748	0.832
13	0.759	0.793	0.741	0.857	0.958	0.819
9	0.261	0.244	0.258	0.256	0.256	0.208
5	0.364	0.523	0.375	0.349	0.360	0.447

coefficient Γ(h) for individual orientations are plotted in Figure 6.

The shape of the drag coefficient Γ(h) curve for each orientation of the fragment has a similar character. Decreasing shape of the curve can be explained by a significant change of the fragment velocity from 1.4 km/s (15 km) to 0.3 km/s (13 km). Subsequently, at an altitude of approximately 7 km, the value of the drag coefficient increases. This increase can be explained by the transition of the fragment into a denser atmosphere. The velocity on the ground level was from 46 m/s to 53 m/s depending on the orientation.

The localisation of individual impacts for the spherical model, the model computed by Borovička et al. [8], and the body model with real shape for different orientations and rotation in prograde and retrograde mode are in Figure 7. The impact distance of the spherical model compared to the real place of the recovered fragment impact is 640 m. The impact distances of individual orientations of the body with real shape, gradual (REG), and random (RAN) rotation ranges from 340 m (orientation IY) to 490 m (orientation RAN) compared to the real place of impact. Naturally, rotation somehow averaged the atmosphere interaction with specific orientation shapes and cross sections. That is way, the RAN and REG simulations ended in the middle of 6 oriented flights. The orientation *Z* has a significantly different geographical position of the impact. In this case, we assume that the fragment was oriented to the side with the largest effective cross section. The given result points to an important influence of the orientation and the real shape of the body on the change of the trajectory and position of the impact place. It is also necessary to mention that the individual impacts of the real body keep the flight direction (with a small shift to the south).

7.3. Košice Meteorite, No. 21 (208 g). Simulation of the dark phase of flight of the Košice fragment no. 21 was successful in all aspects. The resulting values of the drag coefficient Γ for 3D model of this fragment are given in Table 3 and plotted in Figure 8.

For all orientations, the polynomial fit of the 3rd degree was again used (equation (3)). Similar to the largest fragment of the Košice meteorite, the obtained shape of the function $\Gamma(h)$ is used to calculate the values of the drag coefficient in each step of the integration of the dark flight (see Section 5, points 4 and 5).

The shape of the function for the drag coefficient Γ(h) in each orientation of the body follows a similar pattern. A significant difference between the curves can be seen in case of the *Z* and *IZ* orientation. This change in the shape of the curve and the consequence change in the values of the drag coefficient are related to a significant change of the cross section for these two orientations. We did not expect a lower value of the drag coefficient for the *IZ* orientation at an altitude of about 15 km compared to other orientations, but we assume that the conical shape for the given orientation plays a significant role. As a result there is a significantly different position of impact for *IZ* orientation (Figure 9). The value of the drag coefficient Γ from an altitude of 14 km is less than 0.5 (except for *Z* and *IZ* orientation). We see the connection in a smaller cross section compared to the study of the largest fragment. Considerable deceleration of the fragment from 2.5 km/s (altitude 17,4 km) to 0.1 km/s (altitude 15 km) resulted in decrease of the drag coefficient. The gradual transition to the denser part of the atmosphere leads to subsequent increase of the drag coefficient, which is observed approximately from an altitude of 11 km. The velocity of the fragment on the ground level was from 36 m/s to 46 m/s depending on the orientation.

The distance of the modeled impacts compared with the real position of the recovered fragment in impact area (Figure 9) is variable depending on the orientation of the fragment. The final values of individual orientations and gradual (REG) and random (RAND) rotation ranges from 440 m (orientation RAN) to 720 m (orientation *IZ*) compared to spherical body of equivalent effective cross section. The absolute differences depend on input conditions of simulations. The spread of impact area is within 1620 m with minimal side spread (few tens of meters), but the majority of impact position are within 450 meters. In Figure 9 we see maintaining of the line of the predicted direction of flight. The impacts of individual orientations in one line are generally related to the greater effect of the wind field on the less massive fragment.

7.4. Košice Meteorite, No. 53 (23.2 g). Simulation of the dark phase of flight of the Košice fragment no. 53 was also successful. For this fragment, which is close to the spherical shape, we performed 48 simulations. The resulting values of the drag coefficient Γ for 3D model of Košice fragment no. 53 are given in Table 4.

In the case of the Košice fragment no. 53, in terms of minimum value of the root mean square deviation, the polynomial fitting of the 2rd degree was used (in general form, equation 4).

$$y = y_0 + B_1.x + B_2.x^2. \quad (4)$$

Similar to the previous fragments of the Košice meteorite, the variable x in equation (4) represents the altitude of the fragment. The final drag coefficient values as a function of the altitude for individual orientation of the fragment are plotted in Figure 10.

The shape of the function for drag coefficient Γ(h) is different compared with curve shape for fragment no. 21 or the largest fragment. The drag coefficient curve has an increasing character and the value of Γ is < 0.5 in each

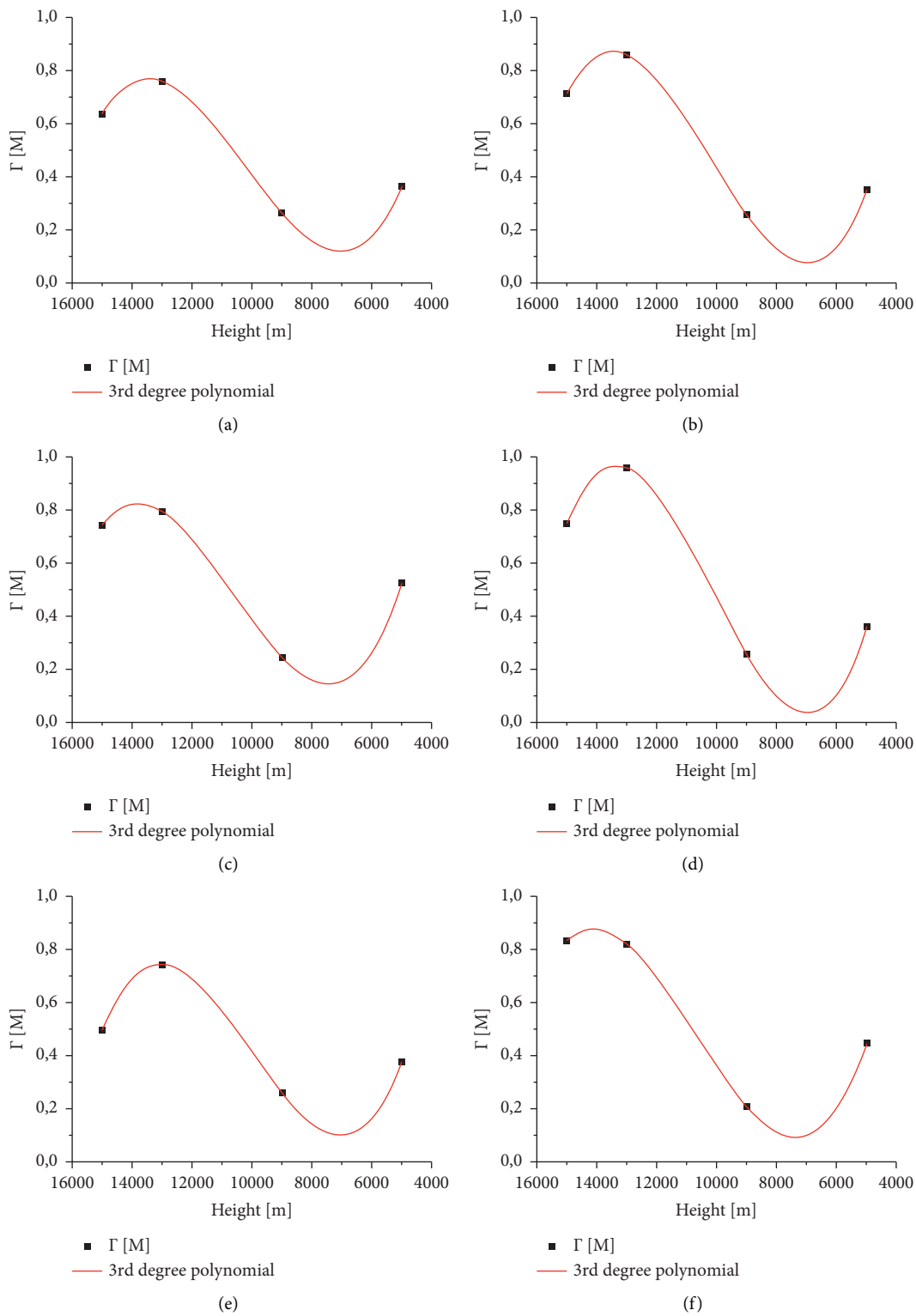

Figure 6: Dependence of drag coefficient Γ(h) on altitude change for the largest fragment of the Košice meteorite (2370 g in 6 different orientations). The graph shows the apparent variability of the drag coefficient Γ(h) when changing the altitude, where also the velocity was decreasing. (a) *X*. (b) *IX*. (c) *Y*. (d) *IY*. (e) *Z*. (f) *IZ*.

orientation. This result is due to more efficient deceleration of the smallest fragment and based on this, our simulations define the area behind the sudden decrease of the function in Figure 1. At the same time, the nearly spherical shape of the fragment leads to a lower drag coefficient value and less effective deceleration in the lower atmosphere. At an altitude of 17.4 km, the body enters into the dark phase of flight with a speed of 2.5 km/s. This value is identical to the fragment no.

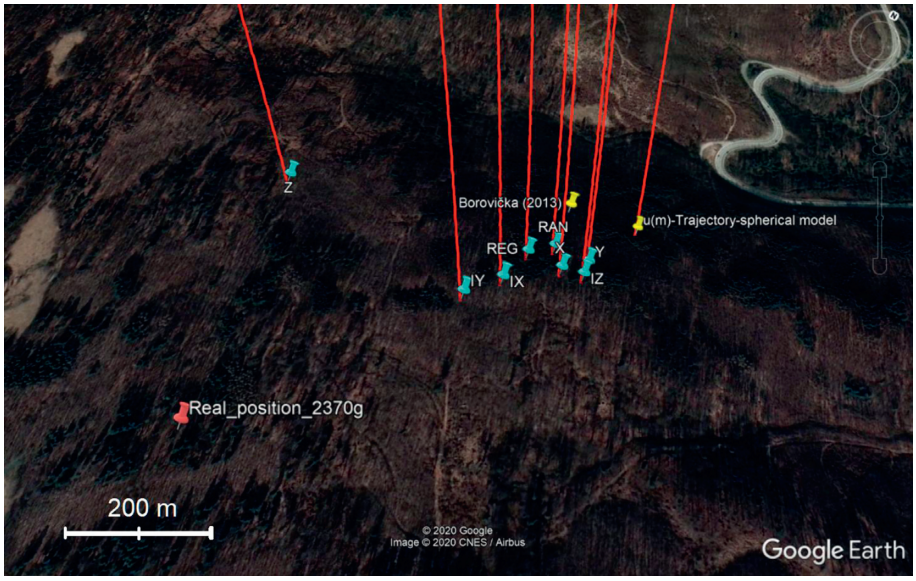

Figure 7: Detail on the impact area for the individual modeled orientations. On the left, the real place of recovered of the largest fragment of the Košice meteorite. The position of the spherical model impact (yellow) from Borovička et al. [8] and μ(m)-Trajectory program.

Table 3: Values of the drag coefficient Γ for individual orientation of the Košice fragment no. 21 (208 g) in selected altitudes [15].

Altitude (km)	Drag coefficient Γ for orientation					
	X	*Y*	*Z*	*IX*	*IY*	*IZ*
15	0.864	0.907	0.807	0.795	0.873	0.646
13	0.253	0.307	0.307	0.238	0.326	0.438
9	0.285	0.245	0.264	0.297	0.258	0.574
5	0.444	0.416	0.589	0.430	0.417	0.669

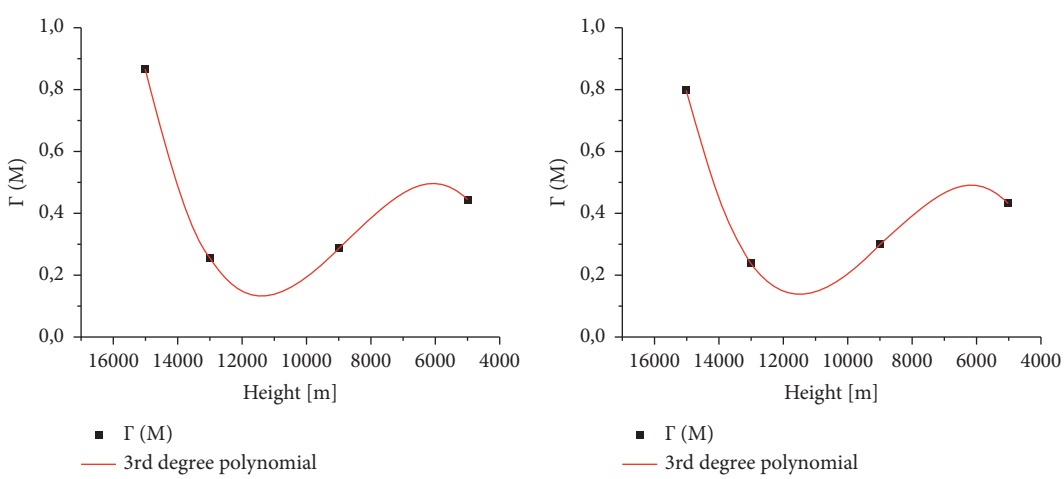

Figure 8: Continued.

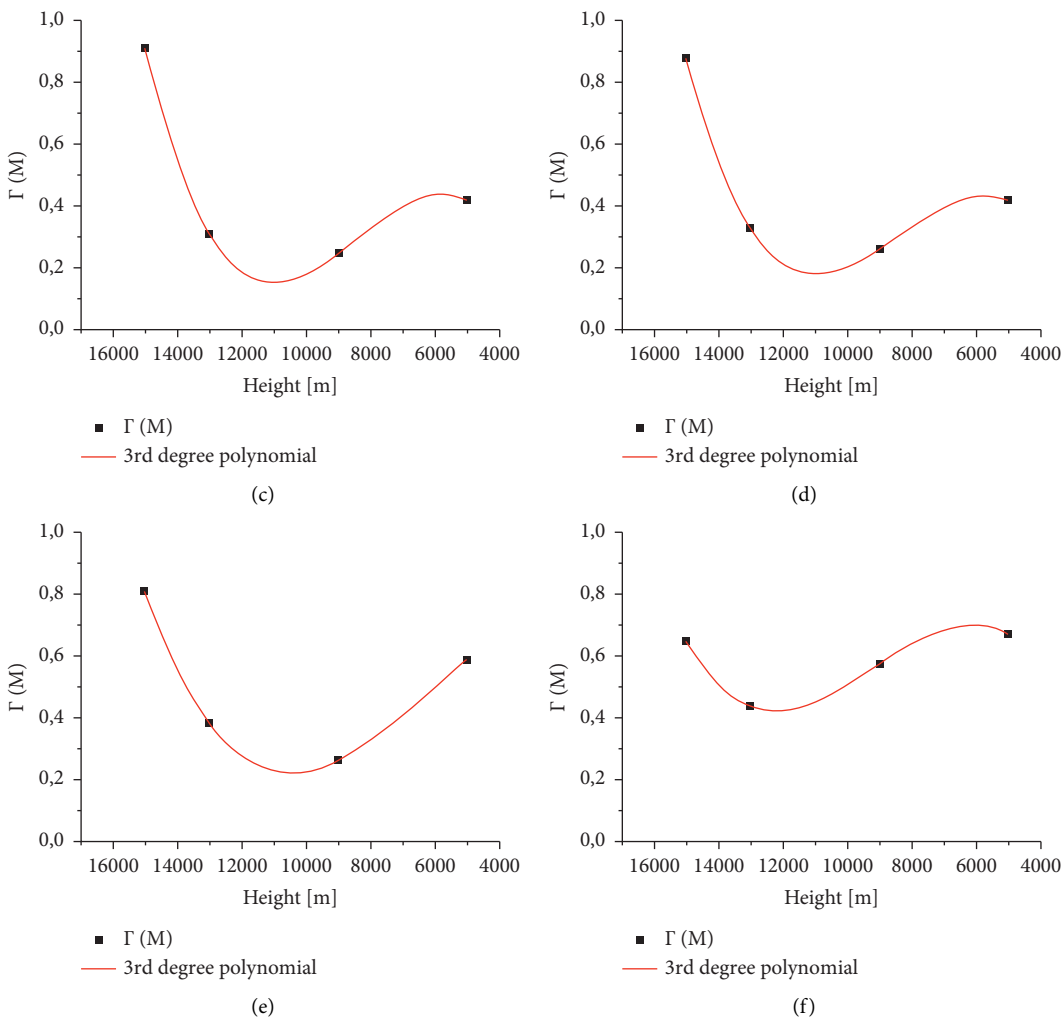

Figure 8: The drag coefficient Γ as function of altitude of the Košice fragment no. 21 (208 g) in 6 different orientations. (a) *X*. (b) *IX*. (c) *Y*. (d) *IY*. (e) *Z*. (f) *IZ*.

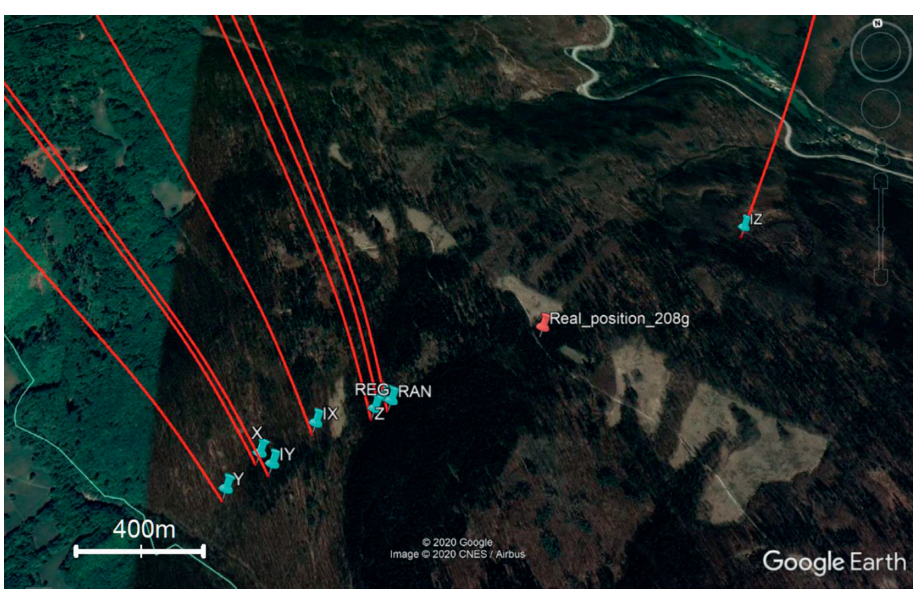

Figure 9: Detail on the shape of the impact area for the individual modeled orientations. On the right, we can see a significant shift of the impact place for orientation *IZ*, compared to other orientations. Real position of the meteorite is equivalent to spherical model position.

Table 4: Values of the drag coefficient Γ for individual orientation of the Košice fragment no. 53 (23.2 g) in selected altitudes [15].

Altitude (km)	Drag coefficient Γ for orientation					
	X	*Y*	*Z*	*IX*	*IY*	*IZ*
15	0.110	0.116	0.113	0.085	0.120	0.167
13	0.149	0.162	0.187	0.140	0.165	0.161
9	0.171	0.274	0.257	0.176	0.195	0.272
5	0.240	0.291	0.442	0.245	0.271	0.401

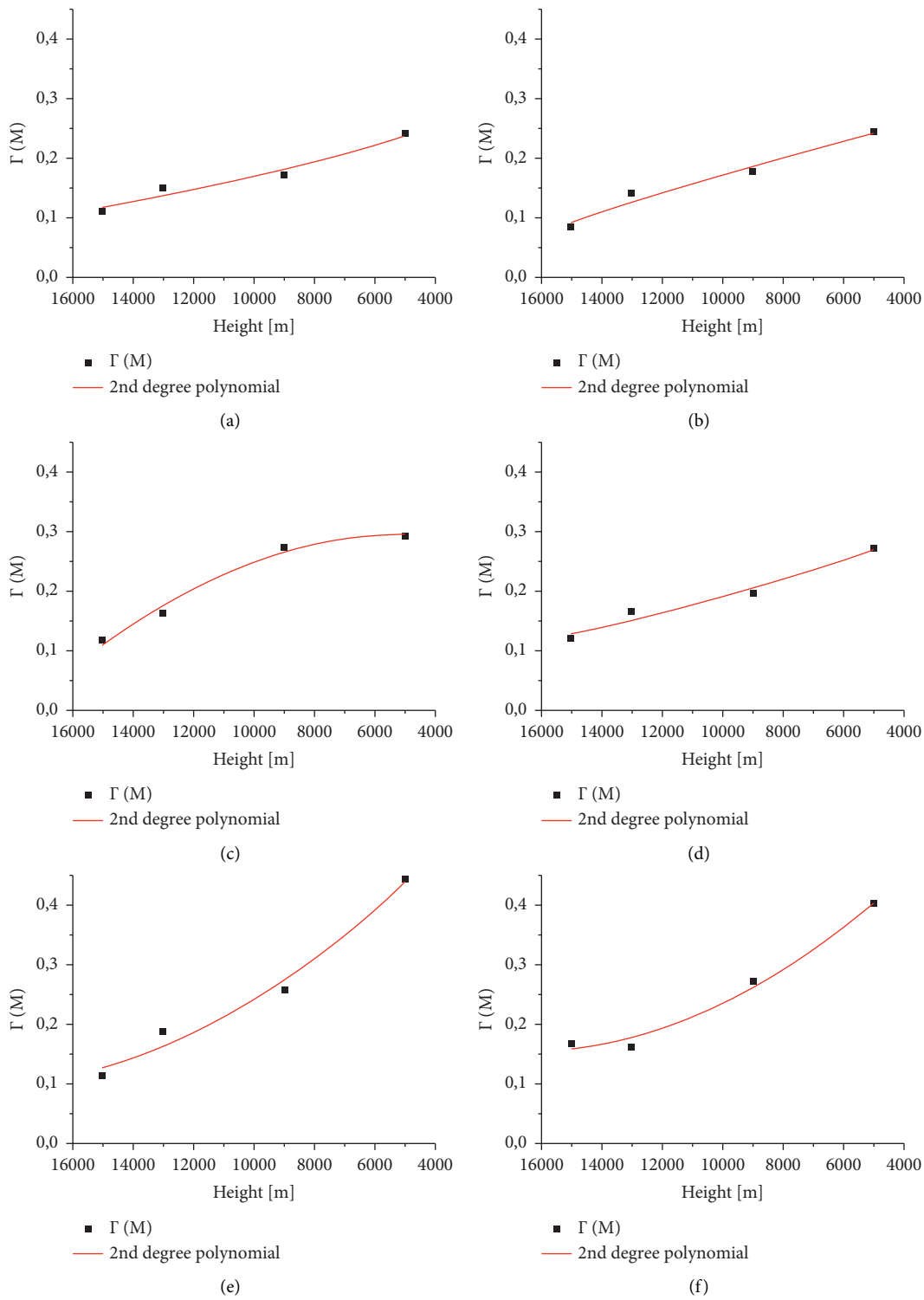

Figure 10: Dependence of drag coefficient on altitude change for fragment of meteorite Košice with catalog no. 53 (23.2 g). The graph shows the increasing value of the drag coefficient Γ when changing the altitude. (a) *X*. (b) *IX*. (c) *Y*. (d) *IY*. (e) *Z*. (f) *IZ*.

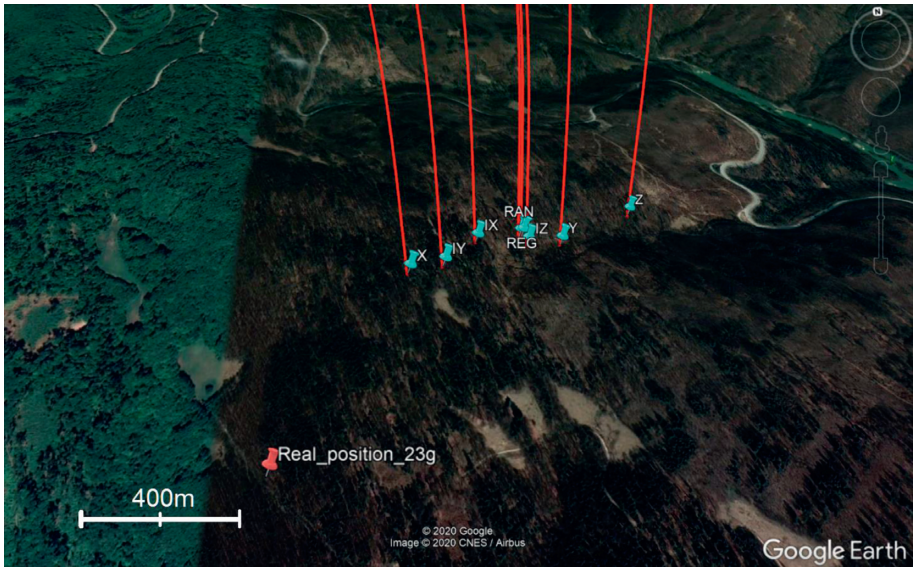

Figure 11: Detail on the impact area for the individual modeled orientations. On the left, the location of the fragment no. 53 (red) is recovered and it is equivalent to spherical model position. The impact area is located outside the line which brings together the fragment's direction of flight and real impact position.

21. However, the velocity 0.3 km/s was reached at an altitude of 13.6 km (for gradual orientation). The velocity on the ground level was from 31 m/s to 42 m/s, which is only approximately 5 m/s less than fragment no. 21.

The impact area for the individual orientations of the fragment is shown in Figure 11. Impact distances in comparison with a real position of the fragment impact (or spherical body of equivalent effective cross section) ranges from 560 m (orientation X) to 1210 m (orientation Z). In some cases, the distance between impact points for individual orientations is only a few tens of meters. This is caused by the fact that the real shape of the meteorite is close to the sphere. Similarly like in the case of the fragment no. 21, the relative spread of the individual impacts is within 680 m along the flight trajectory with minimal side spread (few tens of meters).

8. Conclusion

The aim of the study was to process, evaluate, and analyze the obtained results from simulation of the dark flight for three real shape fragments of the Košice meteorite. The simulation was fully successful for meteorite fragments, where using the MicroCFD virtual wind tunnel we have made the description of the drag coefficient Γ in 6 orientations and in different altitudes. The results of the dark phase of flight, using the μ(m)-Trajectory program, brought significant shifts of the impact area compared to the spherical shapes of the fragments, which proved the necessity of such precise simulation.

However, we must keep in mind the inaccuracies entering into the simulations of the dark phase of flight. On the one hand, from the end point of the light phase of flight, physical and location parameters enter into the simulation with standard deviations: geographical position of the body, velocity, zenith angle, azimuth, etc. On the other hand, the atmospheric conditions such as air density, wind field, and the associated drag coefficient Γ also have an impact on the overall measurement inaccuracy. These parameters come from real measurements using meteorological balloons, often tens to hundreds of kilometers away from the event, or from the meteorological models that extrapolate real data. Figure 4 also shows the different shape of the drag coefficient curves Γ(h) and as we showed it is sensitive on velocity, real shapes of meteoroids, and the choice of the number of altitudes where the simulation is performed and thus can impact results.

In general, we pointed out that used methodology in the form of simulation through several iteration steps has its importance. However, it is necessary to gradually improve this methodology and find a solution for its more effective processing. Also, it is important to process simulations for a larger number of fragments of different types, shapes, and masses. We aim to create a dataset that will contribute to the effective definition of impact areas for a wide range of meteorite falls.

In the future, to obtain the more realistic model of the dark phase of flight and the effective definition of impact area, we plan to create more functions and modifications in the program. One possibility is to generate a statistically large number of particle clones in combination with using the probability density function of random variables, kernel density estimation (KDE) [35], with the purpose of estimating the subarea of impact with the statistically highest concentration of particles and, at the same time, the use of random variations in wind speed and direction for each particle at a level ±10–20%, which are based on the uncertainties of meteorological models [34]. Finally, in the simulation, except for the use of real shapes of fragment, it is appropriate to test several empirical or theoretical models of the drag coefficient [26, 36].

Data Availability

The authors can provide background data that support the results of their study upon request.

Conflicts of Interest

The authors declare that they have no conflicts of interest.

Acknowledgments

This work was supported by the Slovak Research and Development Agency under Grant nos. APVV-16-0148 and APVV-18-0103, by the Slovak Grant Agency for Science, Grant no. VEGA 1/0596/18, and by the Grants for PhD students and young researchers at Comenius University in Bratislava, Grant no. UK/174/2019.

References

[1] Z. Ceplecha, J. Borovička, W. G. Elford et al., "Meteor phenomena and bodies," *Space Science Reviewa*, vol. 84, pp. 327–471, 1998.

[2] Z. Ceplecha, "Geometric, dynamic, orbital and photometric data on meteoroids from photographic fireball networks," *Bulletin*, vol. 38, pp. 222–234, 1987.

[3] Z. Ceplecha, "Multiple fall of Přibram meteorites photogrphes. I. Double-station photographs of the fireball and their relations to the found meteorites," *Bulletin*, vol. 12, pp. 21–47, 1961.

[4] P. Spurný, J. Oberst, and D. Heinlein, "Photographic observations of Neuschwanstein, a second meteorite from the orbit of the Přibram chondrite," *Nature*, vol. 423, pp. 151–153, 2003.

[5] P. Jenniskens, M. H. Shaddad, and D. Numan, "The impact and recovery of asteroid 2008 TC3," *Nature*, vol. 458, pp. 485–488, 2009.

[6] J. Borovička, P. Spurny, D. Šegon et al., "The instrumentally recorded fall of the Križevci meteorite, Croatia, February 4, 2011," *Meteoritics & Planetary Sciences*, vol. 50, pp. 1244–1259, 2015.

[7] J. Borovička, P. Spurný, P. Brown et al., "The trajectory, structure and origin of the Chelyabinsk asteroidal impactor," *Nature*, vol. 503, pp. 235–237, 2013.

[8] J. Borovička, J. Tóth, A. Igaz et al., "The Košice meteorite fall: atmospheric, trajectory, fragmentation, and orbit," *Meteoritics & Planetary Sciences*, vol. 48, pp. 1757–1779, 2013.

[9] J. Tóth, J. Svoreň, and J. Borovička, "The Košice meteorite fall: recovery and stream field," *Meteoritics & Planetary Sciences*, vol. 48, pp. 853–863, 2015.

[10] T. Kohout, K. Havrila, and J. Tóth, "Density, porosity and magnetic susceptibility of the Košice meteorite shower and homogeneity of its parent meteoroid," *Planetary and Space Science*, vol. 93-94, pp. 96–100, 2014.

[11] J. Sitek, J. Dekan, and K. Sedlacková, "Analysis of Košice meteorite by mössbauer spectroscopy," *Journal of Electrical Engineering*, vol. 67, pp. 307–310, 2016.

[12] M. Gritsevich, V. Vinnikov, T. Kohout et al., "A comprehensive study of distribution laws for the fragments of Košice meteorite," *Meteoritics & Planetary Sciences*, vol. 49, pp. 328–345, 2014.

[13] A. S. Betzler and E. P. Borges, "Mass distribution of meteorites," *Monthly Notice of the Royal Astronomical society*, vol. 493, pp. 4058–4064, 2020.

[14] P. Hrábek, "Dynamika preletu meteoroidu atmosférou," Diploma thesis, p. 70, Comenius University in Bratislava, Bratislava, Slovakia, 2016.

[15] K. Havrila, "Modelovanie interakcie mikrometeoritov a meteoritov V planetárnych atmosférach," Diploma thesis, p. 97, Comenius University in Bratislava, Bratislava, Slovakia, 2018.

[16] I. Newton, "Philosophiae naturalis principia Mathematica," in *Sir Isaac Newton's Mathematical Principles of Natural Philosophy*p. 634, University of California Press, Berkeley, CA, USA, 1934.

[17] G. G. Stokes, *On the Theories of the Internal Friction of Fluids in Motions, and the Equilibriumand Motion of Elastic Solids*, Transaction of the Cambridge Philosophical Society, vol. 8, , pp. 75–129, 1845.

[18] J. D. Anderson, *Hypersonic and High Temperature Gas Dynamics*, American 398 Institute of Aeronautics and Astronautics Inc., Reston, VA, USA, 2nd edition, 2006.

[19] A. P. French, *Newtonian Mechanics (The M.I.T. Introductory Physics Series)*, Vol. 760, W. W. Norton and Company Inc., New York, NY, USA, 1st edition, 1970.

[20] G. Falkovich, *Fluid Mechanics*p. 206, 2nd edition, Cambridge University Press, Cambridge, UK, 2018.

[21] L. Clancy, *Aerodynamics*, p. 610, John Wiley, Hoboken, NJ, USA, 1975.

[22] H. Schlichting and K. Gersten, *Boundary-Layer Theory*p. 814, 1st edition, McGraw-Hill, New York, NY, USA, 1955.

[23] A. C. Charters and R. N. Thomas, "The aerodynamic performance of small Spheres from subsonic to high supersonic velocities," *Journal of the Aeronautical Sciences*, vol. 12, pp. 467-468, 1945.

[24] A. J. Hodges, "The drag coefficient of very high velocity spheres," *Journal of the Aeronautical Sciences*, vol. 24, pp. 755–758, 1957.

[25] R. T. Carter, P. S. Jandir, and M. E. Kres, "Estimating the drag coefficients of meteorites for all mach number regimes," in *Proceedings of the 40th Lunar and Planetary Science Conference 2009*, The Woodlands, TX, USA, 2009.

[26] F. A. Morrison, Data Correlation for Drag Coefficient for Sphere, 2013, https://pages.mtu.edu/fmorriso/DataCorrelationForSphereDrag2016.pdf.

[27] A. Rohde, MicroCFD, Computational Fluid Dynamics Software and Consulting, 2001, https://www.microcfd.com/index.htm.

[28] A. Rohde, *Eigenvalues and Eigenvectors of the Euler Equations in General Geometries*, pp. 2001–2609, American Institute of Aeronautics and Astronautics, Reston, VA, USA, 2001.

[29] A. Rohde, V. Golubev, and C. Lessiau, *Direct Simulation of Sound Generated By Viscous Flow over a Cylinder Using a TVD Method*, pp. 2003–3239, American Institute of Aeronautics and Astronautics, Reston, VA, USA, 2003.

[30] A. Rohde and Y. Lee, *A Computational Fluid Dynamics Analysis of a High-Pressure Photo-Emission Gas Spectrometer*, pp. 2011–3551, American Institute of Aeronautics and Astronautics, Reston, VA, USA, 2011.

[31] T. Kohout and A. Kallonen, "Density, porosity, mineralogy, and internal structure of cosmic dust and alteration of its properties during high-velocity atmospheric entry," *Meteoritics & Planetary Sciences*, vol. 49, pp. 1157–1170, 2014.

[32] B. W. McCormick, *Aerodynamics, Aeronautics, and Flight Mechanics*, p. 24, John Wiley & Sons, New York, NY, USA, 1979.

[33] A. E. Hedin, "Extension of the MSIS thermosphere model in to the middle and lower atmosphere," *Journal of Geophysical Research*, vol. 96, pp. 1159–1172, 1991.

[34] J. Moilanen, M. Gritsevich, and E. Lyytinen, "Determination of strewn fields for meteorite falls," *Monthly Notices of the Royal Astronomical Society*, vol. 503, pp. 3337–3350, 2021.

[35] M. Rosenblatt, "Remarks on some nonparametric estimates of a density function," *The Annals of Mathematical Statistics*, vol. 27, no. 3, pp. 832–837, 1956.

[36] E. Loth, J. H. Daspit, and M. Jeong, *Supersonic and Hypersonic Drag Coefficients for a Sphere*, American Institute of Aeronautics and Astronautics Journal, vol. 59, pp. 3261–3274, Reston, VA, USA, 2021.

Hindawi
Advances in Astronomy
Volume 2021, Article ID 9914717, 13 pages
https://doi.org/10.1155/2021/9914717

Research Article

On the Mass Distribution of Fragments of an Asteroid Disrupted in the Earth's Atmosphere

Irina G. Brykina and Lidia A. Egorova

Institute of Mechanics, Lomonosov Moscow State University, Moscow 119192, Russia

Correspondence should be addressed to Lidia A. Egorova; egorova@imec.msu.ru

Received 19 March 2021; Revised 19 May 2021; Accepted 12 June 2021; Published 24 June 2021

Academic Editor: Maria Gritsevich

To model the interaction with the atmosphere of fragments of a disrupted asteroid, which move independently of each other, it is necessary to know their mass distribution. In this regard, an analogy is drawn with fragmentation in high-speed impact experiments performed to simulate the disruption of asteroids at their collisions in outer space. Based on the results of impact experiments and assuming a power law for the mass distribution in a differential form, we obtained the cumulative number of fragments as a function of the fragment mass m normalized to the total mass of fragments, the mass fraction of the largest fragment(s), the number of the largest fragments, and the power index. The formula for the cumulative number of fragments of a disrupted body is used to describe the results of impact experiments for different fragmentation types. The proposed fragment mass distribution is also tested by comparison with the mass distributions of recovered meteorites in the cases of Mbale, Bassikounou, Almahata Sitta, Košice, and Chelyabinsk meteorite falls.

1. Introduction

Asteroids entering the Earth's atmosphere are disrupted under the action of aerodynamic forces, which increase as they penetrate into the denser atmosphere. Disruption of cosmic bodies is a complicated process, depending on many factors: the composition, structure, density, size, and velocity of the body and can occur in different ways. When an asteroid breaks up into a large number of fragments, at the first stage, they move with a common shock wave. To simulate meteoroid disruption at this stage, models of a cloud of fragments moving as a single body were developed [1–5] and used [6–8]; the overview of the models is given in [8]. At the second stage, fragments are scattered far enough to have their own shock waves that interact with each other [9–11]. At the third stage, after complete separation, fragments move independently. To simulate the independent motion of fragments of a destructed cosmic body, models of progressive fragmentation, continuous [12, 13] and discrete, and the instantaneous breakup of a meteoroid or its fragments at one or several gross-fragmentation points were proposed and used [14–18]. In recent years, complex hybrid models have been used, combining different types of fragmentation, including breaking up into large independent fragments and clusters of small fragments. Such approaches have been used to model fragmentation and light curves of Lost City, Innisfree [19], Benešov [19–21], TC3 2008 [22], Košice [21, 23], Chelyabinsk [6, 21, 24, 25], Maribo CM2 [26] bolides, and others.

When modeling the independent motion, ablation, and luminosity of fragments of a destructed asteroid, it is necessary to know their mass distribution. In this regard, an analogy can be drawn between the disruption of asteroids (meteoroids) in the Earth's atmosphere and the disruption of asteroids at their collisions in outer space. To study the collisional evolution of asteroids and simulate their destruction, many experiments have been carried out on the destruction of solid bodies during a high-speed impact [27–42], and others; some reviews are given in [27–29, 32, 36, 37]. Experimental studies covering a wide range of target sizes, shapes, and materials (terrestrial: rocks, cement mortar, basalt, gypsum, glass, ice, artificial

conglomerates, etc., and meteorite samples: ordinary and carbonaceous chondrites), impact velocities, and projectile materials investigate the size, shape, rotation, velocity, and mass (size) distribution of the fragments generated by the impact.

The mass distribution of fragments of a destructed body is usually characterized by a function of the cumulative number of fragments N_m (m), which is defined as the number of fragments with masses greater than or equal to m. In many experimental studies, it was noted that the cumulative mass distribution curve for some fragmentation types is well described by a power law [27–42]. This is usually represented in a simple form where the cumulative number of fragments N_m is proportional to the power of m: $N_m = Bm^{-\beta}$, where coefficient B and power index β are treated as constant. This correlation between the function N_m (m) and fragment mass m gives a linear plot in log-log coordinates with a negative power index slope. However, as also noted in many studies [27–31, 33–37, 40–42], the whole mass distribution curve usually cannot be well represented by a single exponent in the power law and is divided into two or three segments with a steeper slope for larger fragments. In addition to the power law, statistical distributions and multimodal models for nonhomogeneous bodies are used to fit experimental data (see, for example, [43]). In this paper, we use the power law for the fragment mass distribution, presented in differential (incremental) form, which is also given in some papers on impact experiments [27–29, 31, 32]. Integrating this equation and using the mass conservation equation, we obtain the expression for the cumulative number of fragments N_m (m), which is not a linear plot in log-log coordinate and enables us to describe the results of impact experiments with a single curve, that is, using a single exponent.

A similar approach with the use of a power law for the fundamental grain mass distribution, but using a discrete form rather than a continuous one, was used to model the light curves of Leonid meteors [44, 45], and it was concluded that most Leonid light curves could be fitted using a power law distribution of grains. Such approach was used in [46] to model deceleration and light curves of Draconid meteors and in other studies of small meteoroids, as well as in a hybrid model of fragmentation of large meteoroids to describe the mass distribution of small particles (dust), for example, in [23]. The power law of size distribution was also derived based on the analysis of observations of fragmentation of the HAYABUSA spacecraft main body upon its reentry into the Earth's atmosphere [47]. It was a unique opportunity to observe the fragmentation of the "artificial meteoroid." The process has been described in detail; the change in the number of fragments and their size distribution has been obtained by analyzing the images and estimating the brightness of fragments.

The power law mass frequency distribution is also used in the problem of determining meteoroid mass distribution indices for sporadic meteors and meteor showers using radar meteor observations [48–51]. It is shown [52] that the initial mass spectra of various astronomical objects (cosmic dust, asteroids, planets, stars, star clusters, galaxies, and galactic clusters) in ensembles formed by fragmentation (a fast process) can be represented in a first approximation in a statistically significant range by a basis distribution function following a power law. A power law is used in investigating the size-frequency distribution of impact craters on terrestrial planets and asteroids and of projectiles that formed those craters [53–55]. Size distributions based on a power law are widely used to describe various phenomena in geoscience [56–58]: earthquakes (sizes in terms of energy or seismic moment), forest fires areas, the energy of tropical cyclones, amount of rainfall, impact fireballs (sizes in terms of total impact energy), and other natural phenomena. An overview of power law distributions in geoscience is given in [58].

When an asteroid is disrupted in the Earth's atmosphere, the mass distribution of its fragments can be inferred to some extent by the mass distribution of meteorites that have fallen to the ground. Therefore, it seems natural to compare the proposed in this study mass distribution of fragments of a destructed body, based on the power law, with the mass distributions of recovered meteorites in cases where a sufficiently large number have been collected. Previously, various approaches were suggested to approximate the mass (size) distribution of recovered meteorites. Size distributions in six meteorite showers (Barwell, Bruderheim, Gibeon, Johnstown, Sikhote-Alin, and Tenham) were considered in [59] using some empirical formulas. Mass distributions of fragments from sixteen meteorite showers were considered in [60] using some functions, in particular a power law with exponential cutoff and scaling parameters adjusted for each shower to better agreement of theoretical distributions with empirical. The same approach, applying the power law distribution with an exponential cutoff, was used in [61–64] to estimate the shape of original object when considering Košice, Bassikounou, Almahata Sitta, and Sutter's Mill meteorite falls. A curve of the cumulative mass distribution of collected fragments from the Mbale meteorite shower was constructed in [65], and it was shown that a simple power law distribution (straight line in log-log coordinates) fitted the part of this curve for large fragments but could not describe the whole curve. For the Chelyabinsk event, it was also shown [66] that power law distribution in the form of the straight line in log-log coordinates fits only the middle part of meteorites mass distribution. A curve of the mass distribution of the Chelyabinsk meteorites was approximated in [67, 68] by a polynomial of the third degree in logarithmic variables. The mass distribution of recovered fragments after Košice meteorite fall was approximated in [69] using various complex statistical models having several adjusted free parameters; the most appropriate of them were bimodal Weibull, bimodal Grady, and bimodal lognormal distributions. The bimodal lognormal distribution and the more generic exponential distribution were used to model the meteoroid fragmentation in Monte Carlo simulations [70] to predict the strewn field of fallen meteorites, in particular for Košice. The exponential, bimodal exponential, q-exponential, and q-stretched exponential distributions were used in [71] to fit the Košice, Sutter's Mill, and Whitecourt meteorite mass distributions.

Here, we test the proposed formula for the cumulative number of fragments depending on the fragment mass m normalized to the total mass of fragments, the mass fraction of the largest fragment (s), the number of the largest fragments, and the power index as applied to the Mbale, Bassikounou, 2008 TC3 (Almahata Sitta), Košice, and Chelyabinsk meteorite falls.

2. Mass Distribution of Fragments

The mass distribution of fragments of a disrupted body is usually described by the function of the cumulative number of fragments $N_m(m)$ with masses greater than or equal to m, where m is the fragment mass. In this study, we use a differential form of the power law mass distribution [27–29, 31, 32] based on the results of impact experiments:

$$-\frac{\mathrm{d}N_m}{\mathrm{d}m} = n_m, \tag{1}$$

$$n_m = Dm^{-\beta-1}. \tag{2}$$

Here, $\mathrm{d}N_m = n_m \cdot \mathrm{d}m$ means the number of fragments in the mass range from m to $m + \mathrm{d}m$, and coefficient D and power index β are considered as constants. The functions $N_m(m)$ and $n_m(m)$ are considered as continuous functions, defined for $m \le m_l$, where m_l is the mass of the largest fragment, or fragments if there are several largest fragments with the same mass.

Coefficient D is found using the fact that the body mass M (mass of the asteroid just before breakup, mass of the target in experiments) is preserved during destruction; i.e., the mass M is equal to the total mass of all fragments. This can be written as the mass conservation equation:

$$M = \int_0^{m_l} n_m(m')m'\mathrm{d}m'. \tag{3}$$

Substituting the function n_m from relation (2) into this equation, we can find the unknown coefficient D as a function of parameters M and m_l, which we consider as fixed and known values, and power index β (here, we assume $0 < \beta < 1$):

$$D = M\frac{1-\beta}{m_l^{1-\beta}}. \tag{4}$$

Then, using Equations (2) and (4), we obtain the formula for the function $n_m(m)$:

$$n_m = M\frac{1-\beta}{m_l^{1-\beta}}m^{-\beta-1} = \frac{1-\beta}{Ml^{1-\beta}}\left(\frac{m}{M}\right)^{-\beta-1}, \tag{5}$$

where $l = m_l/M$ is the dimensionless mass of the largest fragment. The mass fraction of the largest fragment l is an important parameter characterizing the degree of fragmentation.

To find the cumulative number of fragments $N_m(m)$, we integrate Equation (1) from m to m_l:

$$N_m(m) - N_m(m_l) = \int_m^{m_l} n_m(m')\mathrm{d}m', \quad 0 < m \le m_l. \tag{6}$$

Let us denote the number of fragments with the largest mass m_l by n_l. Then, $N_m(m)$ is found from

$$N_m(m) = \int_m^{m_l} n_m(m')\mathrm{d}m' + n_l. \tag{7}$$

Taking into account equation (5), we obtain the following formula for the cumulative number of fragments N_m:

$$N_m = \frac{1-\beta}{\beta l^{1-\beta}}\left(\left(\frac{m}{M}\right)^{-\beta} - l^{-\beta}\right) + n_l. \tag{8}$$

Assuming that there is only one largest fragment, which is consistent with the results of most experiments, we get

$$N_m = \frac{1-\beta}{\beta l^{1-\beta}}\left(\left(\frac{m}{M}\right)^{-\beta} - l^{-\beta}\right) + 1. \tag{9}$$

Thus, we have obtained the cumulative number of fragments N_m as a function of the dimensionless fragment mass m/M, the mass fraction of the largest fragment (s) l, the number of the largest fragments n_l, and the power index β.

The power index β depends to some extent on the material of the disrupted body and on the degree of its fragmentation. In [31], the β values determined by many researchers in impact experiments were summarized; most of the values are in the range of about 0.5–1. Relatively low β values, typically 0.5–0.7 for rocks subjected to a single impact, were noted in [28]. Upon extensive grinding, fragment size becomes smaller and more uniform, and β value increases.

The function n_m (formula (5)) can be used to model the independent motion and ablation of fragments of the disrupted meteoroid. Independent motion of fragments can be considered when meteoroid breaks up into a cloud of fragments, moving first as a single body; then, at a height h_0, fragments disperse to a sufficient distance to move independently with their own shock waves. Sudden destruction (instantaneous divergence of fragments) at a height h_0 can also be considered. Then, at a height h_0, we have a swarm of independently moving fragments with the number of fragments in the mass range from M_0 to $M_0 + \mathrm{d}M_0$ equal to $n_{m0} \cdot \mathrm{d}M_0$, where

$$n_{m0} = \frac{1-\beta}{M_e l^{1-\beta}}m_0^{-\beta-1}, \qquad m_0 = \frac{M_0}{M_e}. \tag{10}$$

Here, M_0 is the fragment mass at h_0, $m_0 = M_0/M_e$ is the normalized fragment mass at h_0, M_e is the total mass of fragments at h_0, and l is the dimensionless mass of the largest fragment at h_0.

To find the total mass M_Σ, energy deposition per unit height $\mathrm{d}E/\mathrm{d}h_\Sigma$, and luminosity I_Σ of a fragmented meteoroid, we need to integrate over all fragment initial masses:

$$M_\Sigma = \frac{1-\beta}{l^{1-\beta}} \int_0^l m_0^{-\beta-1} M \mathrm{d}m_0,$$

$$I_\Sigma = \frac{1-\beta}{l^{1-\beta}} \int_0^l m_0^{-\beta-1} \left(-\tau \frac{\mathrm{d}}{\mathrm{d}t} \frac{MV^2}{2}\right) \mathrm{d}m_0, \tag{11}$$

$$\left(\frac{\mathrm{d}E}{\mathrm{d}h}\right)_\Sigma = \frac{1-\beta}{l^{1-\beta}} \int_0^l m_0^{-\beta-1} \left(-\frac{1}{V \sin\theta} \frac{\mathrm{d}}{\mathrm{d}t} \frac{MV^2}{2}\right) \mathrm{d}m_0.$$

Here, τ is the luminous efficiency [16]. M and V are the mass and velocity of each fragment, which can be found, for example, using the meteor physics equations for a single body [72] as functions of initial parameters: h_0, m_0, M_e, l, and V_e (the meteoroid velocity at h_0), the entry angle, and the meteoroid density.

3. Comparison with Experimental Data

Numerous impact experiments have shown that high-velocity impact phenomena can be conditionally classified into several fragmentation types. In [29, 31, 32], four fragmentation types are described, depending mainly on the specific energy, which is defined as the kinetic energy of the projectile per unit target mass, and also on the target material and shape, impact geometry, etc. At high specific energy, a large number of small particles occur: high degree or catastrophic fragmentation. At a lower specific energy, relatively large and medium-sized fragments are present together with small ones: cone type of fragmentation. The regime was found when there is one main fragment, which is much larger than the others: the core type of fragmentation. Destruction was also observed when only a crater was formed on the target surface and no spallation occurred: cratering type. This classification is also followed in many other experimental works, for example, in [30, 33–35, 39, 40].

A slightly different classification of disruption types depending on the degree of fragmentation of the target is given in [41]. Type I is cratering. Type II is a transition type where parts of the side surfaces are chipped off. Type III is the core type, which is signified by the whole surface of the target being spalled off with only the core in the central part of the target remaining. Type IV is complete destruction, in which the targets are completely destroyed into fine fragments and no core is left. Types III and IV are called in [41] catastrophic disruption (specific energy more than 1.05 kJ/kg), while types I and II are called noncatastrophic disruption.

We compared the proposed fragment mass distribution with the results of high-speed impact experiments on targets of different materials [30, 31, 33–35, 40, 41] for complete and core types of destruction when using the classification [41] and for catastrophic, cone, and some types of core destruction when using the classification [29–32]. The core type of disruption was observed both for targets with homogeneous structure [29, 31, 32, 35, 41] and for inhomogeneous targets [33, 39]. In [39], different types of core destruction were studied, and it was noted that in the case where the largest core fragment is one order of magnitude larger than the second fragment and there are many small fragments, the distribution curve formed by fragments smaller than or equal to the second one looks like a typical curve of catastrophic disruption and obeys power law mass distribution. When calculating the cumulative number of fragments by formula (8) for a cone or core destruction, where the largest fragment(s) is several times larger than the next one, we excluded the largest fragment(s) from the calculation and started from the second (third) one. Some comparisons of the results of impact experiments with theoretical curves are presented in Figures 1–3 .

Figure 1 shows the comparison of the proposed fragment mass distribution with the results of impact experiments on spherical porous gypsum targets [40] for the catastrophic type of destruction (specific energy: 45.9 kJ/kg), which is characterized by a large number of small fragments with a uniform change in size without gaps. The mass fraction of the largest fragment is equal to 0.026; a cylindrical nylon projectile, much smaller than the target, was used in impact. In calculation by formula (9), plotted in Figure 1 by the blue line, the power index β was adjusted to match the experimental data shown by the black dots; the results are presented in logarithmic coordinates. The cumulative mass distribution described by formula (9) is not a linear plot in logarithmic coordinates, and this makes it possible to describe the experimental mass distribution of fragments of a destroyed target by a single curve, using a single value of the power index β (see Figure 1). This curve has an asymptote at small values of masses with a slope of the power index.

The validity of formula (9) is also supported by comparison with the mass distributions of fragments produced in four impact fragmentation experiments [30] for cubic basalt and pyrophyllite targets (see Figure 2). In Figure 2(a), the mass of both aluminum cylindrical projectiles was 10 g, the basalt target mass was 28.73 g, velocity was 303 m/s, and specific impact energy was 16 kJ/kg; the pyrophyllite target mass was 198.11 g, velocity was 620 m/s, and specific energy was 10 kJ/kg. In Figure 2(b), for the basalt target with a mass of 591.4 g, projectile mass was 2.28 g, velocity was 950 m/s, and specific energy was 1.7 kJ/kg; for the pyrophyllite target with a mass of 159.29 g, projectile mass was 10 g, velocity was 289 m/s, and specific energy was 2.6 kJ/kg.

The mass fraction of the largest fragment decreases with increasing specific impact energy, and the value of the power index depends on the degree of fragmentation (see Figure 2), which, in turn, also depends on the specific energy; this was noted in various experimental studies. For both fragmentation regimes presented in Figures 2(a) and 2(b), calculations by formula (9) are in good agreement with the results of the experiments.

An example of testing the formula for the cumulative number of fragments for the core type of fragmentation (type III [41]) is shown in Figure 3. We compared the analytical calculations with the results of various experiments [41] for different sizes and shapes (cube, sphere, parallelepiped) of basalt targets. Some comparison results are presented in Figure 3 for a series of four experiments

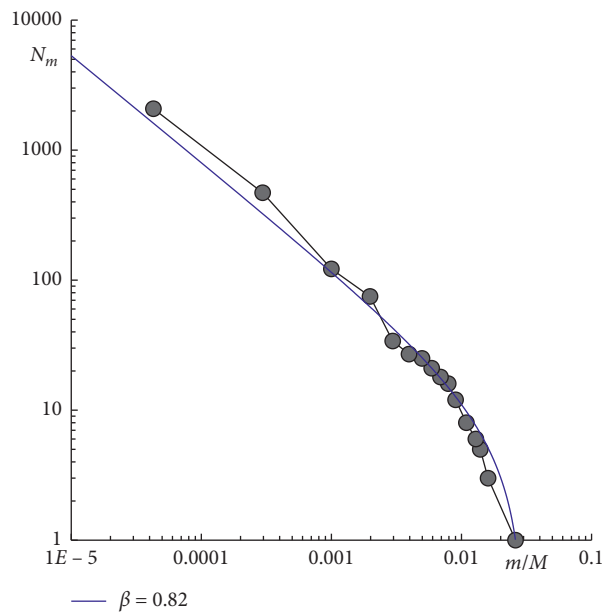

Figure 1: Cumulative number of fragments versus normalized fragment mass. Experimental results [40] at catastrophic destruction (black dots) and calculation by formula (9) at $(l) = 0.026$, $\beta = 0.82$ (blue line).

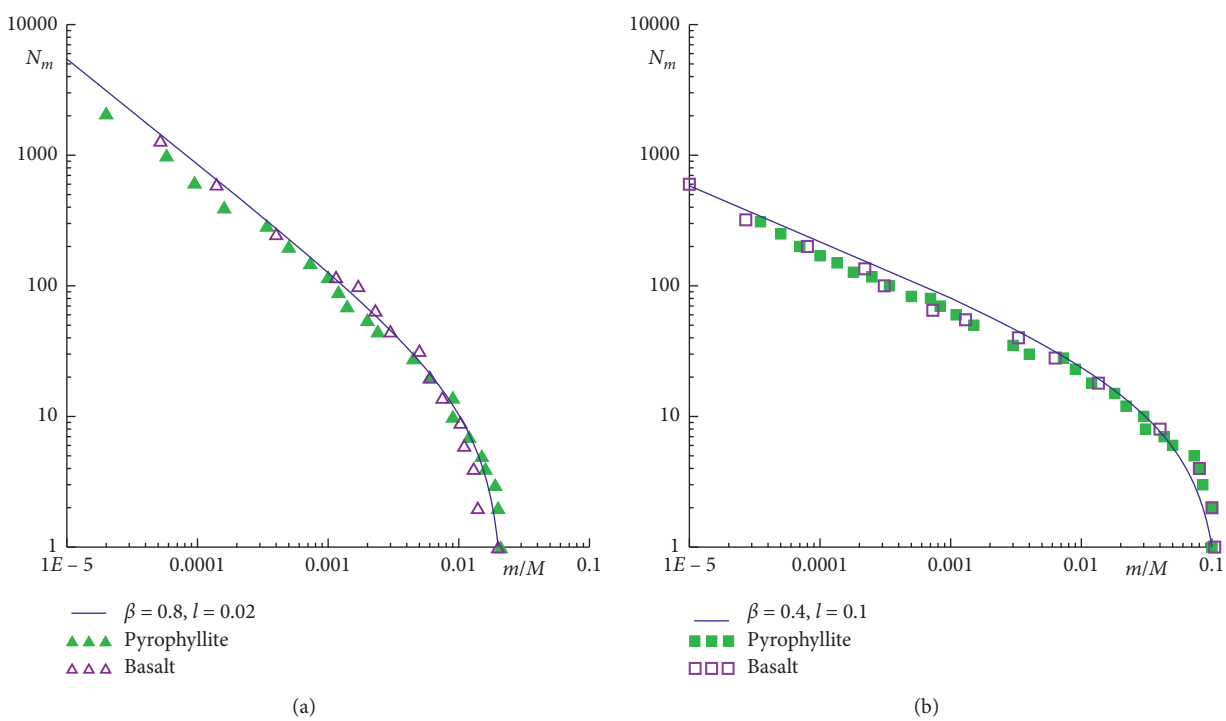

Figure 2: Cumulative number of fragments versus normalized fragment mass. Experimental results [30] are plotted by markers, calculations using formula (9) by the blue line. (a) Specific energy is 16 and 10 kJ/kg for basalt and pyrophyllite targets. (b) Specific energy is 1.7 and 2.6 kJ/kg for basalt and pyrophyllite targets.

carried out under nearly identical conditions to confirm the reproducibility of the experimental results. In these experiments, projectiles were shot at cubic targets with 5 cm side length at impact velocities of 3.7 km/s.

In three impacts, there is one largest fragment, which is much greater than the next, and in one impact, there are two largest fragments. The mass fraction of the largest fragment $l = 0.092$, 0.065, $0.049 + 0.038$, 0.061. We used the formula (9) starting from the second fragment in Figures 3(a), 3(b), and 3(d) and from the third in Figure 3(c). Mass fractions of the following fragments differ less than mass fractions of the largest fragments: $l_2 = 0.027$, 0.025, 0.024, $l_3 = 0.02$. Cumulative mass

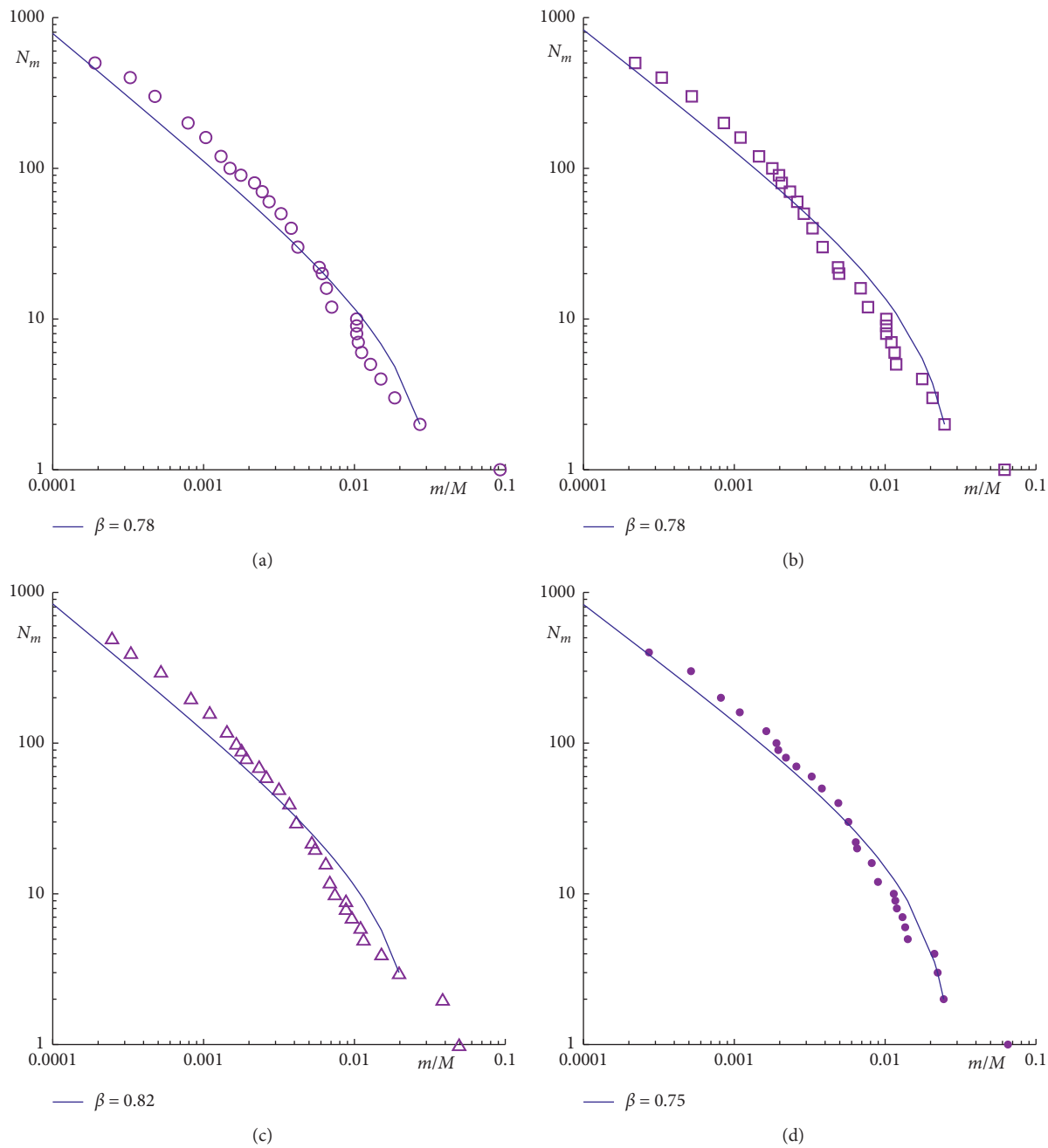

Figure 3: Cumulative number of fragments versus normalized fragment mass. Experimental results [41] at core type of destruction for four impacts under similar conditions (markers) and calculations by formula (9) (blue lines). (a) $(l)_2 = 0.027$, (b) $(l)_2 = 0.025$, (c) $(l)_3 = 0.020$, and (d) $(l)_2 = 0.024$.

distributions for four experiments shown in Figure 3 are very similar when the largest fragments are excluded (the power index changes from 0.75 to 0.82) and are described by the theoretical curves. In an experimental study [38] carried out for the ordinary L6 chondrite, it was also noted that when the largest one or two size fractions for each experiment are ignored, all of the distributions are remarkably similar in shape.

Comparisons with impact experiments showed that formula (8) describes the mass distribution of fragments of a destroyed body in cases of uniform change of fragment masses without gaps. In cases where there are one or two largest fragments, which are several times greater than the next one, formula (8) describes the mass distribution starting from the second (third) fragment. Note that we cannot expect that simple formula (8) with one free parameter, the power index β, can describe all the different types of destruction of bodies into many fragments, which is of a complex nature and depends on various factors. Clarification of the range of applicability of the obtained formula requires further research.

4. Recovered Meteorite Distributions: Results and Discussion

We test the proposed formula for the cumulative number of fragments as a function of the normalized fragment mass by comparing it with the mass distributions of recovered meteorites in cases where a sufficiently large number of them have been collected. Here, we consider five meteorite showers.

4.1. Mbale. The Mbale meteorite fall occurred on August 14, 1992, in and around the city of Mbale in Uganda. The results of an expedition, which was held in the period from August 29 to September 5, 1992, to study the strewn field of the Mbale meteorites, which were classified as ordinary L5/6 chondrites, are presented in paper [65]. During the expedition, eye witness accounts were gathered, 48 meteorite impact positions were located, and masses between 0.1 g and 27.4 kg were recovered, which is considered to be a significant part of the total fallen mass. The certain recovered mass, including 437 fragments (26.18 kg), mostly small, bought from the local people by dealers, is estimated at about 150 kg [65].

To construct the mass distribution of the recovered meteorites, we used the available data from the paper [65] on masses of 53 individual fragments with a total mass $M = 110.6$ kg, a mass of the largest fragment $m_l = 27.4$ kg, and a mass fraction of the largest fragment $l = m_l/M = 0.248$. The cumulative mass distribution of meteorites is shown by violet dots in logarithmic coordinates in Figure 4.

The mass distribution of meteorites is compared with calculation by formula (9) shown by the blue line; the value of the power index β is equal to 0.4. The calculation by the formula for the cumulative number of fragments is consistent with the distribution of Mbale meteorites with the exception of the smallest particles.

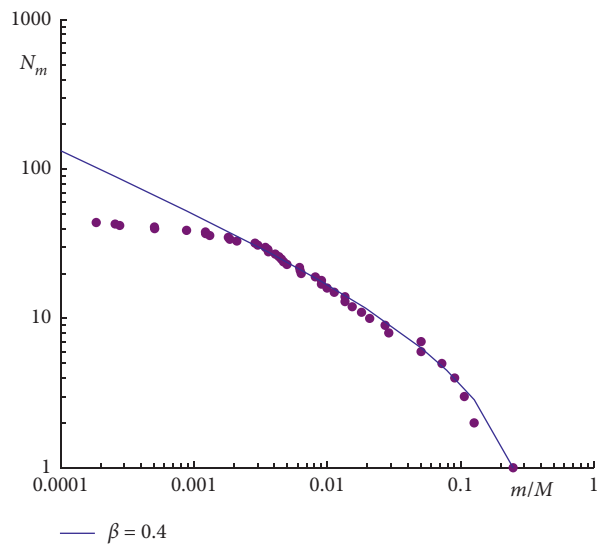

Figure 4: Cumulative number of fragments versus normalized fragment mass for Mbale meteorites. Violet dots: catalogue data [65], blue line: formula (9) at $\beta = 0.4$; 53 fragments, $M(M) = 110.6$ kg, and $m_l = 27.4$ kg.

4.2. Bassikounou. The Bassikounou meteorite fall occurred on October 16, 2006, near the Bassikounou village in southeast Mauritania. Here, we use information about recovered meteorites gathered by Buhl and Baermann [73] from local Mauritanian citizens, mineral dealers, curators, and collectors. The descriptive catalog [73] describes in numbers and in images 108 single masses of a combined weight of 62.38 kg individually and another 382 single masses of a combined weight of 31.66 kg in 8 lots.

When constructing the mass distribution of the recovered meteorites, we used 108 individual masses from the catalog [73] with the total mass $M = 62.38$ kg, the mass of the largest fragment $m_l = 6.1$ kg, and the mass fraction of the largest fragment $l = m_l/M = 0.098$. This distribution is shown by violet dots in logarithmic coordinates in Figure 5.

The mass distribution of meteorites is compared with calculation by formula (9) shown by the blue line; the value of the power index β is equal to 0.4. The proposed formula for cumulative mass distribution describes the distribution of Bassikounou meteorites with masses greater than several tens of grams. If we knew the masses of 382 unaccounted fragments, 365 of which are small (average weight 47.5 g), from the dealer lots and added them, then the left part of the violet dot plot would rise and agreement would be better. The same applies to the distribution of Mbale meteorites.

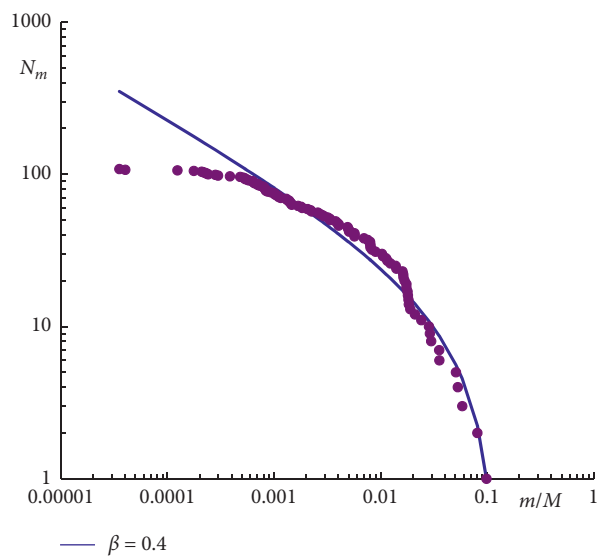

Figure 5: Cumulative number of fragments versus normalized fragment mass for Bassikounou meteorites. Violet dots: catalog data [73], blue line: formula (9) at $\beta = 0.4$; 108 fragments, $M = 62.38$ kg, and $m_l = 6.1$ kg.

4.3. 2008 TC_3 (Almahata Sitta). On October 7, 2008, a small asteroid called 2008 TC_3 entered the Earth's atmosphere and fragmented at an altitude of about 37 km above the Nubian Desert in northern Sudan [74]. The authors of paper [75] describe official expeditions to the desert, during which organized searchers and individuals discovered more than

662 mostly small meteorites with a total mass of 10.7 kg, named "Almahata Sitta"; their fresh look and location in the strewn field, which was predicted by calculating the asteroid 2008 TC_3 trajectory and accounting for high-altitude winds, suggested that they were part of this asteroid. The authors note that most of the recovered meteorites are ureilites and some are ordinary, enstatite, and carbonaceous chondrites.

When constructing the mass distribution of the Almahata Sitta meteorites, we used the masses of 662 fragments from the catalog [75] with the total mass $M = 10.55$ kg, the mass of the largest fragment $m_l = 0.379$ kg, and the mass fraction of the largest fragment $l = 0.036$. The meteorites distribution log-log plot is shown by violet dots in Figure 6. Here, calculation by formula (9) at $\beta = 0.67$ is shown by the blue line.

Figure 6 shows that formula (9) gives good accuracy in describing the distribution of Almahata Sitta meteorites with masses of more than ten grams and less accuracy to a mass of about one gram. Obviously, it is problematic to find all particles with smaller masses, so the difference between the analytical prediction and the distribution of found meteorites is natural.

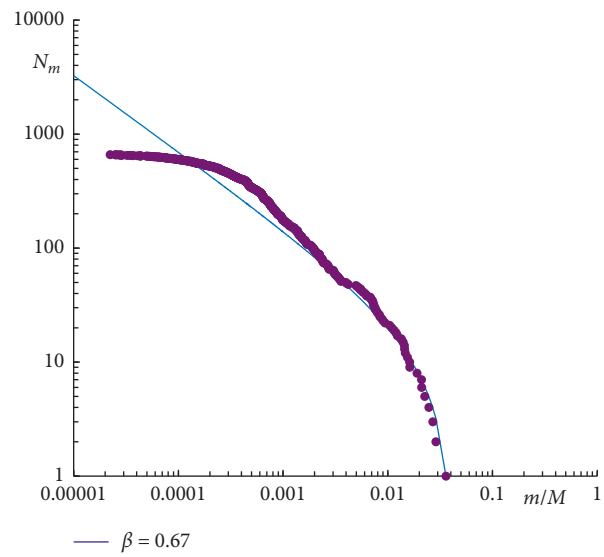

Figure 6: Cumulative number of fragments versus normalized fragment mass for Almahata Sitta meteorites. Violet dots: catalog data [75], blue line: formula (9) at $\beta = 0.67$; 662 fragments, $M = 10.55$ kg, and $m_l = 0.379$ kg.

4.4. Košice. The Košice meteorite fall occurred in eastern Slovakia on February 28, 2010. The meteoroid, with an estimated mass of 3500 kg, entered the atmosphere at a velocity of 15 km/s on a trajectory with a slope of 60° to the horizon; the maximum brightness was reached at an altitude of 36 km [23]. 78 meteorites were recovered in the predicted fall area during several official searches, and 140 meteorites, regarding which information about the masses and coordinates is received, were found by private collectors; a number of fragments were illegally taken out of Slovakia [23, 76]. The meteorites were classified as ordinary H5 chondrites [23, 76].

When constructing the mass distribution of Košice meteorites, we used the masses of 218 fragments presented in catalogs [69, 76]. The total mass of fragments $M = 11.285$ kg, the mass of the largest fragment $m_l = 2.374$ kg, and the mass fraction of largest fragment $l = 0.21$. The mass distribution corresponding to these data is shown by violet dots in Figure 7(a).

In Figure 7(a), one can see a large gap between the masses of the second largest fragment of 2.167 kg and the third one of 0.318 kg. There are two ways to consider this gap. The first one is to assume that there are fragments not found or not officially reported with masses in the range of 2.167–0.318 kg. In [69], it was shown that various statistical models give a high probability of the existence of five or slightly less number of fragments, with masses within this gap. So, when assuming the existence of missing fragments, we add 5 fragments with a total mass of 2–2.5 kg to the gap, in this connection, $M = 13.3$–13.8 kg, and $l = 0.170$–0.178 (in this interval, the mass distribution plot almost is not changed). The mass distribution of meteorites with 5 added fragments is shown in Figure 7(b). We do not plot by violet dots the added fragments in Figure 7(b), because we do not specifically define their masses. The red line corresponds to the calculation by formula (8) at $\beta = 0.7$ and $n_l = 1$.

The fall of the second fragment outside in Figure 7(b) can be explained by the existence of other missing fragments or it can be of random nature. However, the masses of the two largest fragments, 2.374 kg and 2.167 kg, are close, and we can improve agreement assuming that there are two fragments with the largest mass (equal to the mean value) and applying the formula (8) at $n_l = 2$. The mass distribution of Košice meteorites, assuming that there are two fragments with the largest mass of 2.271 kg, is shown in Figure 7(c) (all other fragments are the same as in Figure 7(b)). Theoretical distribution is shown by the red line ($\beta = 0.7$).

Another way is to assume that there are no missing fragments and that the gap between the two largest fragments and the third one is due to the cone (or core, see section 3) type of destruction of the Košice meteoroid. The two largest fragments, which are several times larger than the next one, are characteristic of this type of destruction, often realized in experiments. Comparisons with experimental data [30, 33–35, 41] showed that in cases where there are one or two largest fragments, which are several times greater than the next one, formula (8) describes the mass distribution starting from the second (third) fragment. Figure 7(d) shows the mass distribution of Košice meteorites starting from the third fragment, which is constructed according to the catalog data [69, 76], excluding the two largest fragments (in this case, $M = 6.744$ kg, $m_l = 0.318$ kg, and $l = 0.047$). This distribution is described by the formula for N_m (blue line) down to a mass of fragments of a few grams.

4.5. Chelyabinsk. The passage of the Chelyabinsk meteoroid through the Earth's atmosphere on February 15,

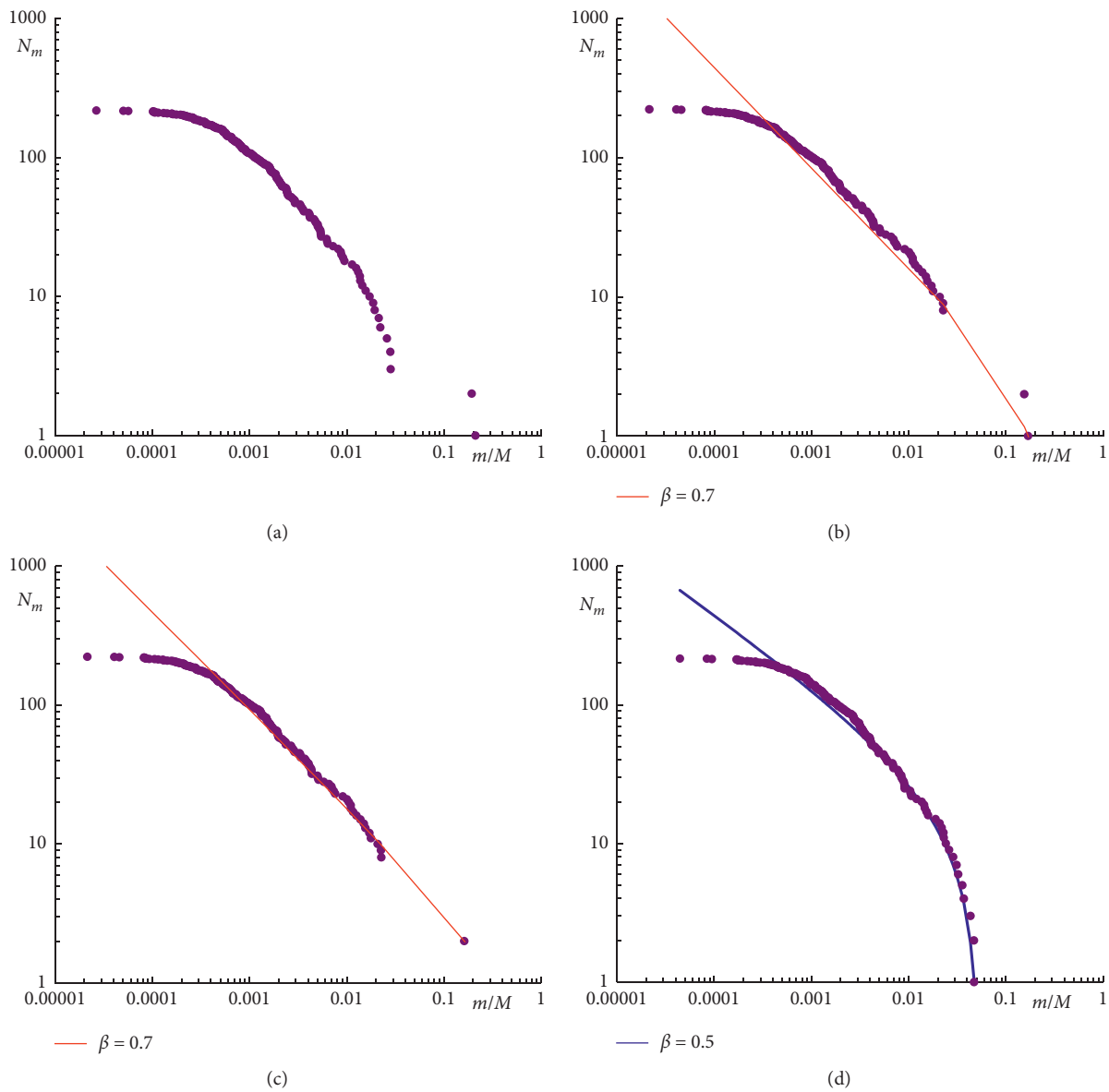

Figure 7: Cumulative number of fragments versus normalized fragment mass for Košice meteorites. Violet dots: catalogue data [69, 76], red and blue lines: formula (8) at $\beta = 0.7$ and 0.5; $m_l = 2.374$ kg; (a) 218 fragments, $M = 11.285$ kg; (b) 223 fragments (5 invisible), $M = 13.3$–13.8 kg; (c) 223 fragments (5 invisible), two largest fragments with mass 2.271 kg, $M = 13.8$ kg, $n_l = 2$; (d) 216 fragments, $M = 6.744$ kg; $m_l = 0.318$ kg.

2013, was recorded starting from an altitude of 97 km by ground-based and satellite observation systems and on numerous video recordings in various localities. Based on the analysis and processing of observational data, the meteoroid trajectory, entry velocity of 19 km/s, entry angle of 18°, density of 3.3 g/cm^3, and the most probable entry mass of 1.2–1.3 × 10^{10} g were determined, and meteorites were classified as ordinary LL5 chondrites [24, 25]. Thousands of small meteorites have been recovered during many official searches, as well as by private collectors and local people. A lot of meteorites are now stored in various institutes and museums, among them the largest fragment weighing 505 kg from Lake Chebarkul is in the State Museum of the South Ural History.

The first data on the masses of recovered Chelyabinsk meteorites were published in [25]. First, to construct the meteorite mass distribution, we used the masses of 177 fragments presented in the study [25]. This distribution is shown by violet dots in Figure 8(a). The total mass of fragments $M = 55.659$ kg, the mass of the largest fragment $m_l = 3.4$ kg, and the mass fraction of the largest fragment $l = 0.061$. Then, we added the meteorite masses from the database of Chelyabinsk State University (CSU) [77], which contain a lot of small fragments; in this connection, $M = 73.889$ kg, $l = 0.046$, and m_l is the same, 3.4 kg. The distribution corresponding to these data (1706 fragments) is shown by violet dots in Figure 8(b). Red, green, and blue lines in Figure (8) correspond to calculations by formula (9)

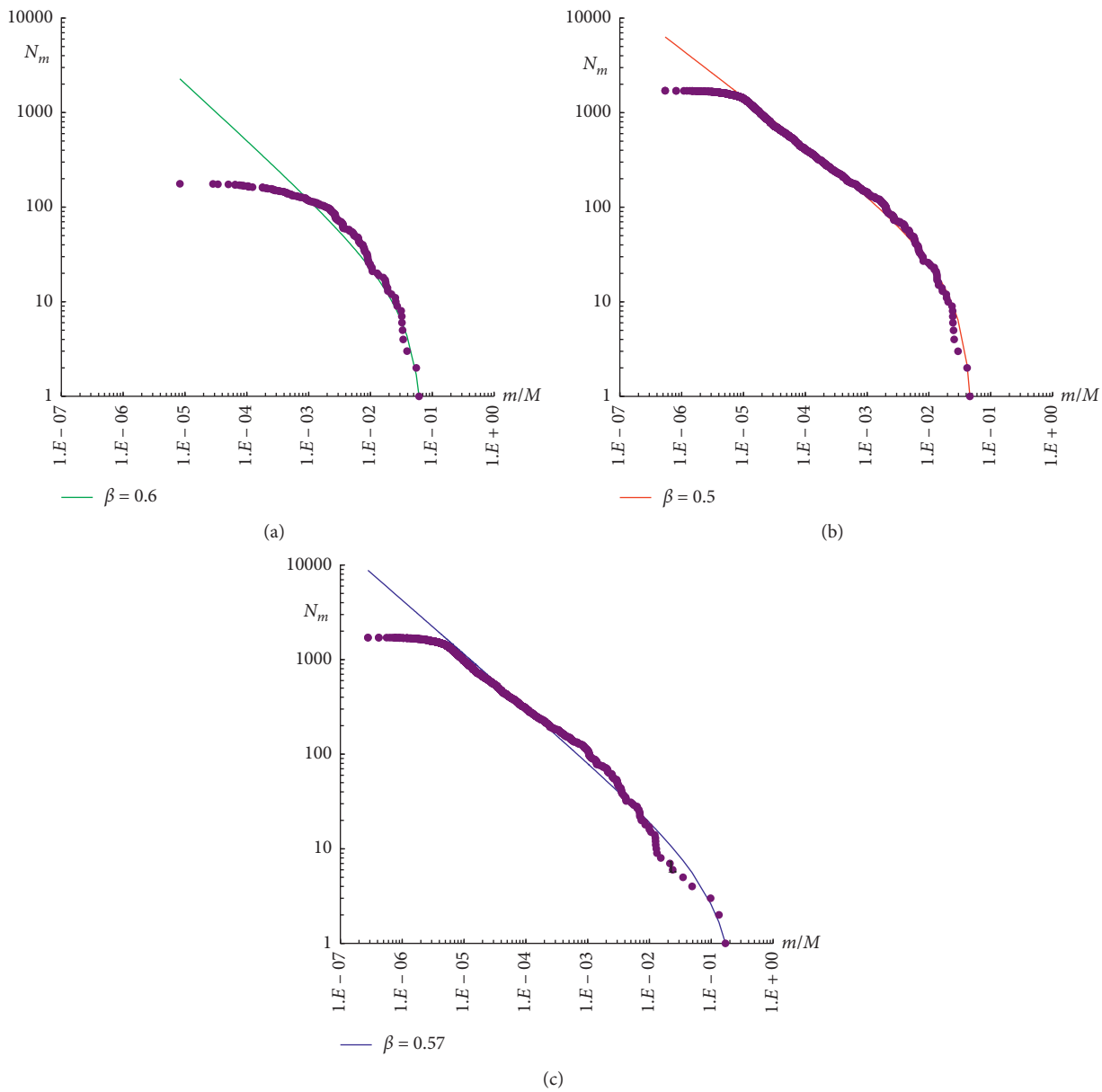

Figure 8: Cumulative number of fragments versus normalized fragment mass for Chelyabinsk meteorites. Red, green, and blue lines: formula (9) at $\beta = 0.5$, 0.6, and 0.57; (a) violet dots: data from [25], 177 fragments, $M = 55.64$ kg, $m_l = 3.4$ kg; (b) violet dots: data from [25] and Database CSU [77], 1706 fragments, $M = 73.89$ kg, $m_l = 3.4$ kg; (c) violet dots: data from [25], Database CSU [77], website [78], and Figure 6 [24], 1711 fragments, $M = 143.19$ kg, $m_l = 24.3$ kg.

at $\beta = 0.5$, 0.6, and 0.57. Figures 8(a) and 8(b) demonstrate that the addition of many small fragments from the Database CSU [77] raises the left side of the violet dots plot, as expected, and significantly improves the agreement of the calculation by formula (9) with the distribution of Chelyabinsk meteorites.

On the news website of the Chelyabinsk region "The first regional", there is information entitled "Local historians have published photos of the second largest fragment of the Chelyabinsk meteorite" that on December 1, 2013, a fragment of the Chelyabinsk meteorite weighing 24.3 kg was found [78], resembling in appearance and features the largest fragment found in lake Chebarkul. Several photos of this fragment are also posted on the site. Suppose that the found stone is really a fragment F2 [24] of the Chelyabinsk meteoroid. Then, it is reasonable to assume that in a large gap between 24.3 kg and 3.4 kg there may be other undiscovered or unregistered fragments, and we add in this gap the hypothetical terminal masses of observed fragments from the Extended Data in Figure 6 of the study [24]. Thus, we add to the fragments shown in Figure 8(b) a fragment weighing 24.3 kg [78] and four fragments between the masses of 3.4 and 24.3 kg from Figure 6 in [24]; in this connection, the total mass $M = 143.188$ kg, and $l = 0.169$. The resulting mass distribution of meteorites is shown by violet dots in Figure 8(c).

Figure 8 shows that the addition of a large fragment with a mass of 24.3 kg to the collection of small fragments (mass fraction of the largest fragment increases by about 7 times) does not fundamentally change the nature of meteorite distribution. Formula (9) is in agreement with the meteorite distribution down to a mass of about a few grams.

Note that we did not include the fragment from Chebarkul Lake in the above consideration. An analogy can be drawn between the destruction of the Chelyabinsk meteoroid and the core type of destruction observed in many impact experiments both for targets with inhomogeneous structure [33, 39] and for homogeneous targets [29, 31, 32, 35, 41]. It was noted [39] that in the case where the largest core fragment is one order of magnitude larger than the second and there are many small fragments, the distribution curve, formed by fragments smaller than or equal to the second one, looks like a typical curve of catastrophic disruption and obeys a power law. Our comparisons with experimental data [30, 33–35, 41] provide support for this. The main Chelyabinsk fragment weighing 505 kg is about 20 times larger than the second-largest fragment weighing 24.3 kg. Thus, we consider the mass distribution of fragments starting from the second one, which is described by formula (9). It should be noted that there are still many small fragments of the Chelyabinsk meteoroid stored in different places, which are also not included in this study.

The main problem in studying the mass distribution of recovered meteorites is that usually only a part of the fallen meteorites is recovered, and only a part of the found meteorites is officially reported. Some meteorites break up when they fall to the ground, and in some cases, it is difficult to distinguish individual meteorites and their fragments. Thus, the distribution of collected meteorites gives only an approximate picture of the real distribution of the fragments of a destructed meteoroid. Nevertheless, the above comparisons for the considered meteorite showers showed that formula (8) is able to describe the distribution of recovered meteorites for fragments with a mass more than several grams (several tens of grams) or for fragments with normalized mass $m/M > 0.001$. In other words, disagreement occurs for fragments with a mass less than 0.1% of the total mass of fragments. The difference between the analytical distribution and the distribution of found meteorites at very low masses is natural because it is impossible to find all small particles. When using formula (8), the values of the adjusted power index β for describing the distributions of meteorites were in the range from 0.4 to 0.7 and for describing the results of experiments in the range of 0.4–0.82. Further research is needed to determine more accurately the most probable value of the parameter β or rather the range of possible values that could be used in the fragment mass distribution when considering the asteroid destruction.

5. Conclusions

The formula for the cumulative number of fragments of a disrupted asteroid is obtained as a function of the fragment mass normalized to the total mass of fragments (the mass of the body before destruction), the mass fraction of the largest fragment(s), the number of the largest fragments, and the free parameter: the power index. The mass distribution of fragments calculated by the proposed formula (8) is consistent with the results of high-velocity impact experiments in cases of uniform change of fragment masses without gaps. In cases where there are one or two largest fragments, which are several times greater than the next one, formula (8) describes the mass distribution starting from the second (third) fragment. The formula for the cumulative number of fragments depending on the normalized fragment mass describes the distributions of recovered meteorites constructed for Mbale, Bassikounou, 2008 TC_3 (Almahata Sitta), Košice, and Chelyabinsk meteorite falls with the exception of small fragments with a mass less than 0.1% of the total mass of fragments. A preliminary estimate of the most probable range of the power index of 0.4–0.7 for meteorite distributions is given. Comparisons with empirical data give grounds to use the proposed fragment mass distribution in modeling the asteroid disruption.

Data Availability

The data used in this article are publicly available, and the article contains references to them.

Conflicts of Interest

The authors declare that they have no conflicts of interest.

Acknowledgments

This study was performed according to the research plan of the Institute of Mechanics of Lomonosov Moscow State University (Project no. AAAA-A16-116021110205-0).

References

[1] S. S. Grigoryan, "Meteorites motion and destruction in planet atmospheres," *Cosmic Research*, vol. 17, pp. 724–740, 1979.

[2] H. J. Melosh, "Atmospheric breakup of terrestrial impactors," *Proceedings of the Seventeenth Lunar and Planetary Science*, vol. 12A, pp. 29–35, 1981.

[3] C. F. Chyba, P. J. Thomas, and K. J. Zahnle, "The 1908 Tunguska explosion: atmospheric disruption of a stony asteroid," *Nature*, vol. 361, no. 6407, pp. 40–44, 1993.

[4] J. G. Hills and M. P. Goda, "The fragmentation of small asteroids in the atmosphere," *The Astronomical Journal*, vol. 105, no. 3, pp. 1114–1144, 1993.

[5] I. G. Brykina, "Large meteoroid fragmentation: modeling the interaction of the Chelyabinsk meteoroid with the atmosphere," *Solar System Research*, vol. 52, no. 5, pp. 426–434, 2018.

[6] P. J. Register, D. L. Mathias, and L. F. Wheeler, "Asteroid fragmentation approaches for modeling atmospheric energy deposition," *Icarus*, vol. 284, pp. 157–166, 2017.

[7] S. McMullan and G. S. Collins, "Uncertainty quantification in continuous fragmentation airburst models," *Icarus*, vol. 327, pp. 19–35, 2019.

[8] I. G. Brykina and M. .D. Bragin, "On models of meteoroid disruption into the cloud of fragments," *Planetary & Space Sci.*vol. 187, Article ID 104942, 2020.

[9] N. A. Artemieva and V. V. Shuvalov, "Motion of a fragmented meteoroid through the planetary atmosphere," *Journal of Geophysical Research: Planets*, vol. 106, no. E2, pp. 3297–3309, 2001.

[10] N. G. Barri, "Dynamics of two spherical objects in supersonic flow," *Doklady Physics*, vol. 55, no. 10, pp. 516–518, 2010.

[11] V. T. Lukashenko and F. A. Maksimov, "Numerical study on the rotation of meteoroid fragments during their separation in the atmosphere," *AIP Conference Proceedings*, vol. 2181, Article ID 020007, 2019.

[12] B. Baldwin and Y. Sheaffer, "Ablation and breakup of large meteoroids during atmospheric entry," *Journal of Geophysical Research*, vol. 76, no. 19, pp. 4653–4668, 1971.

[13] M. I. Avramenko, I. V. Glazyrin, G. V. Ionov, and A. V. Karpeev, "Simulation of the airwave caused by the Chelyabinsk superbolide," *Journal of Geophysical Research: Atmospheres*, vol. 119, no. 12, pp. 7035–7050, 2014.

[14] Z. Ceplecha, P. Spurný, J. Borovička, and J. Keclikova, "Atmospheric fragmentation of meteoroids," *Astronomy & Astrophysics*, vol. 279, pp. 615–626, 1993.

[15] I. V. Nemchinov and O. P. Popova, "An analysis of the 1947 Sikhote-Alin event and a comparison with the phenomenon of February 1, 1994," *Solar System Research*, vol. 31, pp. 408–420, 1997.

[16] Z. Ceplecha, J. Borovička, W. G. Elford et al., "Meteor phenomena and bodies," *Space Science Reviews*, vol. 84, no. 3/4, pp. 327–471, 1998.

[17] D. O. ReVelle, "Recent advances in bolide entry modeling: a bolide potpourri," *Earth, Moon, Planets*, vol. 95, pp. 441–476, 2004.

[18] D. O. ReVelle, "NEO fireball diversity: energetics-based entry modeling and analysis techniques," *Proceedings of the International Astronomical Union Symposium*, vol. 236, pp. 95–106, 2007.

[19] D. O. ReVelle and Z. Ceplecha, "Fragmentation model of meteoroid motion, mass loss, and radiation in the atmosphere," *Meteoritics & Planetary Science*, vol. 40, pp. 35–54, 2005.

[20] J. Borovička, O. P. Popova, I. V. Nemtchinov, P. Spurný, and Z. Ceplecha, "Bolides produced by impacts of large meteoroids into the Earth's atmosphere: comparison of theory with observations. I. Benešov bolide dynamics and fragmentation," *Astronomy & Astrophysics*, vol. 334, pp. 713–728, 1998.

[21] L. F. Wheeler, D. L. Mathias, E. Stokan, and P. G. Brown, "Atmospheric energy deposition modeling and inference for varied meteoroid structures," *Icarus*, vol. 315, pp. 79–91, 2018.

[22] O. Popova, "Passage of bolides through the atmosphere meteoroids: the smallest solar system bodies," in *Proceedings of the Meteoroids 2010 Conference*, pp. 232–242, Breckenridge, Colorado, USA, May 2011.

[23] J. Borovička, J. Toth, A. Igaz et al., "The Košice meteorite fall: atmospheric trajectory, fragmentation, and orbit," *Meteoritics & Planetary Science*, vol. 48, pp. 1757–1779, 2013.

[24] J. Borovička, P. Spurný, P. Brown et al., "The trajectory, structure and origin of the Chelyabinsk asteroidal impactor," *Nature*, vol. 503, no. 7475, pp. 235–237, 2013.

[25] O. P. Popova, P. Jenniskens, V. Kartashova et al., "Chelyabinsk airburst, damage assessment, meteorite recovery, and characterization," *Science*, vol. 342, no. 6162, pp. 1069–1073, 2013.

[26] J. Borovička, O. Popova, and P. Spurný, "The Maribo CM2 meteorite fall—survival of weak material at high entry speed," *Meteoritics & Planetary Science*, vol. 54, pp. 1024–1041, 2019.

[27] W. K. Hartmann and A. C. Hartmann, "Asteroid collisions and evolution of asteroidal mass distribution and meteoritic flux," *Icarus*, vol. 8, no. 1-3, pp. 361–381, 1968.

[28] W. K. Hartmann, "Terrestrial, lunar, and interplanetary rock fragmentation," *Icarus*, vol. 10, no. 2, pp. 201–213, 1969.

[29] A. Fujiwara, G. Kamimoto, and A. Tsukamoto, "Destruction of basaltic bodies by high-velocity impact," *Icarus*, vol. 31, no. 2, pp. 277–288, 1977.

[30] Y. Takagi, H. Mizutani, and S.-I. Kawakami, "Impact fragmentation experiments of basalts and pyrophyllites," *Icarus*, vol. 59, no. 3, pp. 462–477, 1984.

[31] A. Fujiwara, "Results obtained by laboratory simulations of catastrophic impact," *Memorie Della Societa Astronomica Italiana*, vol. 57, pp. 47–64, 1986.

[32] A. Fujiwara, P. Cerroni, D. R. Davis et al., "Experiments and scaling laws for catastrophic collisions," in *Asteroids II*, pp. 240–265, University of Arizona Press, Tucson, AZ, USA, 1989.

[33] D. R. Davis and E. V. Ryan, "On collisional disruption: experimental results and scaling laws," *Icarus*, vol. 83, no. 1, pp. 156–182, 1990.

[34] E. V. Ryan, W. K. Hartmann, and D. R. Davis, "Impact experiments 3: catastrophic fragmentation of aggregate targets and relation to asteroids," *Icarus*, vol. 94, no. 2, pp. 283–298, 1991.

[35] A. Nakamura and A. Fujiwara, "Velocity distribution of fragments formed in a simulated collisional disruption," *Icarus*, vol. 92, no. 1, pp. 132–146, 1991.

[36] G. Martelli, E. V. Ryan, A. M. Nakamura, and I. Giblin, "Catastrophic disruption experiments: recent results," *Planetary and Space Science*, vol. 42, no. 12, pp. 1013–1026, 1994.

[37] K. Holsapple, I. Giblin, K. Housen, A. Nakamura, and E. Ryan, "Asteroid impacts: Laboratory experiments and scaling laws," in *Asteroids III*, pp. 443–462, University of Arizona Press, Tucson, AZ, USA, 2002.

[38] M. J. Cintala and F. Hörz, "Experimental impacts into chondritic targets, part I: disruption of an L6 chondrite by multiple impacts," *Meteoritics & Planetary Science*, vol. 43, no. 4, pp. 771–803, 2008.

[39] C. Okamoto and M. Arakawa, "Experimental study on the impact fragmentation of core-mantle bodies: implications for collisional disruption of rocky planetesimals with sintered core covered with porous mantle," *Icarus*, vol. 197, no. 2, pp. 627–637, 2008.

[40] C. Okamoto and M. Arakawa, "Experimental study on the collisional disruption of porous gypsum spheres," *Meteoritics & Planetary Science*, vol. 44, no. 12, pp. 1947–1954, 2009.

[41] T. Michikami, A. Hagermann, T. Kadokawa et al., "Fragment shapes in impact experiments ranging from cratering to catastrophic disruption," *Icarus*, vol. 264, pp. 316–330, 2016.

[42] G. J. Flynn, D. D. Durda, E. B. Patmore et al., "Hypervelocity cratering and disruption of the Northwest Africa 869 ordinary chondrite meteorite: implications for crater production, catastrophic disruption, momentum transfer and dust production on asteroids," *Planetary and Space Science*, vol. 164, pp. 91–105, 2018.

[43] V. V. Silvestrov, "Application of the Gilvarry distribution to the statistical description of fragmentation of solids under dynamic loading," *Combustion, Explosion & Shock Waves*, vol. 40, pp. 225–237, 2004.

[44] M. Beech and I. S. Murray, "Leonid meteor light-curve synthesis," *Monthly Notices of the Royal Astronomical Society*, vol. 345, no. 2, pp. 696–704, 2003.

[45] M. D. Campbell-Brown and D. Koschny, "Model of the ablation of faint meteors," *Astronomy & Astrophysics*, vol. 418, no. 2, pp. 751–758, 2004.

[46] J. Borovička, P. Spurný, and P. Koten, "Atmospheric deceleration and light curves of Draconid meteors and implications for the structure of cometary dust," *Astronomy & Astrophysics*, vol. 473, pp. 661–672, 2007.

[47] J.-i. Watanabe, T. Ohkawa, M. Sato, K. Ohnishi, and Y. Iijima, "Fragmentation of the HAYABUSA spacecraft on re-entry," *Publications of the Astronomical Society of Japan*, vol. 63, no. 5, pp. 955–960, 2011.

[48] R. C. Blaauw, M. D. Campbell-Brown, and R. J. Weryk, "A meteoroid stream survey using the Canadian Meteor Orbit Radar - III. Mass distribution indices of six major meteor showers," *Monthly Notices of the Royal Astronomical Society*, vol. 414, no. 4, pp. 3322–3329, 2011.

[49] P. Pokorný, D. Vokrouhlický, D. Nesvorný, M. D. Campbell-Brown, and P. G. Brown, "Dynamical model for the toroidal sporadic meteors," *The Astrophysical Journal*, vol. 789, 2014.

[50] P. Pokorný and P. G. Brown, "A reproducible method to determine the meteoroid mass index," *Astron. & Astroph.*vol. 592, 2016.

[51] D. Janches, C. Brunini, and J. L. Hormaechea, "A decade of sporadic meteoroid mass distribution indices in the southern hemisphere derived from SAAMER's meteor observations," *The Astrophysical Journal*, vol. 157, 2019.

[52] A. V. Tutukov and B. M. Shustov, "Fundamental reasons for the similarity and differences of the mass spectra of various astronomical objects," *Astrophysics*, vol. 63, no. 4, pp. 552–565, 2020.

[53] B. A. Ivanov, G. Neukum, and R. Wagner, "Size-frequency distributions of planetary impact craters and asteroids," in *Collisional Processes in the Solar System (Astrophysics and Space Science Library)*, vol. 261, pp. 1–34, Springer, Berlin, Germany, 2001.

[54] B. A. Ivanov, G. Neukum, W. F. Bottke, and W. K. Hartmann, "The comparison of size-frequency distributions of impact craters and asteroids and the planetary cratering rate," in *Asteroids III*, pp. 89–101, University of Arizona Press, Tucson, AZ, USA, 2002.

[55] M. Bronikowska, N. A. Artemieva, and K. Wünnemann, "Reconstruction of the Morasko meteoroid impact – Insight from numerical modeling," *Meteoritics & Planetary Science*, vol. 52, pp. 1704–1721, 2013.

[56] S. M. Burroughs and S. F. Tebbens, "Upper-truncated power laws in natural systems," *Pure and Applied Geophysics*, vol. 158, no. 4, pp. 741–757, 2001.

[57] A. Deluca and Á. Corral, "Fitting and goodness-of-fit test of non-truncated and truncated power-law distributions," *Acta Geophysica*, vol. 61, no. 6, pp. 1351–1394, 2013.

[58] Á. Corral and Á. González, "Power law size distributions in geoscience revisited," *Earth and Space Science*, vol. 6, pp. 673–697, 2019.

[59] M. J. Frost, "Size and spacial distribution in meteoritic showers," *Meteoritics*, vol. 4, no. 3, pp. 217–232, 1969.

[60] L. Oddershede, A. Meibom, and J. Bohr, "Scaling analysis of meteorite shower mass distributions," *Europhysics Letters (EPL)*, vol. 43, no. 5, pp. 598–604, 1998.

[61] V. Vinnikov, M. Gritsevich, and L. Turchak, "Shape estimation for Košice, Almahata Sitta and Bassikounou meteoroids," *Proceedings of the International Astronomical Union*, vol. 10, no. 306, pp. 394–396, 2015.

[62] V. V. Vinnikov, M. I. Gritsevich, D. V. Kuznetsova, and L. I. Turchak, "Estimation of the initial shape of meteoroids based on statistical distributions of fragment masses," *Doklady Physics*, vol. 61, no. 6, pp. 305–308, 2016.

[63] L. I. Turchak, M. I. Gritsevich, and V. V. Vinnikov, "Statistical approach to estimate initial meteoroid shape from empirical mass distribution of recovered fragments," *AIP Conference Proceedings*, vol. 1773, Article ID 110014, 2016.

[64] M. Gritsevich, V. Dmitriev, V. Vinnikov et al., "Constraining the pre-atmospheric parameters of large meteoroids: Košice, a case study," *Astrophysics and Space Science Proceedings*, vol. 46, pp. 153–183, 2017.

[65] P. Jenniskens, H. Betlem, J. Betlem et al., "The Mbale meteorite shower," *Meteoritics*, vol. 29, no. 2, pp. 246–254, 1994.

[66] O. P. Popova, P. Jenniskens, and D. O. Glazachev, "Chelyabinsk meteoroid fragmentation," *Dynamical Processes in Geospheres*, vol. 5, pp. 59–78, 2014.

[67] D. D. Badyukov and A. E. Dudorov, "Fragments of the Chelyabinsk meteorite shower: distribution of masses and sizes and constraints on the mass of the largest fragment," *Geochemistry International*, vol. 51, no. 7, pp. 583–586, 2013.

[68] D. D. Badyukov, A. E. Dudorov, and S. A. Khaybrahmanov, "Mass distribution of fragments of the Chelyabinsk meteorite," *Chelyabinsk Physical and Mathematical Journal*, vol. 1, no. 330, pp. 40–46, 2014.

[69] M. Gritsevich, V. Vinnikov, T. Kohout et al., "A comprehensive study of distribution laws for the fragments of Košice meteorite," *Meteoritics & Planetary Science*, vol. 49, no. 3, pp. 328–345, 2014.

[70] J. Moilanen, M. Gritsevich, and E. Lyytinen, "Determination of strewn fields for meteorite falls," *Monthly Notices of the Royal Astronomical Society*, vol. 503, no. 3, pp. 3337–3350, 2021.

[71] A. S. Betzler and E. P. Borges, "Mass distributions of meteorites," *Monthly Notices of the Royal Astronomical Society*, vol. 493, no. 3, pp. 4058–4064, 2020.

[72] V. A. Bronshten, *Physics of Meteoric Phenomena*, Springer, Dordrecht, Netherlands, 1983.

[73] S. Buhl and M. Baermann, The Bassikounou Meteorite Fall – Descriptive Catalog of the Recovered Masses https://www.meteorite-recon.com/wp-content/uploads/pdf/Buhl_Baermann_Catalog, 2007.

[74] P. Jenniskens, M. H. Shaddad, D. Numan et al., "The impact and recovery of asteroid 2008 TC3," *Nature*, vol. 458, no. 7237, pp. 485–488, 2009.

[75] M. H. Shaddad, P. Jenniskens, D. Numan et al., "The recovery of asteroid 2008 TC3," *Meteoritics & Planetary Science*, vol. 45, no. 10-11, pp. 1557–1589, 2010.

[76] J. Tóth, J. Svoreň, J. Borovička et al., "The Košice meteorite fall: recovery and strewn field," *Meteoritics & Planetary Science*, vol. 50, no. 5, pp. 853–863, 2015.

[77] 2013 Database of the Chelyabinsk Meteorite Fragments of Chelyabinsk State University https://www.csu.ru/science/chelyabinsk-meteor-study-center/database.aspx.

[78] The first regional https://www.1obl.ru/news/o-lyudyakh/foto-vtorogzmeru-oskolka-meteorita-chelyabinsk/.

Hindawi
Advances in Astronomy
Volume 2021, Article ID 8852772, 13 pages
https://doi.org/10.1155/2021/8852772

Research Article

A Numerical Approach to Study Ablation of Large Bolides: Application to Chelyabinsk

Josep M. Trigo-Rodríguez,[1,2] Joan Dergham,[1,2] Maria Gritsevich,[3,4,5,6] Esko Lyytinen,[5†] Elizabeth A. Silber[7,8] and Iwan P. Williams[9]

[1]*Institut de Ciències de l'Espai–CSIC, Campus UAB, Facultat de Ciències, Torre C5-parell-2a, 08193 Bellaterra, Barcelona, Catalonia, Spain*
[2]*Institut d'Estudis Espacials de Catalunya (IEEC), Edif. Nexus, c/Gran Capità, 2-4, 08034 Barcelona, Catalonia, Spain*
[3]*Finnish Geospatial Research Institute (FGI), Geodeetinrinne 2, FI-02430 Masala, Finland*
[4]*Department of Physics, University of Helsinki, Gustaf Hällströmin katu 2a, P.O. Box 64, FI-00014 Helsinki, Finland*
[5]*Finnish Fireball Network, Helsinki, Finland*
[6]*Institute of Physics and Technology, Ural Federal University, Mira str. 19., 620002 Ekaterinburg, Russia*
[7]*Department of Earth Sciences, Western University, London, ON N6A 5B7, Canada*
[8]*The Institute for Earth and Space Exploration, Western University, London, ON N6A 3K7, Canada*
[9]*Astronomy Unit, Queen Mary, University of London, Mile End Rd., London E1 4NS, UK*
[†]*Deceased*

Correspondence should be addressed to Josep M. Trigo-Rodríguez; trigo@ice.csic.es

Received 31 August 2020; Revised 13 January 2021; Accepted 2 March 2021; Published 27 March 2021

Academic Editor: Kovacs Tamas

In this study, we investigate the ablation properties of bolides capable of producing meteorites. The casual dashcam recordings from many locations of the Chelyabinsk superbolide associated with the atmospheric entry of an 18 m in diameter near-Earth object (NEO) have provided an excellent opportunity to reconstruct its atmospheric trajectory, deceleration, and heliocentric orbit. In this study, we focus on the study of the ablation properties of the Chelyabinsk bolide on the basis of its deceleration and fragmentation. We explore whether meteoroids exhibiting abrupt fragmentation can be studied by analyzing segments of the trajectory that do not include a disruption episode. We apply that approach to the lower part of the trajectory of the Chelyabinsk bolide to demonstrate that the obtained parameters are consistent. To do that, we implemented a numerical (Runge–Kutta) method appropriate for deriving the ablation properties of bolides based on observations. The method was successfully tested with the cases previously published in the literature. Our model yields fits that agree with observations reasonably well. It also produces a good fit to the main observed characteristics of Chelyabinsk superbolide and provides its averaged ablation coefficient $\sigma = 0.034\,\mathrm{s}^2\,\mathrm{km}^{-2}$. Our study also explores the main implications for impact hazard, concluding that tens of meters in diameter NEOs encountering the Earth in grazing trajectories and exhibiting low geocentric velocities are penetrating deeper into the atmosphere than previously thought and, as such, are capable of producing meteorites and even damage on the ground.

1. Introduction

On February 15, 2013, our view about impact hazard was seriously challenged. While there was a sense of accomplishment for being able to forecast the close approach of 2012 DA near-Earth asteroid (NEA) within a distance of 27700 km, eventhough this NEO was discovered only one year prior, an unexpected impact with an Apollo asteroid ensued [1]. At 03:20 UTC, a superbolide, also known as the Chelyabinsk superbolide, flew over the Russian territory and Kazakhstan. The possible link between the superbolide and the 2012 DA NEA was discarded by the European Space Agency (ESA) and the Jet Propulsion Laboratory–National Aeronautics and Space Administration (JPL-NASA) from

the reconstruction of the incoming fireball trajectory. The Chelyabinsk superbolide entered the atmosphere at ~19 km/s, and according to the US sensor data (CNEOS fireball list: https://cneos.jpl.nasa.gov/fireballs/), it reached the maximum brightness at an altitude of 23.3 km with a velocity of 18.6 km/s [1, 2], also providing us with valuable samples in the form of meteorites.

The existence of meteoroid streams capable of producing meteorite-dropping bolides is a hot topic in planetary science. Such streams were first proposed by Halliday [3, 4]. Their existence has important implications because they can naturally deliver to the Earth different types of rock-forming materials from potentially hazardous asteroids (PHAs). It is believed that NEOs in the Earth's vicinity are undergoing dynamical and collisional evolution on relatively short timescales. We previously identified several NEO complexes that are producing meteorite-dropping bolides, and we hypothesize that they could have been produced during close approaches to terrestrial planets [5, 6]. Such formation scenario for this kind of asteroidal complexes is now reinforced with the recent discovery of a complex of NEOs likely associated with the NEA progenitor of the Chelyabinsk bolide [7]. The shattered pieces resulting from the disruption of NEOs visiting the inner solar system can spread along the entire parent body orbit on a time-scale of centuries [4, 8, 9]. This scenario is also consistent with the modern view of NEOs being resurfaced as consequence of close approaches [10]. Additionally, the meteorites recovered from the Chelyabinsk have a brecciated nature [11, 12] that is reminiscent of the complex collisional history and a probable rubble pile structure of the asteroid progenitor of the complex [13]. The existence of these asteroidal complexes in the near-Earth region has important implications as they could be the source of low spatial density meteoroid streams populated by large meteoroids. Such complexes could be the source of the poorly known fireball-producing radiants [14, 15]. This could have important implications for the fraction of sporadic meteoroids producing bright fireballs and in the physical mechanisms envisioned in the past [16–18].

The Chelyabinsk event is also of interest because of its magnitude and energy and due to its relevance to be considered as a representative example of the most frequent outcome of the impact hazard associated with small asteroids in human timescales. Chelyabinsk also exemplifies the importance that fragmentation has for small asteroids, which can even excavate a crater on the Earth's surface, although rarely [19–23]. Fragmentation is important as it provides a mechanism in which a significant part of the kinetic energy associated with small asteroids is released. It was certainly a very relevant process for the Tunguska event [24, 25], and in the better-known case of Chelyabinsk, most of the kinetic energy was transferred to the internal energy of the air, which is radiated as light [26].

One way to study meteoroids as they enter the Earth's atmosphere is through video observations of such events. Consequently, we are developing complementary approaches to study the dynamical behavior of video-recorded bolides in much detail. The SPanish Meteor Network (SPMN) pioneered the application of high-sensitivity cameras for detecting fireballs, and it currently maintains an online list of bright events detected over Spain, Portugal, Southern France, and Morocco since 1999 [27, 28]. For example, casual video recordings plus several still photographs of the superbolide in flight allowed us to reconstruct the heliocentric orbit of Villalbeto de la Peña meteorite in the framework of the SPMN [28]. The possibility of studying superbolides such as Chelyabinsk is a very attractive milestone to be considered. The software used in this study was developed as part of a master thesis [29] and subsequently tested and validated using several cases discussed by [29], as well as events from the 25 video and all-sky CCD stations set up over the Iberian Peninsula by the SPMN. In this context, we have been engaged in studying the dynamic behavior of meteoroids decelerating in the Earth's atmosphere [30, 31].

In this study, we study the Chelyabinsk bolide by following a Runge–Kutta method of meteor investigation similar to that developed by Bellot Rubio et al. [32]. We aim to test if that specific method is also valid for another mass range, particularly for small asteroids and large meter-sized meteoroids. We first describe our numerical model and test it against the known meteor events. We compare our code validation results to the results obtained by Bellot Rubio et al. [32] for the same dataset. We then apply our numerical model to the Chelyabinsk superbolide in order to study its dynamical behavior. For the sake of simplicity, our model considers a constant ablation coefficient and the shape factor, even though these parameters could vary in different ablation stages [33–35].

This study is structured as follows: the data reduction and the theoretical approach pertaining to the Chelyabinsk bolide are described in the next section. In Section 3, the main implications of this work in the context of fireballs, meteorites, and NEO research are discussed. We use the model to determine the fireball flight parameters, and by studying the deceleration, we also obtain the ablation coefficient. Finally, the conclusions of this work are presented in Section 4.

2. Data Reduction, Theoretical Approach, and Observations

The Chelyabinsk superbolide was an unexpected daylight superbolide as many other unpredicted meteorite-dropping bolides in history. Fortunately, numerous casual video recordings of the bolide trajectory from the ground were obtained, given the nowadays common dashcams available in private motor vehicles in Russia. According to the video recordings available, it is possible to study the atmospheric trajectory and deceleration carefully, allowing the reconstruction of the heliocentric orbit in record time [2, 26].

2.1. Single Body Theory. There are two main approaches in the study of the dynamic properties of meteors during atmospheric interaction, the quasicontinuous fragmentation (QCF) theory introduced by Novikov et al. [37], which was

later extended by Babadzhanov [38], and the single body theory described by Bronshsten [39]. There have been discrepancies in the applicability conditions of both methods: the single body works with basic differential equations, while the QCF uses semiempirical formulas studying only the luminosity produced by the meteor. The main difference is that the single body theory obtains smaller dynamical masses than the QCF method. Thus far, neither approach is prevalent, and the reason why the theories do not converge could be attributed to the contribution of other key processes such as the fragmentation and deceleration of meteoroids during ablation or to the poorly constrained values of the bulk density and/or the luminous efficiency coefficient [40–42].

We remark that the initial dynamic mass estimate or the preatmospheric size can be derived using the methods described in other works [43–48]; hence, we leave it out of the scope of the present model. We also note that alternative models accounting for ablation have been recently developed; however, further discussion on that topic is beyond the scope of this study, and the reader is referred to the following literature [46, 47, 49–52]. As noted in the introduction, high-strength meteoroids from asteroids or planetary bodies exhibit a very different behavior than fragile dust aggregates originating from comets [53–57].

2.2. The Role of Fragmentation. The fragmentation of meteoroids was studied in detail by various authors [38, 40]. After analyzing different photographic observations, Levin [40] distinguished four possible types of fragmentation: (a) the decay of the meteoroid into large nonfragmenting debris, (b) the progressive disintegration of the original meteoroid into fragments that continue to crumble into smaller fragments, (c) the instantaneous ejection of a large number of small particles, which, when affecting the entire meteoroid, is called a catastrophic disruption, and finally, (d) the quasicontinuous fragmentation which consists of the gradual release of a large number of small particles from the surface and their subsequent evaporation due to high temperatures associated with the shock thermal wave formed around the body.

In practice, a combination of two or more types of fragmentation can be observed in a given meteor event. In fact, it is possible to observe that (a) and (c) fragmentation types described in the preceding paragraph could occur more than once for the same meteor event. The analysis of meteors performed by Jacchia [58] using Super-Schmidt cameras demonstrated that the single body theory does not work for cases which suffer abrupt types of fragmentation along the trajectory. As a direct consequence, meteoroids exhibiting fragmentation of the first (a), second (b), and third (c) kind should not be studied using this simplified single body theory. When a meteoroid suffers an abrupt fragmentation, the main body loses mass instantaneously, and therefore, the single body equations cannot be applied since the condition of continuity of mass is not satisfied. Thus, the cases with possible abrupt fragmentation episode(s) will not be examined in this work.

2.3. The Single Body Theory: The Drag and Mass Loss Equations. The dynamic behavior of a meteoroid as it interacts with the Earth's atmosphere is described using the drag and mass loss equations. These equations, as presented by Bronshten [39], are as follows:

$$\frac{\mathrm{d}v}{\mathrm{d}t} = -K\rho_{\mathrm{air}} m^{-1/3} \cdot v^2, \tag{1}$$

$$\frac{\mathrm{d}m}{\mathrm{d}t} = -\sigma K\rho_{\mathrm{air}} m^{2/3} \cdot v^3. \tag{2}$$

where K is the shape-density coefficient, ρ_{air} is the air density, m is the meteoroid mass, v is the instantaneous velocity, and σ is the ablation coefficient.

By using equations (1) and (2), the parameters to be identified are K and σ. The ablation coefficient defines the loss of mass for the bolide as it penetrates the atmosphere; the larger the value is, the more the mass will be ablated for a given velocity. The value of the ablation coefficient depends on various factors and is expressed as

$$\sigma = \frac{\Lambda}{2\Gamma Q}, \tag{3}$$

where Λ is the heat transfer coefficient, Γ is the drag coefficient, and Q is the heat of ablation.

The shape-density coefficient depends on the shape and density of the meteoroid and is expressed as

$$K = \frac{sA}{\rho^{2/3}}, \tag{4}$$

where A is the shape factor, s is the cross-section area, and ρ is the meteoroid bulk density.

We must point out that the observational data obtained from the reconstruction of the trajectories of meteors using CCD or video cameras is basically the frame to frame speed of the bolide as a function of the height, requiring another equation to link the time with the altitude:

$$\frac{\mathrm{d}h}{\mathrm{d}t} = -v \cdot \cos(z), \tag{5}$$

where z is the zenith angle.

By substituting equation (5) into equations (1) and (2), the following expressions are obtained:

$$\frac{\mathrm{d}v}{\mathrm{d}h} = \frac{K\rho_{\mathrm{air}} m^{-1/3} \cdot v}{\cos(z)}, \tag{6}$$

$$\frac{\mathrm{d}m}{\mathrm{d}h} = \frac{\sigma K\rho_{air} m^{2/3} \cdot v^2}{\cos(z)}. \tag{7}$$

Next, by dividing equation (2) by equation (1), we obtain

$$\frac{\mathrm{d}m}{\mathrm{d}v} = m\sigma v. \tag{8}$$

Solving this differential equation with the boundary condition of $m = m_o$, when $v = v_o$, the following is obtained:

$$m = m_o \cdot e^{-(1/2)\sigma\left(v_o{}^2 - v^2\right)}. \tag{9}$$

Now, we combine equations (9) and (6) to derive

$$\frac{\mathrm{d}v}{\mathrm{d}h} = K\rho_{\mathrm{air}}\left(m_o \cdot \left(e^{-(1/2)\sigma\left(v_o{}^2 - v^2\right)}\right)\right)^{-(1/3)} \cdot v \cdot \frac{1}{\cos z}. \quad (10)$$

In order to obtain the value of K and σ, we use equation (10), as it uses substitution for the dependence on the instantaneous mass, and thus, we deal with one equation instead of two. Furthermore, there is the initial mass, which is an important parameter to be studied. Equation (10) directly links the deceleration of the meteoroid as a function of different parameters, in particular the zenith angle. The last term is of particular interest as it modulates the full equation. For the vertical entry ($z = 0^\circ$), the deceleration is maximized, while for z close to 90°, the deceleration is minimized. For that reason, large meteoroids at grazing angles are able to follow extremely long trajectories or even escape again into space, such as the Grand Tetons superbolide that spent nearly two minutes traveling over several states of the USA and Canada on August 10, 1972 [11, 59].

However, by using the concepts introduced above, it is not possible to obtain the values of initial mass (m_o) and K. The parameters that can be found are only the expressions of $m_o{}^{-1/3} \cdot K$ and σ. Consequently, another equation is required to obtain K and m_o separately. The remaining expression is the photometric equation:

$$I = \frac{\tau}{2}\left(-\frac{\mathrm{d}m}{\mathrm{d}t}\right) \cdot v^2, \quad (11)$$

where τ is the luminous efficiency. This equation is assuming $v =$ constant, and it is often applied to small meteors. The luminous efficiency is obtained empirically; thus, any deviations in that value might produce significant changes in the results. This equation will be referred to later as a part of the mass determination. Now, we focus only on equation (10).

We define the K' as

$$K' = K \cdot m_o^{-1/3}. \quad (12)$$

Then, the equation to work with is

$$\frac{\mathrm{d}v}{\mathrm{d}h} = \rho_{\mathrm{air}} K'\left(e^{-1/2\sigma\left(v_o{}^2 - v^2\right)}\right)^{-1/3} \cdot v \cdot \frac{1}{\cos z}, \quad (13)$$

with variables K' and σ.

3. Results and Discussion

3.1. Numerical Approximation. In this section, we develop a numerical approximation with the aim to describe the meteoroid flight in the atmosphere. Our goal is to obtain the solution that can be used to better understand that physical process. Subsequently, our intention is to develop a numerical approach that can be very valuable in predicting the variation of the parameters along the trajectory segments versus analytical "whole-trajectory smoothing."

Equation (13) is the expression used to find the physical parameters. To test our model, we use meteor data pertaining to the meteoroid velocity at different altitudes taken from the literature. In this regard, the accurate trajectory/velocity meteor data obtained via high-resolution Super-Schmidt cameras [58] can be utilized for a case study. These meteor trajectory data are used to optimize the procedure to obtain the values of K' and σ that fit the best the actual data points. The procedure presented here produces many synthetic curves. Subsequently, in order to optimize the computing time, a solution to make the equation converge to the real data is found.

3.1.1. The Runge–Kutta Method Implementation. The Runge–Kutta method is an iterative technique for the approximation and solution of ordinary differential equations. The method was first developed by Runge [60] and Kutta [61].

The Runge–Kutta approximation provides a solution at a determined point of altitude. Application of the Runge–Kutta method requires the initial conditions to be known:

$$y' = f(t, y) \quad ; \quad y_o \quad ; \quad t_o. \quad (14)$$

In our case, the initial conditions will be the initial velocity and the altitude of the bolide when ablation starts, "synthetically" written as

$$\frac{\mathrm{d}v}{\mathrm{d}h} = f(h, v) \quad ; \quad v(h_o) \quad ; \quad h_o. \quad (15)$$

We then need to choose a step size (p) that should be comparable with the data resolution to allow a better comparison between the model and the observations. The step size defines how many integration steps need to be implemented before the final solution is reached. The smaller the step size, the more accurate the solution will be, noting that this will also increase the computing time. The step size corresponds to the characteristic Δh that according to Bellot Rubio et al. [32] can be chosen around a few hundred of meters, 100–300 m.

Once the step size is defined, we define the model coefficients as follows:

$$\begin{aligned} l_1 &= f(t_n, y_n), \\ l_2 &= f\left(t_n + \frac{1}{2}p, y_n + p\frac{1}{2}l_1\right), \\ l_3 &= f\left(t_n + \frac{1}{2}p, y_n + p\frac{1}{2}l_2\right), \\ l_4 &= f(t_n + p, y_n + pl_3). \end{aligned} \quad (16)$$

For our case, the function to be studied is

$$f(h_n, v_n) = K'\rho(h)\left(e^{-1/2\sigma\left(v_o{}^2 - v^2\right)}\right)^{-1/3} \cdot v \cdot \frac{1}{\cos z}, \quad (17)$$

and the coefficients are calculated as

$$\begin{aligned} l_1 &= f(h_n, v_n), \\ l_2 &= f\left(h_n + \frac{1}{2}p, v_n + p\frac{1}{2}l_1\right), \\ l_3 &= f\left(h_n + \frac{1}{2}p, v_n + p\frac{1}{2}l_2\right), \\ l_4 &= f(h_n + p, v_n + pl_3). \end{aligned} \quad (18)$$

Once the coefficients (equation (16)) are calculated, we compute the solution for the point y_{n+1} using the following formula:

$$y_{n+1} = y_n + \frac{1}{6} p\left(l_1 + 2l_2 + 2l_3 + l_4\right). \tag{19}$$

For our case (equation (18)), this is

$$v_{n+1} = v_n + \frac{1}{6} p\left(l_1 + 2l_2 + 2l_3 + l_4\right). \tag{20}$$

The result obtained is the solution for the point (h_{n+1}, v_{n+1}), which becomes the initial condition to find the numerical approximation for the next point. The procedure is repeated until the desired value is reached.

3.1.2. Validating the Code Using the Jacchia Catalog. Once the procedure is defined, we need to validate the code by comparing the results with the previously published data. We use a catalog of very precise photographic trajectories of meteors [58], hereafter referred to as the JVB catalog, obtained using high spatial resolution Super-Schmidt cameras. Jacchia' [58] study synthesizes the physical inferred parameters for 413 meteors between −5 and +2, 5 stellar magnitude ranges obtained during a multistation meteor network operated in the fifties and sixties in New Mexico, USA. The data provide the meteor velocity and magnitude as a function of the altitude, the derived preatmospheric velocity, the deceleration, and some additional information for the observed meteors. All JVB catalog events were named using a number. In this project, we have used the same Jacchia and Whipple [58] numbering, but included a J at the beginning for the computational reasons. For example, we later discuss meteor J8945 (listed in JVB as 8945).

Equation (13) also requires the knowledge of air density. We adopted a general model widely used in meteor studies [45], the United States (US) standard atmosphere [62]. The US standard atmosphere was originally developed in 1958 by the US Committee on Extension to the Standard Atmosphere and improved in 1976. It is a series of tables which approximate the values for atmospheric temperature, density, pressure, and other properties over a wide range of altitudes.

3.1.3. Autofitting Procedure. We have defined a way to transform the differential equation into an expression that can be iteratively computed. The aim is to find a result for which K' and σ produce the closest curve fitting to the observational data points. In order to find the best matching values, we introduce the following autofitting procedure. We start by choosing two random values of K' and σ set as initial approximation. The meteor data to be investigated include the velocity of a meteor at specified points of altitude; we compare this velocity with the velocity simulated by our code at the same altitude points. The error factor is then calculated as follows:

$$\xi = \left(v_d - v_f\left(K, \sigma\right)\right)^2, \tag{21}$$

where v_d is the velocity inferred from the measured data, and v_f is the computed velocity.

Furthermore, we introduce the increment factors for K' and σ, which are defined as ΔK and $\Delta\sigma$. Following the same procedure as earlier, we compute the error factor for

$$\begin{aligned}
&\xi = \left(v_d - v_f\left(K + \Delta K, \sigma\right)\right)^2 \quad \xi = \left(v_d - v_f\left(K - \Delta K, \sigma\right)\right)^2,\\
&\xi = \left(v_d - v_f\left(K, \sigma + \Delta\sigma\right)\right)^2 \quad \xi = \left(v_d - v_f\left(K, \sigma - \Delta\sigma\right)\right)^2,\\
&\xi = \left(v_d - v_f\left(K + \Delta K, \sigma + \Delta\sigma\right)\right)^2 \quad \xi = \left(v_d - v_f\left(K - \Delta K, \sigma - \Delta\sigma\right)\right)^2,\\
&\xi = \left(v_d - v_f\left(K + \Delta K, \sigma - \Delta\sigma\right)\right)^2 \quad \xi = \left(v_d - v_f\left(K - \Delta K, \sigma + \Delta\sigma\right)\right)^2.
\end{aligned} \tag{22}$$

In principle, we created a 2D matrix of errors. The error parameter can be shown in a table for better visualization of the algorithm (Figure 1). Once all the error values are computed, the search for the minimum value is performed, and the result is considered the new centered value for the next computation iteration.

We repeat the same procedure for the next centered value, until we reach the point where the minimum will be centered in the middle of the matrix. Consequently, the minimum error value will correspond to the sought values of K' and σ. If very small increments of K' and σ are used, the solution will be more accurate (at the cost of increased computing time). If we set large increments of K' and σ, the solution will be reached faster, but at the expense of the resolution of the solution. In order to deal with this conundrum, the code is optimized such that it is set to work with large increments of K' and σ at the beginning. Once the 'first approximation' solution is found, the code switches to smaller increments until the optimal resolution is reached.

Figure 2 shows an example of the autofitting procedure. We have chosen the J8945 meteor for the comparison with published data [32]. Other cases were studied and compared in Dergham [29]. By comparing the velocity vs. altitude graphs, it is evident that the fitting curves are very similar to the observed data.

3.1.4. Abrupt Disruption Cases. We have presented a model capable of obtaining some parameters for meteoroids. However, as previously mentioned, not all meteoroids can be studied using this particular model because if they undergo fragmentation, the results might be skewed. Bellot Rubio et al. [32] also mentioned that there are a significant number of cases in the JVB catalog that cannot be fitted, likely as a consequence of undergoing abrupt disruptions. Figure 3 shows the results of the velocity curve using our model for the case J4141. The results are also compared with that obtained by Bellot Rubio et al. [32].

Despite the difficulties to obtain well-fitting solutions for some events, it is remarkable that our model is able to identify and produce solutions for the events undergoing quasicontinuous fragmentation. A possible way to study meteoroids with abrupt fragmentation is to focus on different segments of the trajectory that do not include a

$\xi = (v_d - v_f(K + \Delta K, \sigma - \Delta\sigma))^2$	$\xi = (v_d - v_f(K + \Delta K, \sigma))^2$	$\xi = (v_d - v_f(K + \Delta K, \sigma + \Delta\sigma))^2$
$\xi = (v_d - v_f(K, \sigma - \Delta\sigma))^2$	$\xi = (v_d - v_f(K, \sigma))^2$	$\xi = (v_d - v_f(K, \sigma + \Delta\sigma))^2$
$\xi = (v_d - v_f(K - \Delta K, \sigma - \Delta\sigma))^2$	$\xi = (v_d - v_f(K - \Delta K, \sigma))^2$	$\xi = (v_d - v_f(K - \Delta K, \sigma + \Delta\sigma))^2$

$+K$ $+\sigma$

Figure 1: Basic scheme of the error matrix.

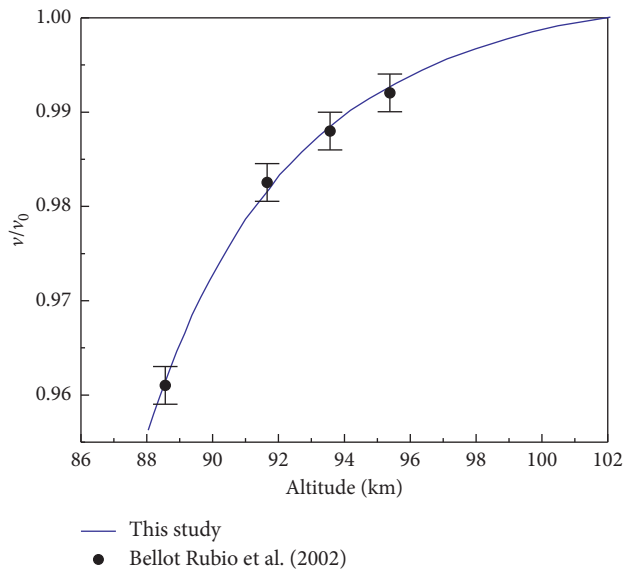

Figure 2: Normalized velocity vs. altitude fit for the meteor J8945. The result is a good fit to the previously published Figure 1 of Bellot Rubio et al. [32].

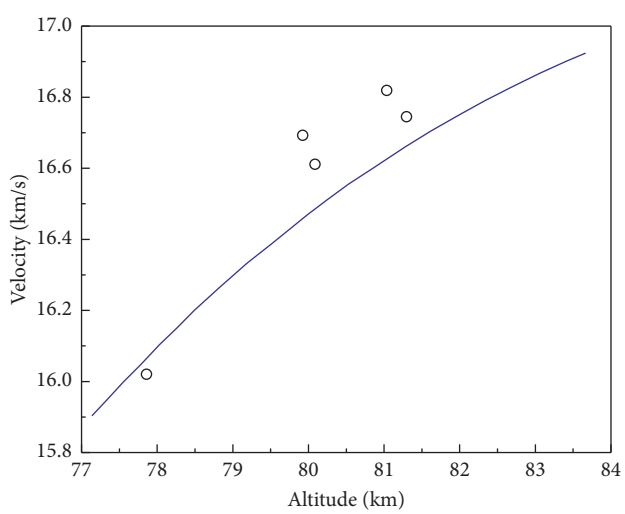

Figure 3: Comparison of results for the meteoroid J4141. The model cannot produce a well-fitting solution since this meteoroid likely suffered an abrupt disruption. This figure can be compared with that shown in Figure 1 of Bellot Rubio et al. [32].

disruption episode. We will apply that approach to the lower part of the trajectory of the Chelyabinsk bolide to demonstrate that the obtained parameters are consistent.

3.2. The Ablation Coefficient. Equation (13) has several unknowns. The ability of a meteoroid to produce light can be linked to its mass loss or the ablation coefficient σ [34, 42]. In principle, the ablation coefficient reflects how rapidly the meteoroid loses its mass as it interacts with the atmosphere. Low values of the ablation coefficient indicate that the object is losing a lesser amount of mass compared to that having a higher value of the ablation coefficient. The ablation coefficient is normally represented in units of $s^2\,km^{-2}$ and can also be expressed through the dimensionless mass loss parameter [44, 63] used through the range of meteor physics studies. The value of the ablation coefficient depends of many factors, such as chemical composition, grain size, density, porosity, and body shape, among others. In general, the values of the ablation coefficient range between 0.01 and $0.3\,s^2\,km^{-2}$ [25]. In order to exemplify this, we applied different ablation coefficients to a 1 g meteoroid with the preatmospheric velocity of 25 km/s and which starts to decelerate at the altitude of 100 km. The results are shown in Figure 4.

In general, the larger the ablation coefficient is, the faster the body decelerates due to a more rapid mass loss. Consequently, the mass of the body decreases due to ablation; this is described by using the ablation coefficient, and the drag force imposed by the atmosphere has a larger effect. Table 1 shows the comparison of our results to several events described in the JVB catalog.

3.3. Deceleration, Normalized Instantaneous Mass, and Mass Loss Rate. In this section, the effect of deceleration is examined in more detail. Given that we have the velocity as a function of altitude along the trajectory, we can study deceleration from the behavior of the velocity curve. This is particularly useful as many meteor processing algorithms and detection methods provide velocity values sequentially [15, 64]. At a certain point h_i, the code computes an increment of velocity over the increment of distance at the points immediately before and after. This can be expressed as

$$\frac{dv}{dh}(h_i) \cong \frac{\Delta v}{\Delta h} = \frac{v_{h2} - v_{h1}}{h_2 - h_1}. \tag{23}$$

Considering all the points with known velocity and altitude along the trajectory as input data, equation (23) can be applied directly. Figure 5(a) shows the velocity curve as a function of altitude for the J8945 meteoroid.

The normalized instantaneous mass (m/m_0) is the next quantity to be studied. The expression for the normalized

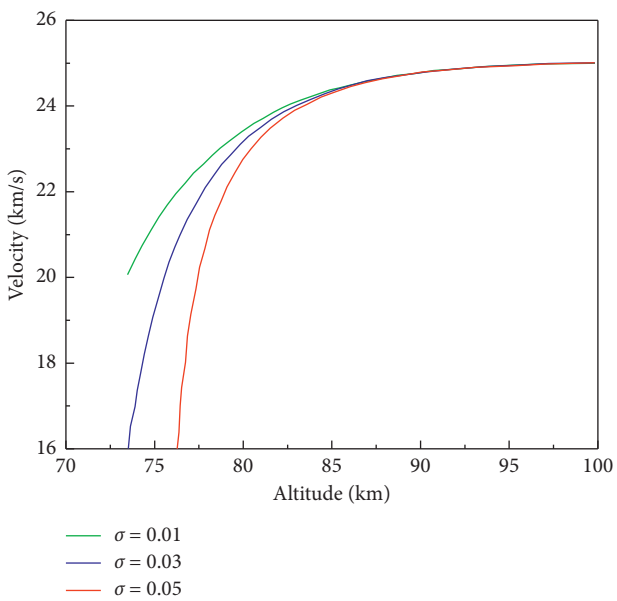

Figure 4: Comparison of meteoroids having the same initial conditions ($m_0 = 1$ g, $v_0 = 25$ km/s) but different ablation coefficients.

Table 1: Comparison of the ablation coefficients for various meteor cases from the JVB catalog.

Meteor ID	Jacchia ($s^2 \cdot km^{-2}$)	This study ($s^2 \cdot km^{-2}$)
J6882	0.0812	0.075
J6959	0.0331	0.0382
J7216	0.0501	0.079
J8945	0.0354	0.036
J9030	0.0549	0.0542
J7161	0.0354	0.0381

instantaneous mass can be derived by rearranging equation (9):

$$\frac{m}{m_o} = e^{-(1/2)\sigma\left(v_o^2 - v^2\right)}. \tag{24}$$

Equation (24) expresses the normalized instantaneous mass as a function of velocity, whereas the values of velocity are the functions of altitude. Figure 5(b) shows the behavior of normalized mass expressed as a function of altitude for the J8945 event.

We define the normalized mass loss rate as the derivative of the relative mass over the altitude. This value is computed as follows:

$$d\left[\frac{m/m_o}{h}\right] = \frac{\Delta m/m_o}{\Delta h} = \frac{m/m_{oh2} - m/m_{oh1}}{h_2 - h_1}. \tag{25}$$

Figure 5(c) shows the direct application of this approach for the J8945 event.

3.4. Application to the Chelyabinsk Superbolide. We apply the Runge–Kutta code developed in this work to the famous Chelyabinsk superbolide. On February 15, 2013, it was predicted that the NEA-2012 DA14, discovered a year prior by the Observatory Astronòmic de Mallorca, would approach the Earth within a close minimum distance of only 27700 km. However, while all the attention was focused on anticipating that encounter, another NEA unexpectedly entered the atmosphere over central Asia on February 15, 2013 at 03:20:33 UTC. The bolide disintegrated in the proximity of the city of Chelyabinsk [1]. The Chelyabinsk bolide reached the brightness magnitude of −28, which is brighter than the moon (Figure 6).

As the days passed and the orbits were calculated, scientists discarded a possible association between the two NEAs, as they presented very different heliocentric orbits. Thanks to video cameras (dash cams) found in the majority of Russian motor vehicles and surveillance cameras placed on buildings, the initial trajectory of the bolide was reconstructed and the orbit was determined [2].

After the superbolide sightings, many people uploaded various videos to Internet. Since the geographical location of the recorded videos was known, we reconstructed the bolide trajectory, obtaining the values of velocity as a function of altitude. As shown in Table 2, the data were obtained from the analysis of our video compilation, the bolide velocity along the terminal part of its trajectory just after the massive fragmentation event taking place at the altitude of 26 km. The step size was determined by the video frame rate, corresponding to differences in height of 200–150 m. Table 2 shows these data.

Figure 7(a) depicts the dynamical data after the disruption had occurred at an altitude of 26 km, and the fit is obtained by our model. The graph shows a quite uniform behavior of the Chelyabinsk superbolide after the main fragmentation event.

By studying the dynamic curve, the ablation coefficient can be obtained. The derived value is

$$\sigma = 0.034\ s^2 \cdot km^{-2}. \tag{26}$$

It is quite remarkable that this value, derived for the lower trajectory, provides a similar ablation coefficient as that for the fireballs at much higher altitudes, even though Chelyabinsk was the deepest penetrating bolide ever documented, still emitting light even as it reached the troposphere. Notably, the atmospheric density in these lower regions is about four orders of magnitude higher.

The normalized mass evolution for that lower part of the trajectory is shown in Figure 7(b), and the mass loss rate evolution is shown in Figure 7(c). In particular, it is certainly encouraging that the model predicts quite well the ablation behavior of the Chelyabinsk bolide in the lower part of its atmospheric trajectory. The light curve of the Chelyabinsk event was normalized using the US government sensor data at a peak of brightness value of 2.7 we10^{13} W s·r^{-1}, corresponding to an absolute astronomical magnitude of −28 [1]. According to the NASA JPL Chelyabinsk final report [65], the maximum brightness was achieved at an altitude of 23.3 km. This is consistent with our results as the maximum inferred value of mass loss rate from our dynamic data that occur at an altitude of ~23.5 km (Figure 7(c)).

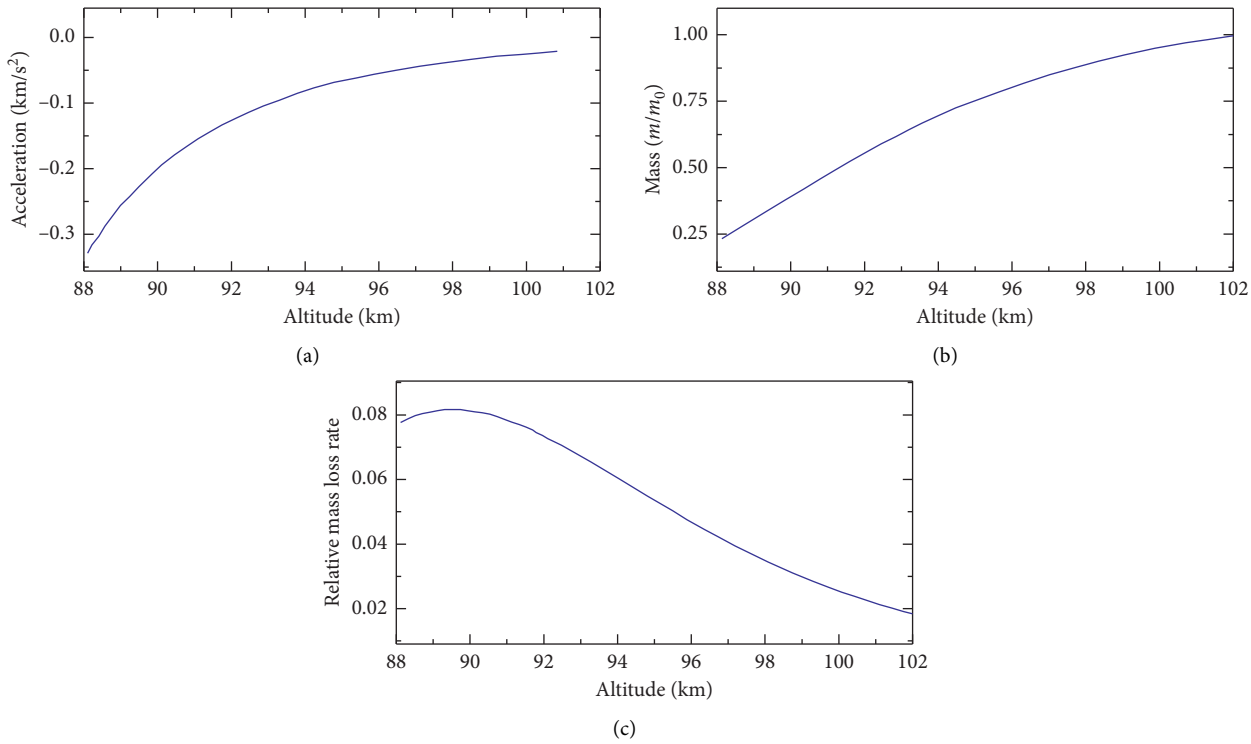

Figure 5: Curves of the acceleration (a), mass evolution (b), and relative mass loss rate (c) as a function of altitude for the meteoroid J8945.

Figure 6: A casual photograph of the Chelyabinsk bolide taken by Marat Ahmetvaleev. (a) The abrupt fragmentation at a height of 23 km is clearly distinguishable by the main flare. (b) Pictures of the dust trail by the same photographer reveal multiple paths produced by the fragments. Both pictures are courtesy of the author.

It is well known that the maximum brightness is achieved shortly after the meteoroid catastrophically breaks apart due to the fragmented/pulverized material being exposed to the heat generated by the resulting shock wave.

An interesting conclusion that can be obtained directly from these results is the importance of the atmosphere. As mentioned before, the faster the meteoroid, the more rapid the ablation process. Thus, the atmosphere could effectively shield the Earth from very fast impacts since such objects are preferentially and more quickly ablated. However, the less favorable cases are very large objects (especially if their preatmospheric velocity is low), such as the Tunguska impactor that produced an airburst over Siberia in 1908 when it entered the atmosphere at a velocity of ~30 km/s [66]. The Chelyabinsk superbolide had the preatmospheric velocity of 19 km/s, and its trajectory was consistent with a grazing geometry (high zenith angle).

To exemplify this, we have plotted the entry of the Chelyabinsk superbolide for different initial velocities (Figure 8). Of course, disrupting NEOs can produce fragments tens of meters in size. If these fragments encounter our planet under certain geometric conditions, they might become a significant source of damage on the ground and casualties. Thus, identifying the existence of asteroidal

Table 2: Dynamic data of the Chelyabinsk superbolide.

Height (km)	V (km/s)	Height (km)	v (km/s)
18.98	14.04	15.66	9.73
18.78	13.86	15.53	9.46
18.58	13.68	15.39	9.20
18.38	13.49	15.26	8.94
18.18	13.29	15.13	8.68
17.99	13.09	15.01	8.42
17.80	12.88	14.89	8.17
17.62	12.66	14.77	7.92
17.44	12.44	14.66	7.67
17.26	12.22	14.55	7.43
17.08	11.99	14.45	7.19
16.91	11.75	14.34	6.96
16.74	11.51	14.24	6.74
16.58	11.27	14.15	6.52
16.42	11.02	14.06	6.31
16.26	10.76	13.97	6.11
16.10	10.51	13.88	5.92
15.95	10.25	13.80	5.73

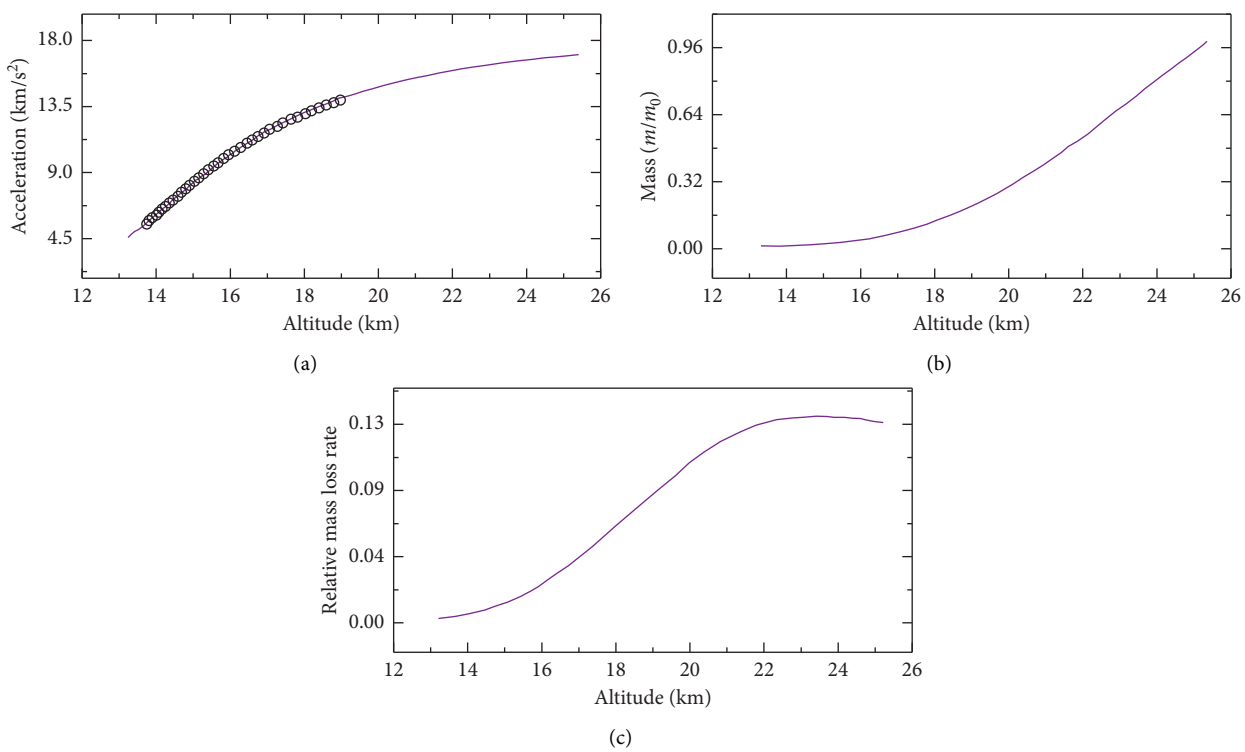

Figure 7: Velocity evolution (a), mass evolution (b), and mass loss rate (c) as a function of altitude for the Chelyabinsk superbolide.

complexes in the near-Earth environment is crucial for better assessment of impact hazard.

If the Chelyabinsk superbolide entered at a higher velocity, it would have slowed down faster due to a more rapid mass loss. According to our model, the maximum brightness of a meteoroid occurs when the mass loss reaches the peak. Consequently, the model predicts that a Chelyabinsk-like asteroid moving at a lower velocity could have more destructive potential on the Earth's surface (Figure 8). On the other hand, a projectile of the same rocky composition and moving at higher velocity could have undergone a much faster ablation process, culminating in an explosive airburst, similar to that occurring over Tunguska. Such conclusions imply that the efficiency of the Earth's atmosphere to shield us from dangerous tens of meters in size asteroids that strongly depend on the relative velocity of the encounter with our planet.

It is important to remark that new improvements in detection of fireballs from space could provide an additional progress in studying the luminous efficiency of bolides [34].

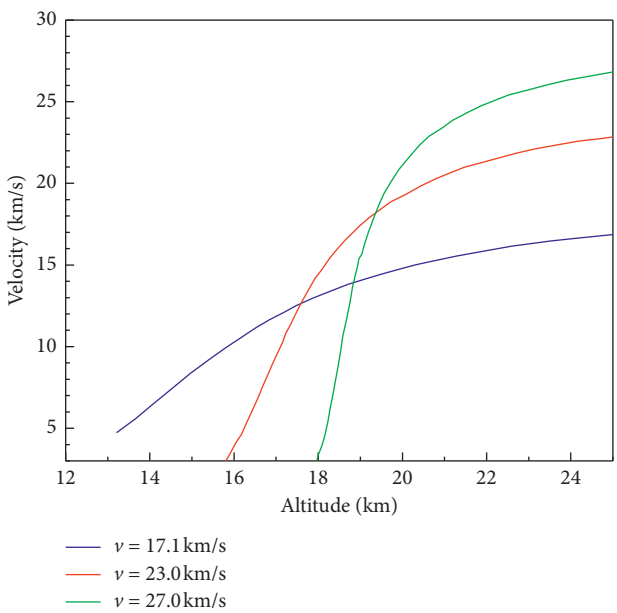

Figure 8: Simulation of the Chelyabinsk superbolide with different initial velocities ($v = 17.1$, 23, and 27 km/s).

In fact, several detections of the Chelyabinsk bolide from space have been reported [67, 68]. Future studies of common events detected from both the ground and space could constrain the role of the observing geometry in signal loss and possible biases in the subsequent determination of velocity, radiated energy, and determination of the orbital elements.

3.5. Implications for Impact Hazard. Considering the destructive nature of large extraterrestrial objects (e.g., [24]), it is crucial to identify the existence of asteroidal complexes in the near-Earth environment. Indeed, the Chelyabinsk scale or larger extraterrestrial bodies (10s of meters in size) are of special interest to the planetary defense community because depending on their orbital geometry and impact angle, these objects could pose significant hazard for humans and infrastructure on the ground. Thus, studying the near-Earth environment along with the well-documented events such as the Chelyabinsk superbolide can shed more light on the dynamic processes, as well as fundamental properties of these objects.

From the study of meteorite falls and the relative absence of small impact craters [19], we know that meter-sized asteroids are efficiently fragmented when they penetrate into the stratosphere at hypervelocity. The loading pressure in front of the body produces the rock fracture when it overcomes its tensile strength. As a natural consequence, meteorite falls often deliver tens to hundreds of stones, just after this type of break-ups [69, 70]. We have previously described such behavior when discussing the evolution of Chelyabinsk. Additionally, there is a consensual view that the terrestrial atmosphere behaves as an efficient shield for meter to 10s of meters in diameter projectiles. Despite of this, we still need to increase our statistics as more rarely, and probably for low-velocity projectiles under favorable geometric circumstances, crater excavation is still possible. A good example of this was the so-called Carancas event: an impact crater excavated in the Perú's Altiplane by a one meter-sized chondritic meteorite [71]. Being a quite unusual impact event, it is also likely that a significant number of these events are rarely studied because they happen in remote locations and remain unnoticed. It is obvious that Chelyabinsk and other well-recorded events (e.g., by fireball networks) provide an opportunity to understand in the required detail the behavior of meter-sized meteoroids and their capacity to directly cause human injuries and even casualties.

4. Conclusions

We have developed a numerical model employing the Runge–Kutta method to predict the dynamic behavior of meteoroids penetrating the Earth's atmosphere based on the meteor physics equations [39]. To test the numerical model, we successfully applied it to several meteor events described in the scientific literature. Having validated the numerical model, we studied the deceleration behavior of the Chelyabinsk superbolide in the lower part of its atmospheric trajectory, just at the region following the main fragmentation event where such an approach is applicable. This scheme represents a novel way to study complicated meteoric events by examining only the portion of the trajectory during which the object does not undergo abrupt fragmentation.

Our study of the deceleration profile of the Chelyabinsk superbolide has allowed us to reach the following conclusions:

(a) Our numerical model, successfully applied to the lower part of the fireball trajectory, predicts well the main observed characteristics of the Chelyabinsk superbolide. This is quite remarkable as the lower trajectory studied here has a similar ablation behaviour compared to fireballs at higher altitudes. It should be noted that the Chelyabinsk event is the deepest penetrating bolide ever documented, borderline emitting light as it reached the troposphere. Thus, our approach offers a promising venue in studying complex meteoric events in a streamlined and simplified manner.

(b) The best fit to the deceleration pattern provides an average ablation coefficient $\sigma = 0.034\ \mathrm{s^2{\cdot}km^{-2}}$, which is in the range of those derived in the scientific literature

(c) The ablation coefficient is considered constant within each studied trajectory interval. This simplistic approach is probably one of the reasons why this model is not applicable to the entire trajectory of the meteoroids suffering significant fragmentation and catastrophic disruptions. In any case, for the cases studied here, the ablation coefficients obtained in our work are consistent with those reported in scientific literature.

(d) A comparison of the fireball main parameters inferred from both the ground and space could constrain the role of the observing geometry in signal loss and biases in the determination of the velocity, radiated energy, and the orbital elements

(e) NEOs disrupting in the near-Earth region can produce fragments tens of meters in size, which, if encountering our planet under the right geometric circumstances, might be a significant source of hazard for humans and infrastructure on the ground. Consequently, we suggest that identifying the existence of asteroidal complexes in the near-Earth environment is crucial for a better assessment of impact hazard.

(f) Finally, we should not underestimate the hazardous potential of small asteroids as our model indicates that the ability of the Earth's atmosphere to shield us from such objects strongly depends on the relative velocity of the encounter with our planet

Data Availability

The data used to support the findings of this study are included within the article.

Conflicts of Interest

The authors declare that they have no conflicts of interest.

Acknowledgments

This research was funded by the research project (PGC2018-097374-B-I00, P.I. J.M.T-R), funded by FEDER/Ministerio de Ciencia e Innovación–Agencia Estatal de Investigación. MG acknowledges support from the Academy of Finland (325806). Research at the Ural Federal University was supported by the Russian Foundation for Basic Research (18-08-00074 and 19-05-00028). During the peer-review of this manuscript, the authors lost a mastermind, dear friend, and the co-author Esko Lyytinen. The authors dedicate this common effort in memorial to his enormous science figure and also to his friendship, insight, and understanding shared over the years. The authors thank Dr. Oleksandr Girin and two anonymous reviewers for their valuable and constructive comments. The authors also thank Marat Ahmetvaleev for providing them with the amazing pictures of the Chelyabinsk bolide and its dust trail.

References

[1] P. G. Brown, J. D. Assink, L. Astiz et al., "A 500-kiloton airburst over Chelyabinsk and an enhanced hazard from small impactors," *Nature*, vol. 503, no. 7475, pp. 238–241, 2013.

[2] J. Borovicka, P. Spurný, P. Brown et al., "The trajectory, structure and origin of the Chelyabinsk asteroidal impactor," *Nature*, vol. 503, no. 7475, pp. 235–237, 2013.

[3] I. Halliday, "Detection of a meteorite stream: observations of a second meteorite fall from the orbit of the Innisfree chondrite," *Icarus*, vol. 69, no. 3, pp. 550–556, 1987.

[4] T. J. Jopek, G. B. Valsecchi, and C. Froeschlé, "Asteroid meteoroid streams," in *Asteroids III*, W. F. Bottke Jr., A. Cellino, P. Paolicchi, and R. P. Binzel, Eds., pp. 645–652, University of Arizona Press, Tucson, AZ, USA, 2002.

[5] J. M. Trigo-Rodríguez, E. Lyytinen, D. C. Jones et al., "Asteroid 2002NY40 as source of meteorite-dropping bolides," *Monthly Notices of the Royal Astronomical Society*, vol. 382, pp. 1933–1939, 2007.

[6] J. M. Madiedo, J. M. Trigo-Rodríguez, I. P. Williams, J. L. Ortiz, and J. Cabrera, "The Northern χ-Orionid meteoroid stream and possible association with the potentially hazardous asteroid 2008XM1," *Monthly Notices of the Royal Astronomical Society*, vol. 431, no. 3, pp. 2464–2470, 2013.

[7] C. de la Fuente Marcos and R. de la Fuente Marcos, "The Chelyabinsk superbolide: a fragment of asteroid 2011 EO40," *Monthly Notices of the Royal Astronomical Society: Letters*, vol. 436, no. 1, pp. L15–L19, 2013.

[8] T. J. Jopek, G. B. Valsecchi, and C. Froeschlé, "Possible meteoroid streams associated with (69230) Hermes and 2002 SY_{50}," *Earth Moon and Planets*, vol. 95, pp. 5–10, 2004.

[9] J. Tóth, P. Vereš, and L. Kornoš, "Tidal disruption of NEAs-a case of Příbram meteorite," *Monthly Notices of the Royal Astronomical, Society*, vol. 415, no. 2, pp. 1527–1533, 2011.

[10] J. Tóth, P. Vereś, and L. Kornoš, "Tidal disruption of NEAs - a case of Příbram meteorite," *Monthly Notices of the Royal Astronomical Society*, vol. 415, no. 2, pp. 1527–1533, 2011.

[11] A. Bischoff, M. Horstmann, C. Vollmer, U. Heitmann, and S. Decker, "Chelyabinsk—not only another ordinary LL5 chondrite, but a spectacular chondrite breccia," *Meteoritics and Planetary Science*, vol. 48, 2013.

[12] T. Kohout, M. Gritsevich, V. I. Grokhovsky et al., "Mineralogy, reflectance spectra, and physical properties of the Chelyabinsk LL5 chondrite - insight into shock-induced changes in asteroid regoliths," *Icarus*, vol. 228, pp. 78–85, 2014.

[13] E. Asphaug, "Interior structures for asteroids and cometary nuclei," in *Mitigation of Hazardous Comets and Asteroids*, M. J. S. Belton, T. H. Morgan, N. Samarasinha, and D. K. Yeomans, Eds., p. 66, Cambridge University Press, Cambridge, UK, 2004.

[14] A. Terentjeva, "Fireball streams," in *Asteroids, Comets Meteors III, C.I. Lagerkvist*, H. Rickman and B. A. Lindblad, Eds., p. 579, Uppsala Astronomical Observatory, Uppsala, Sweden, 1990.

[15] I. Halliday, A. A. Griffin, and A. T. Blackwell, "Detailed data for 259 fireballs from the Canadian camera network and inferences concerning the influx of large meteoroids," *Meteoritics & Planetary Science*, vol. 31, no. 2, pp. 185–217, 1996.

[16] Z. Ceplecha, J. Borovička, W. G. Elford et al., "Meteor Phenomena and bodies," *Space Science Reviews*, vol. 84, no. 3/4, pp. 327–471, 1998.

[17] I. P. ReVelle, "The evolution of meteoroid streams," in *Meteors in the Earth's Atmosphere*, E. Murad and I. P. Williams, Eds., pp. 13–32, Cambridge University Press, Cambridge, UK, 2002.

[18] M. di Martino and A. Cellino, "Physical properties of comets and asteroids inferred from fireball observations," in *Mitigation of Hazardous Comets and Asteroids*, M. J. S. Belton, T. H. Morgan, N. Samarasinha, and D. K. Yeomans, Eds., p. 153, Cambridge University Press, Cambridge, UK, 2004.

[19] P. A. Bland and N. A. Artemieva, "Efficient disruption of small asteroids by Earth's atmosphere," *Nature*, vol. 424, no. 6946, pp. 288–291, 2003.

[20] P. Brown, D. O. ReVelle, E. A. Silber et al., "Analysis of a crater-forming meteorite impact in Peru," *Journal of Geophysical Research*, vol. 113, no. E9, p. E09007, 2008.

[21] M. I. Edwards, V. P. Stulov, and L. I. Turchak, "Consequences of collisions of natural cosmic bodies with the Earth's atmosphere and surface," *Cosmic Research*, vol. 50, no. 1, pp. 56–64, 2012.

[22] M. I. Gritsevich, V. P. Stulov, and L. I. Turchak, "Formation of large craters on the Earth as a result of impacts of natural cosmic bodies," *Doklady Physics*, vol. 58, no. 1, pp. 37–39, 2013, https://doi.org/10.1134/S1028335813010059.

[23] L. I. Turchak and M. I. Gritsevich, "Meteoroids interaction with the Earth atmosphere," *Journal of Theoretical and Applied Mechanics*, vol. 44, no. 4, pp. 15–28, 2014.

[24] M. B. E. Boslough and D. A. Crawford, "Low-altitude airbursts and the impact threat," *International Journal of Impact Engineering*, vol. 35, no. 12, pp. 1441–1448, 2008.

[25] E. A. Silber, M. Boslough, W. K. Hocking, M. Gritsevich, and R. W. Whitaker, "Physics of meteor generated shock waves in the Earth's atmosphere—a review," *Advances in Space Research*, vol. 62, no. 3, pp. 489–532, 2018.

[26] D. A. Kring, M. Boslough, and " Chelyabinsk, "Chelyabinsk: Portrait of an asteroid airburst," *Physics Today*, vol. 67, no. 9, p. 32, 2014.

[27] J. M. Trigo-Rodríguez, A. J. Castro-Tirado, J. Llorca et al., "The development of the Spanish Fireball Network using a new all-sky CCD system," *Earth, Moon Planets*, vol. 95, pp. 375–387, 2004.

[28] J. M. Trigo-Rodríguez, J. Llorca, A. J. Castro-Tirado, J. A. Docobo, and J. Fabregat, "The Spanish fireball network," *Astronomy & Geophysics*, vol. 47, no. 6, pp. 26–6, 2006.

[29] J. Dergham and J. M. Trigo-Rodríguez, "A numerical method to investigate the Ablation coefficient of the Chelyabinsk Superbolide," in *Proceedings of the Astronomical Conference Held at A.M. University*, T. J. Jopek, F. J. M. Rietmeijer, J. Watanabe, and I. P. Williams, Eds., A.M. University Press, Poznań, Poland, pp. 11–17, August 2013.

[30] J. M. Trigo-Rodríguez, J. M. Madiedo, I. P. Williams et al., "The 2011 October Draconids outburst - I. Orbital elements, meteoroid fluxes and 21P/Giacobini-Zinner delivered mass to Earth," *Monthly Notices of the Royal Astronomical Society*, vol. 433, no. 1, pp. 560–570, 2013.

[31] M. Moreno-Ibáñez, J. M. Trigo-Rodríguez, J. M. Madiedo et al., "Multi-instrumental observations of the 2014 Ursid meteor outburst," *Monthly Notices of the Royal Astronomical Society*, vol. 468, no. 2, pp. 2206–2213, 2017.

[32] L. R. Bellot-Rubio, M. J. Martínez González, L. Ruiz Herrera et al., "Modeling the photometric and dynamical behavior of Super-Schmidt meteors in the Earth's atmosphere," *Astronomy & Astrophysics*, vol. 389, no. 2, pp. 680–691, 2002.

[33] M. I. Gritsevich, T. S. Guslov, D. M. Kozhemyakina, and A. D. Novikov, "On change in the mass loss parameter along the trajectory of a meteor body," *Solar System Research*, vol. 45, no. 4, p. 336, 2011.

[34] A. Bouquet, D. Baratoux, J. Vaubaillon et al., "Simulation of the capabilities of an orbiter for monitoring the entry of interplanetary matter into the terrestrial atmosphere," *Planetary and Space Science*, vol. 103, pp. 238–249, 2014.

[35] E. K. Sansom, M. Gritsevich, H. A. R. Devillepoix et al., "Determining fireball fates using the α-β criterion," *The Astrophysical Journal*, vol. 885, no. 2, p. 7, Article ID 115, 2019.

[36] E. Lyytinen, "American Meteor Society webpage," 2013, http://www.amsmeteors.org/2013/02/large-daytime-fireball-hits-russia/.

[37] G. G. Novikov, V. N. Lebedinet, and A. V. Blokhin, "Formation of meteor tails during the quasi-continuous fragmentation of meteor bodies," *Tr. Inst. Ehksp. Meteorol. Goskomgidrometa, No. 18/119*, Atmospheric Optics, Moscow, Russia, 1986pp. 75–82, in Russian.

[38] P. B. Babadzhanov, "Fragmentation and densities of meteoroids," *Astronomy & Astrophysics*, vol. 384, no. 1, pp. 317–321, 2002.

[39] V. A. Bronshten, *Physics of Meteoric Phenomena*, Reidel Publishing Co., Dordrecht, Netherlands, 1983.

[40] B. Levin, *Physikalische Theorie der Meteore und die meteoritische Substanz im Sonnensystem*, Akademie-Verlag, Berlin, Germany, 1961.

[41] M. I. Gritsevich, "Validity of the photometric formula for estimating the mass of a fireball projectile," *Doklady Physics*, vol. 53, no. 2, pp. 97–102, 2008a.

[42] M. Gritsevich and D. Koschny, "Constraining the luminous efficiency of meteors," *Icarus*, vol. 212, no. 2, pp. 877–884, 2011.

[43] M. I. Gritsevich and V. P. Stulov, "Extra-atmospheric masses of the Canadian network bolides," *Solar System Research*, vol. 40, no. 6, pp. 477–484, 2006.

[44] M. I. Gritsevich, "Determination of parameters of meteor bodies based on flight observational data," *Advances in Space Research*, vol. 44, no. 3, pp. 323–334, 2009.

[45] E. Lyytinen and M. Gritsevich, "Implications of the atmospheric density profile in the processing of fireball observations," *Planetary and Space Science*, vol. 120, pp. 35–42, 2016.

[46] M. M. M. Meier, K. C. Welten, M. E. I. Riebe et al., "Park Forest (L5) and the asteroidal source of shocked L chondrites," *Meteoritics & Planetary Science*, vol. 52, no. 8, pp. 1561–1576, 2017.

[47] M. I. Gritsevich, V. Dmitriev, V. Vinnikov et al., "Constraining the pre-atmospheric parameters of large meteoroids: Košice, a case study," in *Assessment and Mitigation of Asteroid Impact Hazards. Astrophysics and Space Science Proceedings*, J. Trigo-Rodríguez, M. Gritsevich, and H. Palme, Eds., vol. 46, p. 153, Springer, Cham, Switzerland, 2017.

[48] J. Moilanen, M. Gritsevich, and E. Lyytinen, "Determination of strewn fields for meteorite falls," *Monthly Notices of the Royal Astronomical Society*, 2021.

[49] C. O. Johnston, E. C. Stern, and L. F. Wheeler, "Radiative heating of large meteoroids during atmospheric entry," *Icarus*, vol. 309, pp. 25–44, 2018.

[50] C. O. Johnston, E. C. Stern, and J. Borovička, "Simulating the Benešov bolide flowfield and spectrum at altitudes of 47 and 57 km," *Icarus*, vol. 354, Article ID 114037, 2021.

[51] F. Bariselli, A. Frezzotti, A. Hubin, and T. E. Magin, "Aerothermodynamic modelling of meteor entry flows," *Monthly Notices of the Royal Astronomical Society*, vol. 492, no. 2, pp. 2308–2325, 2020.

[52] B. Dias, A. Turchi, E. C. Stern, and T. E. Magin, "A model for meteoroid ablation including melting and vaporization," *Icarus*, vol. 345, p. 113710, 2020.

[53] J. M. Trigo-Rodríguez and J. Llorca, "The strength of cometary meteoroids: clues to the structure and evolution of comets," *Monthly Notices of the Royal Astronomical Society*, vol. 372, no. 2, pp. 655–660, 2006.

[54] J. M. Trigo-Rodríguez and J. Llorca, "Erratum: the strength of cometary meteoroids: clues to the structure and evolution of comets," *Monthly Notices of the Royal Astronomical Society*, vol. 375, no. 1, p. 415, 2007.

[55] J. M. Trigo-Rodríguez and J. Blum, "Tensile strength as an indicator of the degree of primitiveness of undifferentiated

bodies," *Planetary and Space Science*, vol. 57, no. 2, pp. 243–249, 2009.

[56] M. Moreno-Ibáñez, M. Gritsevich, and J. M. Trigo-Rodríguez, "New methodology to determine the terminal height of a fireball," *Icarus*, vol. 250, pp. 544–552, 2015.

[57] J. M. Trigo-Rodríguez, "The flux of meteoroids over time: meteor emission spectroscopy and the delivery of volatiles and chondritic materials to Earth," in *Hypersonic Meteoroid Entry Physics, IOP Series in Plasma Physics*, G. Colonna, M. Capitelli, and A. Laricchiuta, Eds., Institute of Physics Publishing, 2019.

[58] L. G. Jacchia and F. L. Whipple, "Precision orbits of 413 photographic meteors," *Smithsonian Contributions to Astrophysics*, vol. 4, no. 4, pp. 97–129, 1961.

[59] L. G. Jacchia, "A meteorite that missed the Earth," *Sky and Telescope*, vol. 48, p. 4, 1972.

[60] C. D. T. Runge, "Über die numerische Auflösung von Differentialgleichungen," *Mathematische Annalen*, vol. 46, no. 2, pp. 167–178, 1895.

[61] M. Kutta, "Beitrag zur näherungsweisen Integration totaler differential gleichungen," *Zeitschrift für Mathematik und Physik*, vol. 46, pp. 435–453, 1901.

[62] U.S. Government Printing Office, *U.S. Standard Atmosphere*, U.S. Government Printing Office, Washington, DC, USA, 1976.

[63] M. Moreno-Ibáñez, M. Gritsevich, J. M. Trigo-Rodríguez, and E. A. Silber, "Physically based alternative to the PE criterion for meteoroids," *Monthly Notices of the Royal Astronomical Society*, vol. 494, no. 1, pp. 316–324, 2020.

[64] M. I. Gritsevich, "The Pribram, Lost City, Innisfree, and Neuschwanstein Falls: an analysis of the atmospheric trajectories," *Solar System Research*, vol. 42, no. 5, pp. 372–390, 2008b.

[65] D. Yeomans and P. Chodas, "CNEOS JPL Homepage," 2013, https://cneos.jpl.nasa.gov/news/fireball_130301.html.

[66] Z. Sekanina, "The Tunguska event—no cometary signature in evidence," *The Astronomical Journal*, vol. 88, pp. 1382–1413, 1983.

[67] S. D. Miller, W. C. Straka III, A. S. Bachmeier, T. J. Schmit, P. T. Partain, and Y. J. Noh, "Earth-viewing satellite perspectives on the Chelyabinsk meteor event," *Proceedings of the National Academy of Sciences*, vol. 110, no. 45, pp. 18092–18097, 2013.

[68] S. R. Proud, "Reconstructing the orbit of the Chelyabinsk meteor using satellite observations," *Geophysical Research Letters*, vol. 40, no. 1, pp. 3351–3355, 2013.

[69] M. Gritsevich, V. Vinnikov, T. Kohout et al., "A comprehensive study of distribution laws for the fragments of Košice meteorite," *Meteoritics & Planetary Science*, vol. 49, no. 3, pp. 328–345, 2014.

[70] V. Vinnikov, M. Gritsevich, and L. Turchak, "Shape estimation for Košice, Almahata Sitta and bassikounou meteoroids," *Proceedings of the International Astronomical Union*, vol. 10, no. S306, pp. 394–396, 2015.

[71] G. Tancredi, J. Ishitsuka, P. H. Schultz et al., "A meteorite crater on Earth formed on September 15, 2007: the Carancas hypervelocity impact," *Meteoritics & Planetary Science*, vol. 44, no. 12, pp. 1967–1984, 2009.

[72] P. Jenniskens, *Meteor Showers and Their Parent Comets*, Cambridge University Press, Cambridge, UK, 2006.

Hindawi
Advances in Astronomy
Volume 2021, Article ID 6678056, 12 pages
https://doi.org/10.1155/2021/6678056

Research Article

Assessment of Near-Earth Asteroid Deflection Techniques via Spherical Fuzzy Sets

M. Fernández-Martínez and J. M. Sánchez-Lozano

University Centre of Defence at the Spanish Air Force Academy, MDE-UPCT, 30720–Santiago De La Ribera, Región De Murcia, Spain

Correspondence should be addressed to M. Fernández-Martínez; manuel.fernandez-martinez@cud.upct.es

Received 23 October 2020; Revised 22 January 2021; Accepted 18 February 2021; Published 8 March 2021

Academic Editor: Maria Gritsevich

Extensions of fuzzy sets to broader contexts constitute one of the leading areas of research in the context of problems in artificial intelligence. Their aim is to address decision-making problems in the real world whenever obtaining accurate and sufficient data is not a straightforward task. In this way, spherical fuzzy sets were recently introduced as a step beyond to modelize such problems more precisely on the basis of the human nature, thus expanding the space of membership levels, which are defined under imprecise circumstances. The main goal in this study is to apply the spherical fuzzy set version of Technique for Order of Preference by Similarity to Ideal Solution (TOPSIS), a well-established multicriteria decision-making approach, in the context of planetary defense. As of the extraction of knowledge from a group of experts in the field of near-Earth asteroids, they rated four deflection technologies of asteroids (kinetic impactor, ion beam deflection, enhanced gravity tractor, and laser ablation) that had been previously assessed by means of the classical theory of fuzzy series. This way, a comparative study was carried out whose most significant results are the kinetic impactor being the most suitable alternative and the spherical fuzzy set version of the TOPSIS approach behaves more sensitively than the TOPSIS procedure for triangular fuzzy sets with regard to the information provided by our group of experts.

1. Introduction

Meteoroids reach the Earth mainly as small rocks and fragile aggregates which appear as a consequence of the decay of asteroids and comets. In this way, the tiny dusts that arrive at the Earth each day amounts to a mean of approximately 100 tons [1].

Although it is true that larger objects will unlikely reach Earth's orbit, a potential impactor may dramatically affect the life and the climate in our planet. For instance, a 10 km wide impactor led to the so-called Cretaceous-Paleocene extinction that happened 64 million years ago [2, 3]. In 1908, the fragmentation at a low altitude (5–10 km) of an asteroid with an estimated diameter $d \in [30, 50]$ m destroyed around 2000 km^2 of woodland [4], what was known as the Tunguska event. Recently, in 2013, a bolide with an estimated weight of 12000 tons and an estimated diameter of 19 m entered Earth's atmosphere at a relative velocity of 19 km/s. The object broke up at an altitude of 30 km, thus injuring more than 1500 people [2, 5, 6].

The latter are clear examples of fatal consequences that impact of these kinds of objects with the Earth may result in. The impact of a single massive cosmic body might leave a fairly large crater in the surface of the Earth or induce a tsunami in the case it collides with the surface of the ocean, thus contributing to overall risk [7–10]. Furthermore, air blasts derived from destruction of meteoritic bodies in Earth's atmosphere may provoke not only falls of clouds of fragments but also major injuries on Earth's surface even if the object does not make a touchdown. Indeed, such explosions may cause from glass breakage (for air blasts greater than 15 m/s) to extreme distortions in steel structures of bridges or buildings which may lead to their collapse (for air blasts greater than 200 m/s) [11] and ([12], Table 1). Therefore, such consequences do not only depend on the size of the impactor but also on other parameters such as entry angle, velocity, density, and shape [12].

Near-Earth objects (NEOs) are asteroids or comets whose perihelion distance is less than 1.3 AU (about 195 million km). Short period comets with orbital periods less than 200 years are known as near-Earth comets (NECs) whose orbits lie far away from the Earth. In this way, researchers are mainly focused on the tracking of the near-Earth asteroids (NEAs) [2, 13].

Three key reasons that support the study of NEAs are, namely, planetary defense, scientific knowledge (e.g., deepen our solar system origins), and mining. In this regard, the current study is allocated to planetary defense.

In particular, the so-called potentially hazardous asteroids are NEAs whose minimum orbit interception distance with respect to Earth's orbit is less than 0.05 AU. They are also characterized by an estimated size greater than 140 m in diameter and an absolute magnitude not greater than 22.0, as well. Since they are able to closely approach Earth's orbit, small perturbations regarding their orbits may place them on a collision path to the Earth. As such, to perform an exhaustive tracking of these asteroids is recommended [14, 15].

Some efforts have already been made with the aim of redirecting a NEA out of a risky trajectory with the Earth', at least at a first glance. Indeed, in 2013, the NASA introduced the Asteroid Redirect Mission (ARM) with a double purpose, namely, redirect small (i.e., less than 8 m diameter) asteroids and extract small (less than 4 m) boulders from the surface of a wide asteroid and place it on a distant retrograde orbit around the moon [16]. The later could be understood as a preliminary test of the current technical capacity to deliver and catch an object to a safe environment, despite that mission did not actually consist of redirecting a small PHA. However, that technological and scientific project was cancelled in 2017 [17].

Notwithstanding, several encouraging approaches for NEA redirection have been posed, even though the technology underlying them has not yet completely developed. In this regard, we would like to highlight the Double Asteroid Redirection Test (DART) that will be the first in situ exhibition of a kinetic impactor to deflect an asteroid in space. This was formerly applied to the satellite of the binary NEA (65803) Didymos [18].

Redirecting an asteroid should be distinguished from deflecting it. In fact, deflecting an asteroid consists of modifying its trajectory to avert a potential impact with the Earth. As such, nuclear blast and kinetic impactor are examples of deflection techniques. On the other hand, the aim of redirecting an object is to induce a controlled change in its orbit with a further purpose, as it is the case of laser ablation/sublimation, tugboat, mass driver, and ion beam ([2] and references therein). However, in this study, we shall understand a deflection technology as that one being able of deflecting or redirecting an asteroid.

It is worth pointing out that, in [19], an assessment involving four deflection technologies for asteroids smaller than 250 meters in diameter (a range of sizes that covers most of the impactors with the Earth that occur in timescales up to 100000 years), i.e., kinetic impactor, ion beam deflection, enhanced gravity tractor, and laser ablation, was carried out in regard to eight criteria (build time, level of maturity of a NEA deflection technology, asteroid rotation, asteroid structure, asteroid composition, asteroid shape, active deflection duration, and mission risk). Such a decision problem was addressed throughout a combination of fuzzy logic and multicriteria decision-making (MCDM, hereafter) approaches.

We recall that a MCDM problem consists of looking for the best choice from a set of alternatives by a set of criteria, and to deal with, all that information is arranged into the so-called decision matrix [20]. A wide collection of MCDM algorithms, such as ELECTRE, OWA, VIKOR, ANP, and, PROMETHEE, can be found in the literature.

Despite MCDM methodologies had been previously applied to address several issues regarding NEAs ([20, 21]), they were first combined with fuzzy logic recently in [19], where four NEA deflection technologies (described in Section 3.2) were rated with respect to a set consisting of eight criteria (Section 3.3). The involvement of fuzzy logic therein was mainly motivated by the existence of qualitative criteria whose values are difficult to be specified or measured. In this way, linguistic labels that were associated with triangular fuzzy numbers, as well as (the valuable knowledge from) the judgments provided by an international board consisting of great standing scientists in the field of NEAs, were used to quantify the level of importance of such criteria. This way, the level of importance of each criterion was calculated, thus leading to solve the decision problem that had been posed by means of the MCDM approach named Technique for Order of Preference by Similarity to Ideal Solution (TOPSIS).

Zadeh was the first to introduce that approach to manage uncertainty and ambiguity when there exist attributes that are hard to be quantified [22]. In fuzzy logic, the level of membership of an element to a series is determined by a real number lying in the interval $[0, 1]$, thus leading to a fuzzy series. Since that pioneer work, fuzzy series have been applied not only to deal with decision problems in a wide range of contexts (e.g., [23]) but also to contribute new viewpoints in that field including intuitionistic fuzzy sets [24], Pythagorean fuzzy sets [25–28], neutrosophic fuzzy sets [29], or picture fuzzy sets [30, 31].

Extensions of fuzzy sets to broader contexts constitute one of the leading areas of research in the context of problems in computational intelligence. Their aim is to address decision-making problems in the real world whenever obtaining accurate and sufficient data is not a straightforward task. In this way, spherical fuzzy sets were recently introduced as a step beyond the picture fuzzy sets to modelize MCDM problems more precisely on the basis of the human nature, thus expanding the space of membership levels, which are defined under imprecise circumstances [32]. Even though they were introduced recently [33], it is worth mentioning that several operators, distance measures, and even some applications have already been contributed [34–38].

Being encouraged by such novel contributions, we wondered to what extent ranking of alternatives would vary if either fuzzy sets are considered to deal with a MCDM

problem or the most recent extensions of fuzzy sets (such as spherical fuzzy sets) are used with the same purpose. Following the above, this study addresses that question by applying the spherical fuzzy version of the TOPSIS approach to a decision problem that had previously been posed in the context of planetary defense [19].

The structure of this study is as follows. Section 2 contains the basics on fuzzy sets and fuzzy logic (Section 2.1), spherical fuzzy sets and their operators (Section 2.2), and also includes a description regarding the generalization of the TOPSIS approach to the context of spherical fuzzy sets (Section 2.3). The assumptions of our study are summarized in Section 3.1. Next, we recall the four NEA deflection technologies to be evaluated in this study (Section 3.2) together with the selected criteria (Section 3.3). Furthermore, some comments on the board of experts who provided us valuable information to determine the weights of the criteria are provided in Section 3.4. Our results and discussion are provided in Section 4, whereas two analyses of sensitivity are carried out and further discussed in Section 5. Finally, the main conclusions of this study are presented in Section 6.

2. Methodology

2.1. On Fuzzy Sets and Fuzzy Logic. Fuzzy logic constitutes an alternative to classical logic to deal with decision making by introducing some degree of vagueness to assess situations or objects.

In 1965, membership functions and fuzzy sets were mathematically introduced to model the level of incertitude and ambiguity in regard to human thinking [22]. In this way, the domain of a membership function turns into the unit interval $[0,1]$ rather than the set $\{0,1\}$. As such, in the context of the classical logic, the membership of an element to a set is completely determined, whereas in the fuzzy logic, such a membership could be measured gradually.

The application of fuzzy logic to real-life contexts results especially appropriate when the rules of membership of a given element to a certain class cannot be stated clearly [39]. In fact, the category itself may depend on the context.

In fuzzy logic, the level of membership of an element to a class is quantified by a real number that belongs to the interval $[0,1]$. In this way, if the membership level of an element to a certain set is close to 1, then it is more likely that such an element belongs to that class. On the contrary, if that degree of membership is close to 0, then it is more unlikely that it belongs to that set.

Let $A \subseteq U$, where U refers to a universe of discourse. A membership function can be defined as a rule of association, $\mu_A: U \longrightarrow [0,1]$, that maps every $x \in U$ to its degree of membership to A, $\mu_A(x) \in [0,1]$. Hence, the concept of a membership function can be further extended to a qualitative setting by means of linguistic labels and variables that are more accurate than crisp numbers in such contexts [40]. Reciprocally, each function $\mu: U \longrightarrow [0,1]$ allows defining a membership function that is associated to a certain fuzzy set, thus depending on the context it is applied to and the concept it represents. In this way, several functions have been widely applied including the Gaussian, the PI (or trapezoidal), and the LAMBDA (or triangular) ones.

Several extensions of ordinary fuzzy sets have appeared in the literature (e.g., [33] for a chronological tracking of them). Among them, we would like to highlight those generalizations of fuzzy sets with a three-dimensional membership function.

An intuitionistic fuzzy set is one of the form $\widetilde{A} = \left\{\langle \mu_{\widetilde{A}}(u), \nu_{\widetilde{A}}(u)\rangle : u \in U\right\}$, where $\mu_{\widetilde{A}}: U \longrightarrow [0,1]$ is the membership function that quantifies the degree of membership of each element u to $\widetilde{A}$, and $\nu_{\widetilde{A}}: U \longrightarrow [0,1]$ is the nonmembership function. They satisfy that $\mu_{\widetilde{A}}(u) + \nu_{\widetilde{A}}(u) \in [0,1]$ for all $u \in U$. In addition, $\pi_{\widetilde{A}}(u) = 1 - \mu_{\widetilde{A}}(u) - \nu_{\widetilde{A}}(u)$ is defined as the degree of hesitancy of u to $\widetilde{A}$. However, in real-life applications, it may happen that, for a certain alternative satisfying a criterion, the sum of the squares of the membership and nonmembership functions stands not greater than 1 with their sum being greater than 1. With the aim to avoid the experts modifying their preferences, the second type intuitionistic fuzzy sets were introduced by Atanassov in [41]. They are the form $\widetilde{A} = \left\{(\mu_{\widetilde{A}}(u), \nu_{\widetilde{A}}(u)) : u \in U\right\}$, where its membership function, $\mu_{\widetilde{A}}: U \longrightarrow [0,1]$, and its nonmembership function, $\nu_{\widetilde{A}}: U \longrightarrow [0,1]$, satisfy that $\mu^2_{\widetilde{A}}(u) + \nu^2_{\widetilde{A}}(u) \in [0,1]$ for all $u \in U$. In addition, the degree of hesitancy of each $u \in U$ with respect to $\widetilde{A}$ is given by the following expression:

$$\pi_{\widetilde{A}}(u) = \left(1 - \mu^2_{\widetilde{A}}(u) - \nu^2_{\widetilde{A}}(u)\right)^{1/2}. \tag{1}$$

We would like also to point out that further generalizations of the TOPSIS approach under fuzziness have been proposed in the literature on the context of interval-valued spherical fuzzy sets ([42]).

2.2. Spherical Fuzzy Sets and Operators. Going beyond, in ([33], Definition 3), the spherical fuzzy sets were first introduced to allow the hesitancy of a decision maker be defined independently of her/his degrees of membership and nonmembership in regard to an alternative with respect to a criterion. Their definition, which appears in this section, consists of using the Euclidean distance on a spherical volume rather than measuring arc distances on the surface of a sphere, as it was proposed in [43, 44].

Next, we recall how to define them. Let U be a universe of discourse. A spherical fuzzy set (SFS, hereafter) of U is a set of the form

$$\widetilde{A}_S = \left\{\langle \mu_{\widetilde{A}_S}(u), \nu_{\widetilde{A}_S}(u), \pi_{\widetilde{A}_S}(u)\rangle : \quad u \in U\right\}, \tag{2}$$

where $\mu_{\widetilde{A}_S}, \nu_{\widetilde{A}_S}$, and $\pi_{\widetilde{A}_S}: U \longrightarrow [0,1]$ are the functions that quantify the degree of membership, nonmembership, and hesitancy of each $u \in U$ to the SFS $\widetilde{A}_S$, respectively. They satisfy that $\mu^2_{\widetilde{A}_S}(u) + \nu^2_{\widetilde{A}_S}(u) + \pi^2_{\widetilde{A}_S}(u) \in [0,1]$ for all $u \in U$.

Let $\varepsilon = \langle \mu_{\widetilde{A}_S}(u), \nu_{\widetilde{A}_S}(u), \pi_{\widetilde{A}_S}(u)\rangle : u \in U$ be a spherical fuzzy number (SFN, hereafter). The product of ε by a scalar $\lambda > 0$ was defined as follows:

$$\lambda \cdot \varepsilon = \left\{ \left\langle \left(1 - \left(1 - \mu^2_{\tilde{A_S}}(u)\right)^{\lambda}\right)^{1/2}, \nu^{\lambda}_{\tilde{A_S}}(u), \left(\left(1 - \mu^2_{\tilde{A_S}}(u)\right)^{\lambda} - \left(1 - \mu^2_{\tilde{A_S}}(u) - \pi^2_{\tilde{A_S}}(u)\right)^{\lambda}\right)^{1/2} \right\rangle : \quad u \in U \right\}, \tag{3}$$

whereas the $\lambda-$ power of ε is given by

$$\varepsilon^{\lambda}_S = \left\{ \left\langle \mu^{\lambda}_{\tilde{A_S}}(u), \left(1 - \left(1 - \nu^2_{\tilde{A_S}}(u)\right)^{\lambda}\right)^{1/2}, \left(\left(1 - \nu^2_{\tilde{A_S}}(u)\right)^{\lambda} - \left(1 - \nu^2_{\tilde{A_S}}(u) - \pi^2_{\tilde{A_S}}(u)\right)^{\lambda}\right)^{1/2} \right\rangle : \quad u \in U \right\}. \tag{4}$$

([33], Definition 5). We also refer the reader to ([33], Definition 6) for some properties regarding products of SFS by scalars (with respect to $\oplus$) and powers of SFSs (with respect to the operator $\otimes$.)

On the other hand, let $\omega = (\omega_1, \omega_2, \ldots, \omega_n)$ be a normalized list of weights, i.e., $\omega_i \in [0,1]$ for all $i = 1, 2, \ldots, n$ with $\sum_{i=1}^{n} \omega_i = 1$. It is worth mentioning that several operators for SFNs were introduced in ([33], Section 3). Next, we recall the definitions of spherical weighted arithmetic mean (SWAM, ([33], Definition 7)) and spherical weighted geometric mean (SWGM, [33], Definition 8)) operators with respect to a normalized list of weights that will be used in this study. Let $\{\varepsilon_i\colon\ i = 1, \ldots, n\}$ be a finite list of triangular fuzzy numbers, where $\varepsilon_i = \langle \mu_{\tilde{A_{S_i}}}(u), \nu_{\tilde{A_{S_i}}}(u), \pi_{\tilde{A_{S_i}}}(u) \rangle$ for each $i = 1, \ldots, n$. Then,

$$\begin{aligned}
\mathrm{SWAM}_{\omega}(\varepsilon_1, \ldots, \varepsilon_n) &:= \sum_{i=1}^{n} \omega_i \varepsilon_i = \omega_1 \varepsilon_1 + \cdots + \omega_n \varepsilon_n \\
&= \left\{ \left\langle \left[1 - \prod_{i=1}^{n}\left(1 - \mu^2_{\tilde{A_{S_i}}}(u)\right)^{\omega_i}\right]^{1/2}, \prod_{i=1}^{n} \nu^{\omega_i}_{\tilde{A_{S_i}}}(u), \left[\prod_{i=1}^{n}\left(1 - \mu^2_{\tilde{A_{S_i}}}(u)\right)^{\omega_i} - \prod_{i=1}^{n}\left(1 - \mu^2_{\tilde{A_{S_i}}}(u) - \pi^2_{\tilde{A_{S_i}}}(u)\right)^{\omega_i}\right]^{1/2} \right\rangle \quad : u \in U \right\}, \\
\mathrm{SWGM}_{\omega}(\varepsilon_1, \ldots, \varepsilon_n) &:= \sum_{i=1}^{n} \varepsilon_i^{\omega_i} = \varepsilon_1^{\omega_1} + \cdots + \varepsilon_n^{\omega_n} \\
&= \left\{ \left\langle \prod_{i=1}^{n} \mu^{\omega_i}_{\tilde{A_{S_i}}}(u), \left[1 - \prod_{i=1}^{n}\left(1 - \nu^2_{\tilde{A_{S_i}}}(u)\right)^{\omega_i}\right]^{1/2}, \left[\prod_{i=1}^{n}\left(1 - \nu^2_{\tilde{A_{S_i}}}(u)\right)^{\omega_i} - \prod_{i=1}^{n}\left(1 - \nu^2_{\tilde{A_{S_i}}}(u) - \pi^2_{\tilde{A_{S_i}}}(u)\right)^{\omega_i}\right]^{1/2} \right\rangle : u \in U \right\}.
\end{aligned} \tag{5}$$

Finally, for a SFN, $\varepsilon = \langle \mu_{\tilde{A_S}}(u), \nu_{\tilde{A_S}}(u), \pi_{\tilde{A_S}}(u) \rangle\colon\ u \in U$, recall that its score was defined in the following terms ([33], Definition 9):

$$\mathrm{Score}(\varepsilon) = \left(\mu_{\tilde{A_S}}(u) - \pi_{\tilde{A_S}}(u)\right)^2 - \left(\nu_{\tilde{A_S}}(u) - \pi_{\tilde{A_S}}(u)\right)^2. \tag{6}$$

2.3. The SFS TOPSIS. Interestingly, some extensions of fuzzy sets have led to new versions of the TOPSIS approach (e.g., [33] for a literature review concerning them). In this study, we shall apply the SFS version of the TOPSIS approach (SFS TOPSIS, hereafter) that was first introduced ([33], Section 5) and already applied in the literature (e.g., [45, 46]).

First, recall that a MCDM problem can be expressed by a decision matrix whose entries contain the evaluation of the alternatives with respect to each criterion. Thus, first, let $m \geq 2$, $X = \{X_1, X_2, \ldots, X_m\}$ be a finite set of alternatives, $C = \{C_1, C_2, \ldots, C_n\}$ be a discrete set of criteria, and $\omega = (\omega_1, \omega_2, \ldots, \omega_n)$ be a normalized list of weights, i.e., $\omega_i \in [0,1]$ for all $i = 1, 2, \ldots, n$ and $\sum_{i=1}^{n} \omega_i = 1$. Then, that decision matrix constitutes the starting point to apply the SFS TOPSIS approach, which includes the following stages.

Step 1: the evaluation matrices of alternatives and criteria have to be filled in by the decision makers. With this aim, the linguistic labels that appear in Table 1 should be used.

Step 2: the judgments of the decision makers have to be aggregated by means of the SWAM (respectively, the SWGM) operator as defined above. Specifically,

Step 2.1: the individual valuations of the decision makers in regard to the relative importance of each criterion have to be combined to obtain the weights of the criteria.

Step 2.2: construction of the aggregated spherical fuzzy decision matrix by taking into account the judgments of the decision makers. In fact, let us denote the evaluation of the alternative X_i with respect to the criterion C_j by $C_j(X_i) = (\mu_{ij}, \nu_{ij}, \pi_{ij})$ for all $i = 1, \ldots, m$ and all $j = 1, \ldots, n$. Hence, let $D := (C_j(X_i))_{m \times n}$ be the decision matrix of a SFS MCDM problem.

Table 1: Linguistic terms and their associated linguistic labels and SFNs (μ, ν, π).

Linguistic term	Label	μ	ν	π
Absolutely more importance	AMI	0.9	0.1	0.1
Very high importance	VHI	0.8	0.2	0.2
High importance	HI	0.7	0.3	0.3
Slightly more importance	SMI	0.6	0.4	0.4
Equally importance	EI	0.5	0.5	0.5
Slightly low importance	SLI	0.4	0.6	0.4
Low importance	LI	0.3	0.7	0.3
Very low importance	VLI	0.2	0.8	0.2
Absolutely low importance	ALI	0.1	0.9	0.1

Step 3: construction of the aggregated weighted spherical fuzzy decision matrix. Once the alternatives have been ranked and the weights of the criteria determined, calculate $\widetilde{D} = (C_j(X_{i\omega}))_{m\times n}$, where $C_j(X_{i\omega}) = (\mu_{ij\omega}, \nu_{ij\omega}, \pi_{ij\omega})$ for all $i = 1, \ldots, m$ and all $j = 1, \ldots, n$. Notice that ([33], equation (14)) is applied in this step.

Step 4: defuzzification of the aggregated weighted spherical fuzzy decision matrix is by applying the score function (equation (6)). To tackle with, use Score $(C_j(X_{i\omega})) = (\mu_{ij\omega} - \pi_{ij\omega})^2 - (\nu_{ij\omega} - \pi_{ij\omega})^2$.

Step 5: calculation of both the Spherical Fuzzy Negative Ideal Solution (SF-NIS), denoted by X^-, and the Spherical Fuzzy Positive Ideal Solution (SF-PIS), denoted by X^+, throughout the following expressions, respectively:

$$\begin{aligned} X^- &:= \left\{\langle C_j, \min\left\{\text{Score}\left(C_j(X_{i\omega})\right): \quad i = 1, \ldots, m\right\}\rangle \quad : j = 1, \ldots, n\right\} \\ &= \left\{\langle C_j, \left(\mu_j^-, \nu_j^-, \pi_j^-\right)\rangle \quad : j = 1, \ldots, n\right\}, \\ X^* &:= \left\{\langle C_j, \max\left\{\text{Score}\left(C_j(X_{i\omega})\right) \quad : i = 1, \ldots, m\right\}\rangle \quad : j = 1, \ldots, n\right\} \\ &= \left\{\langle C_j, \left(\mu_j^*, \nu_j^*, \pi_j^*\right)\rangle \quad : j = 1, \ldots, n\right\}. \end{aligned} \tag{7}$$

Step 6: calculation of the normalized Euclidean distance ([47]) of each alternative X_i with respect to the SF-NIS (respectively, the SF-PIS) for all $i = 1, \ldots, m$ by means of the next expressions:

$$\begin{aligned} D(X_i, X^-) &= \sqrt{\frac{1}{2n}\sum_{j=1}^{n}\left[\left(\mu_{ij} - \mu_i^-\right)^2 + \left(\nu_{ij} - \nu_i^-\right)^2 + \left(\pi_{ij} - \pi_i^-\right)^2\right]}, \\ D(X_i, X^*) &= \sqrt{\frac{1}{2n}\sum_{j=1}^{n}\left[\left(\mu_{ij} - \mu_i^*\right)^2 + \left(\nu_{ij} - \nu_i^*\right)^2 + \left(\pi_{ij} - \pi_i^*\right)^2\right]}, \end{aligned} \tag{8}$$

where $C_j(X_i) = (\mu_{ij}, \nu_{ij}, \pi_{ij})$ for all $i = 1, \ldots, m$ and all $j = 1, \ldots, n$.

Step 7: calculation of the minimum distance with respect to the SF-PIS as well as the maximum distance with respect to the SF-NIS, i.e.,

$$\begin{aligned} D_{\min}(X_i, X^*) &= \min\{D(X_i, X^*): \quad i = 1, \ldots, m\}, \\ D_{\max}(X_i, X^-) &= \max\{D(X_i, X^-) \quad : i = 1, \ldots, m\}. \end{aligned} \tag{9}$$

Step 8: calculation of the closeness ratio as provided in ([33], equation (37)), thus taking the absolute value of the expression suggested in [48], namely,

$$\xi(X_i) = \frac{D(X_i, X^*)}{D_{\min}(X_i, X^+)} - \frac{D(X_i, X^-)}{D_{\max}(X_i, X^-)}, \quad \text{for all } i = 1, \ldots, m. \tag{10}$$

Step 9: list the alternatives by increasing the order of their corresponding closeness ratios. In this way, the

optimal alternative is the one that appears rated in the first position of that ranking.

3. Assessment of the NEA Deflection Technologies

3.1. Assumptions of Our Study. We would like to highlight that the primary goal in the current study is to perform a fuzzy MCDM analysis with the aim to assess the following NEA deflection technologies: kinetic impactor (KI), enhanced gravity tractor (EGT), ion-beam deflection (IBD), and laser ablation (LA). Such alternatives will be evaluated with respect to the 8 criteria that have been described in Section 3.3. Furthermore, to deal with that task, the information provided by a group of experts (Section 3.4) will allow us to calculate the aggregated relative importance of a given alternative for each criterion in terms of linguistic labels that are identified with SFNs (Section 4).

The deflection of an asteroid consists of accelerating the object just enough in such a way it crosses Earth's orbit by a minimum distance from the point the NEA would have crossed it providing that it had not been deflected.

The assumptions of our study that were disclosed to the group of experts were as follows. First, we intend to conduct a (nonnuclear) primary deflection greater than or equal to twice Earth' radii (excluding the KI) on a threatening NEA with an estimated diameter lower than or equal to 250 m. Also, the warning time was assumed to range between 5 and 30 years.

We would also like to point out that the assignment of a threatening asteroid to one of the four orbital groups (Apollos, Atens, Atiras, or Amors) has not been specifically considered in the current analysis. Alternatively, and regarding the orbital dynamics of NEAs, they have assumed those assumptions that can be found in [49] and ([50], equation (7)).

The alternatives described in ([19], Section 3.1) and the criteria appeared in ([19], Section 3.2) are also considered throughout this study. Along the next two sections, we summarize them for the sake of completeness.

3.2. Description of the Alternatives for NEA Deflection

Alternative A_1: the kinetic impactor (KI) consists of placing a spaceship on a trajectory to crash a NEA. This way, both the momentum and the velocity of the targeted asteroid would be modified [49]. It is worth mentioning that it is already possible to impact an asteroid at a high velocity as NASA's Deep Impact mission reported in 2005 [51]. According to the space science community, one of the advantages of the KI deflection technology lies in its immediate effect as well as the high level of momentum that may be delivered to the targeted asteroid. However, there is still a nonnegligible level of uncertainty regarding the amount of momentum that is effectively delivered to the NEA [52].

Alternative A_2: the technology under the ion beam deflection (IBD) mainly consists of an ion thruster on board a spacecraft (named the "shepherd") that points a highly collimated high-velocity ion beam at NEA. Simultaneously, a secondary thruster points in the opposite direction to maintain a uniform distance from the asteroid [49, 53]. In this way, a hovering distance of twice the diameter of the targeted asteroid allows leaving the gravitational force of NEA negligible [54]. Interestingly, the IBD rendezvous spacecraft may be sent to NEA beforehand, which allows decreasing the uncertainty in regard to the orbit of the asteroid. This could be understood as an advantage of the IBD with respect to the KI approach. Moreover, IBD permits an accurate retargeting of the impact point at the asteroid, which becomes especially useful in regard to large asteroids that may be deflected only a few Earth radii (except if a nuclear blast is utilized). Nevertheless, a satisfactory level of autonomy regarding the hovering of the shepherd has not yet been reached. In addition, a greater accuracy concerning the pointing of the beam still lacks [52].

Alternative A_3: enhanced gravity tractor (EGT). The gravity tractor (GT) consists of a spaceship that hovers over a targeted NEA being aimed at redirecting its trajectory by taking advantage of the gravitational attraction between the asteroid and the spacecraft. Note that the GT constitutes a trim/observer approach itself [54]. In the case of the enhanced gravity tractor (EGT), the hovering spacecraft increases its mass by removing some rocks or regolith from the targeted NEA. That amount of mass is calculated in such a way that its thrusters at full power and in the general direction of the NEA do not increase the distance between the asteroid and the spaceship. In fact, a uniform separation distance between the spacecraft and the targeted asteroid has to be preserved, so the thrusters slowly impulse the whole system in the opposite direction of the asteroid (to reduce the velocity of the NEA) or in the actual direction of the object (thus improving its velocity) [49, 55].

Alternative A_4: laser ablation (LA). The energy from the combined effects of a set of phase locked laser amplifiers is continuously impinged on NEA, thus ejecting some material away from its surface and having an effect on the velocity of the targeted asteroid [49, 54, 56].

3.3. The Selected Attributes. In this study, all the following criteria described will be evaluated by means of scales of importance that are given in terms of SFNs. With this aim, it used the information provided by our group of experts.

Attribute C_1: build time. This criterion, Tb, could be understood in the following terms:

$$\mathrm{Tb} = \text{required warning time} - \mathrm{Tr} - T, \tag{11}$$

where the required warning time is the timeframe from the discovery of the threat to the predicted date of

collision, Tr is the rendezvous time, and T is defined for each NEA deflection alternative as follows:

$$T = \begin{cases} T_1 + T_2, & \text{if the alternative is either EGT or IBD,} \\ T_1, & \text{in the case of LA,} \\ \frac{1}{3}\frac{\Delta X}{\Delta V}, & \text{if the alternative is KI.} \end{cases} \tag{12}$$

In equation (12), T_1 denotes the active deflection time, T_2 is the coasting time, ΔX denotes the required deflection distance (in m), and ΔV is the achievable velocity change (in m/s). It should be highlighted that the build time does not include the time each technology needs to achieve the TRL 6 [49]. Observe that the build time is especially important when the warning time is short which, in turn, may be produced by a significant uncertainty concerning the probability of impact of the asteroid with the Earth.

Attribute C_2: duration of the active deflection. It is the time needed to achieve a deflection of the targeted asteroid of at least twice Earth' radius (except in the case of the KI).

Attribute C_3: asteroid rotation. As it was suggested by our group of experts, it is unlikely to tackle with a fast rotator for objects with estimated diameters ranging 150–240 m.

Attribute C_4: asteroid composition. It is worth noting that the efficiency of several NEA deflection approaches may strongly depend on this criterion. For instance, LA may not work appropriately when being applied on metallic surfaces since the heat produced may be conducted away.

Attribute C_5: asteroid structure. This is related to the porosity and the internal structure of the object instead of the surface material structure of the asteroid or its friability. It should be pointed out that KI is sensitive to the internal structure of the object and its porosity, which may affect the momentum transfer. Also, it could influence the ability of EGT to collect material from the NEA surface.

Attribute C_6: asteroid shape. A great variety of irregular contours may appear in targeted NEAs.

Attribute C_7: level of maturity of a deflection technology or technological readiness level (TRL). This is a standardized scale suggested by NASA to evaluate the current level of development of a technology in regard to a desired maturity level for that approach. In this study, targeted maturity means a redirection technology for asteroids that is ready to be proved in space at the next level, which is equivalent to TRL 6 ([54]).

Attribute C_8: mission risk. It takes into account the possibility of a technological failure or an unsuccessful result regarding the asteroid deflection mission. This is quantified separately from the TRL to identify those specific risks that may appear when applying each NEA deflection technique. It is worth mentioning that a scale based on the Goddard risk matrix has been proposed to address the risk assessment ([54, 57–59]).

3.4. Our Group of Experts. A group of 10 researchers whose expertise areas include NEA deflection technologies completed the questionnaires sent by the authors, thus providing some valuable information in regard to the alternatives and criteria involved in our study. Their affiliations were as follows: Langley Research Center and Jet Propulsion Laboratory of the National Aeronautics and Space Administration (three experts), Planetary Defence Office and Galileo Mission of the European Space Agency (two experts), Institute of Space Sciences at the Spanish National Research Council, Institute for Aerospace Studies at the University of Toronto, Department of Physics Applied to Aeronautical Engineering of the Polytechnic University in Madrid, Department of Mathematics and SpaceDyS at the University of Pisa, and Laboratory of Applied Physics at the Johns Hopkins University.

4. Results and Discussion

As stated above, the scale of importance appearing in Table 1 ([33]), which identifies a set of linguistic labels with their corresponding SFNs, is considered to assess the criteria and the alternatives involved in the current study. To deal with, the information provided by our advisory board was used. In this way, Table 2 provides the weights of the criteria described in terms of SFNs via the SWAM operator.

The following order of preference regarding our set of criteria holds from the results appeared in Table 2:

$$C_1 > C_2 > C_8 > C_4 > C_7 > C_5 > C_3 > C_6. \tag{13}$$

According to equation (13), C_1 (build time) appears ranked in the first position being followed by C_2 (active deflection duration), C_8 (mission risk), C_4 (asteroid composition), C_7 (level of maturity), and C_5 (asteroid structure). Then, C_3 (asteroid rotation) and C_6 (asteroid shape) are found with a same level of importance. In this regard, a good reference to identify a set of linguistic labels with their corresponding SFNs can be found in [33].

When applying the triangular fuzzy set (TFS, hereafter) version of the analytic hierarchy process (AHP) approach ([19]), the next order of preference was found for our set of criteria by means of the valuable information provided by the group of experts:

$$C_1 > C_2 > C_7 > C_4 > C_5 > C_8 > C_6 > C_3. \tag{14}$$

Hence, from both equations (13) and (14), it holds that the criteria C_7 (level of maturity) and C_4 (asteroid composition) interchange their relative level of importance from the SWAM operator to the TFS version of AHP. Specifically, it holds that C_4 appears as a more important criterion than C_7 when applying SFS TOPSIS. It is also worth pointing out that the attribute C_8 (mission risk) has been assigned a

Table 2: Weights of the criteria in terms of SFNs.

Spherical fuzzy numbers	Weights		
Criteria	μ	ν	π
C_1 (build time)	0.8	0.2	0.2
C_2 (active deflection duration)	0.6	0.5	0.4
C_3 (asteroid rotation)	0.4	0.6	0.4
C_4 (asteroid composition)	0.6	0.4	0.4
C_5 (asteroid structure)	0.5	0.5	0.4
C_6 (asteroid shape)	0.4	0.6	0.4
C_7 (level of maturity)	0.6	0.4	0.3
C_8 (mission risk)	0.6	0.5	0.3

greater level of importance when applying the SWAM operator than TFS AHP.

The next step was to generate a new decision matrix (Table 3) that contains the assessment of the alternatives for such criteria from the judgments provided by the experts via linguistic labels defined in terms of SFNs (Table 1).

From that decision matrix and taking into account the weights of the criteria (obtained by the SWAM operator), the SFS TOPSIS methodology was applied to rank the alternatives of our case of study. In this way, Table 4 displays a comparison between the rankings provided by the SFS TOPSIS approach vs. the one obtained by means of TFS TOPSIS methodology.

The SFS TOPSIS-based ranking in Table 4 shows that the alternatives LA and EGT do interchange their positions with respect to their TFS TOPSIS rankings. This could be due to the greater SFS TOPSIS relative importance that has been assigned to the criterion C_4 (asteroid composition) to the detriment of C_7 (level of maturity). In fact, a greater valuation for that criterion (Table 3) places LA with respect to C_4, thus being followed by KI, IBD, and EGT.

Similarly, since mission risk (criterion C_8) for both alternatives LA and EGT is greater than the one for both KI and IBD, and it was the 3rd most important criterion according to SWAM operator (equation (13)), both LA and EGT become closer from KI and IBD in the SFS TOPSIS ranking.

5. Sensitivity Analyses

Two sensitivity analyses have been carried out in this section with the aim to validate the robustness of the results provided in Section 4. In fact, the first one consists of carrying out the SFS TOPSIS calculations by means of the SWGM operator and taking into account the weights of the criteria as provided by the judgments from the group of experts (Section 5.1), whereas the second sensitivity analysis repeats the SFS TOPSIS calculations by both operators, SWAM and SWGM, but assuming that the weights of all the criteria are the same. Two interesting facts follow from the results provided by each sensitivity analysis.

5.1. On the Effect of the SWGM Operator. Recall that arithmetic mean is used to aggregate the valuations provided by the experts to generate the decision matrix of the TOPSIS approach (e.g., [19]). However, when ranking the alternatives through the SFS TOPSIS procedure, we can use either the SWAM operator or the SWGM operator, which constitutes an advantage of SFSs over TFSs to deal with fuzzy series. In fact, applying geometric mean to generate the aggregated matrix of decision (by scales of importance through TFS) could provoke that the TOPSIS algorithm may not be executed.

In this section, we compare the ranking of alternatives provided by the SFS TOPSIS approach and the SWAM operator (Section 4) vs. the one provided by the SFS TOPSIS approach when the SWAM operator is applied. In both cases, the weights of the criteria were calculated according to the information provided by our group of experts. We found that both rankings of alternatives were found to be the same (Table 5), which suggests that the choice of the SWGM (respectively, the SWAM) operator does not influence the ranking positions of the alternatives. Only slight deviations were found in regard to the absolute values of the differences between the closeness ratios of pairs of consecutive alternatives. As such, the choice of one of such operators to the detriment of the other would mainly depend on the computational cost required to carry out the corresponding calculations. However, in this case, the computational cost is similar for both operators.

5.2. On the Dependence of the SFS TOPSIS Approach on the Judgments from the Group of Experts. Next, we highlight the influence of the information provided by the group of experts over our SFS TOPSIS rankings of alternatives. With this aim, a pair of SFS TOPSIS rankings was obtained (one per each operator, SWAM and SWGM) by assuming that the weights of all the criteria are the same. First, as shown in Table 6, it holds that the positions of the four alternatives involved in the present study were found to be the same in both SFS TOPSIS-based rankings. However, such SFS TOPSIS-based rankings differ from the one provided in [19], where TFS TOPSIS was used to assess these four NEA deflection technologies. In fact, the use of one of such operators (SWAM or SWGM) may lead to some changes in regard to the rankings of alternatives as provided by the SFS TOPSIS approach with respect to the rankings of alternatives provided by the TFS TOPSIS procedure.

Specifically, observe that KI keeps the first position in all such SFS TOPSIS-based rankings. On the other hand, LA is ranked in 3rd position in both SFS TOPSIS rankings when the weights of the criteria are calculated from the group of

Table 3: Assessment of the alternatives for criteria $C_1 - C_8$ in terms of SFNs as provided by the SFS TOPSIS approach via the SWAM operator.

	Criteria																							
	C_1			C_2			C_3			C_4			C_5			C_6			C_7			C_8		
Alternatives	μ	ν	π	μ	ν	π	μ	ν	π	μ	ν	π	μ	ν	π	μ	ν	π	μ	ν	π	μ	ν	π
A_1 (KI)	0.6	0.4	0.3	0.7	0.3	0.3	0.5	0.5	0.3	0.6	0.4	0.3	0.6	0.4	0.3	0.6	0.4	0.3	0.7	0.3	0.3	0.6	0.4	0.4
A_2 (IBD)	0.5	0.5	0.4	0.4	0.6	0.4	0.5	0.5	0.3	0.5	0.5	0.4	0.3	0.7	0.3	0.5	0.5	0.4	0.5	0.5	0.4	0.6	0.4	0.3
A_3 (EGT)	0.4	0.6	0.4	0.3	0.7	0.3	0.4	0.6	0.3	0.4	0.6	0.3	0.5	0.6	0.3	0.4	0.6	0.4	0.4	0.6	0.3	0.7	0.4	0.3
A_4 (LA)	0.4	0.6	0.3	0.5	0.6	0.4	0.6	0.4	0.3	0.7	0.3	0.3	0.5	0.5	0.4	0.5	0.5	0.3	0.4	0.7	0.2	0.7	0.4	0.3

Table 4: Comparison of rankings of alternatives between the SFS TOPSIS (SWAM operator) approach to TFS TOPSIS procedure ([19]). The weights of the criteria were obtained from the information provided by the group of experts.

Alternative	SFS TOPSIS (SWAM) ranking		TFS TOPSIS ranking	
	Closeness ratio	Ranking	R_i	Ranking
A_1 (KI)	0.00	1	3.07	1
A_2 (IBD)	5.39	2	1.85	2
A_3 (EGT)	7.82	4	1.16	3
A_4 (LA)	5.99	3	0.74	4

Table 5: SFS TOPSIS (SWGM) ranking of alternatives as described in the first analysis of sensitivity. The weights of the criteria were chosen to be those calculated from the information provided by the group of experts. The "Diff." column contains the differences between the closeness ratios (in absolute value) from pairs of alternatives.

SFS TOPSIS (SWGM) ranking of alternatives (criteria weights from experts)			
Alternative	Closeness ratio	Rank	Diff.
A_1 (KI)	0.00	1	–
A_2 (IBD)	3.24	2	3.24
A_3 (EGT)	4.81	4	1.57
A_4 (LA)	3.86	3	0.95

Table 6: SFS-based rankings of alternatives for both operators, SWAM and SWGM, under the assumption that the all the criteria are equally weighted (Section 5.2) vs. TFS-based ranking of alternatives for equally weighted criteria ([19]).

Alternative	SFS rankings (equally weighted criteria)		TFS ranking (equally weighted criteria)
	SWAM rank	SWGM rank	Rank
A_1 (KI)	1	1	1
A_2 (IBD)	3	3	2
A_3 (EGT)	4	4	3
A_4 (LA)	2	2	4

experts, though it appears ranked in 4th position in the TFS TOPSIS ranking for equally weighted criteria. However, it occupies 2nd position in both SFS TOPSIS rankings for equally weighted criteria. The next ranked alternatives are IBD and EGT (notice that such a consecutive order for such alternatives coincides with the one that appears in the TFS TOPSIS-based rankings).

This analysis of sensitivity highlights that, unlike the TFS TOPSIS procedure, the weights of the criteria should be assigned carefully when applying a SFS TOPSIS approach since variations regarding the weights of the criteria may induce changes of positions among the ranked alternatives.

6. Conclusions

In this section, we summarize the main conclusions to be highlighted from the study carried out.

First of all, it is worth pointing out that the KI alternative is consolidated as the best choice for active NEA deflection purposes. In fact, the results thrown by the SFS TOPSIS methodology coincide with all those presented in [19] when it was applied to the TFS TOPSIS approach with the same purpose.

However, this study highlights the fact that a SFS TOPSIS-based ranking of alternatives may vary widely when a sensitivity

analysis is carried out. Specifically, we showed that the ranking of alternatives as provided by the SFS TOPSIS approach when taking into account the information from the group of experts becomes quite different from the SFS TOPSIS ranking of alternatives we obtained provided that all the weights of the criteria are assumed to be the same. In other words, this study reveals a nonnegligible dependence of the SFS TOPSIS results from the judgments that could be provided by the group of experts with the aim of ranking a set of alternatives.

On the other hand, we would like to mention that the use of either the SWAM operator or the SWGM operator is indifferent when carrying out SFS TOPSIS calculations. In fact, only slight differences between the absolute value of the closeness ratios from pairs of consecutive alternatives were found with a similar computational cost. This fact could be understood as an advantage of SFS TOPSIS approach to the detriment of TFS TOPSIS. In fact, the latter only uses arithmetic mean in contexts where it is necessary to utilize the lowest level of the standard TFS scale of importance.

Note that a consistency analysis regarding the judgments provided by the group of experts cannot be carried out through the SWAM (respectively, the SWGM) operator. Notwithstanding, recently, it has been contributed in [60] a SFS version of the AHP methodology, which encourages us to calculate the weights of the criteria throughout that novel approach as a future research task. Also, we would like to carry out additional comparative analyses between both SFS and TFS approaches, especially to address other decision problems of astronomical interest, with the aim to investigate whether our conclusions also recur in other cases of the study.

Data Availability

The data used to support the findings of this study (i.e., the information provided by the group of experts that are filled in the questionnaires based on the methodologies applied in this work) are available from the corresponding author upon request.

Disclosure

The survey' results are based on the expert opinions of the participating individuals and do not necessarily reflect the official positions of their parent institutions.

Conflicts of Interest

The authors declare that they have no conflicts of interest.

Acknowledgments

This research has been partially funded by the research project (PGC2018-097374-B-I00), funded by FEDER/Ministerio de Ciencia e Innovación - Agencia Estatal de Investigación. M.F.M. appreciates the partial support of Ministerio de Ciencia, Innovación y Universidades, grant number PGC2018-097198-B-I00, and Fundación Séneca of Región de Murcia, grant number 20783/PI/18. J.M.S.L. acknowledges the support of Grants TIN2017-86647-P and 19882-GERM-15 from the Spanish Ministry of Economy and Competitiveness (MINECO) and Fundación Séneca (Región de Murcia), respectively. This work could have not been carried out without the generous collaboration of experts from the following institutions: Langley Research Center and Jet Propulsion Laboratory of the National Aeronautics and Space Administration (NASA), Planetary Defence Office and Galileo Mission of the European Space Agency (ESA), Laboratory of Applied Physics at the Johns Hopkins University, Institute for Aerospace Studies at the University of Toronto, Institute of Space Sciences at the Spanish National Research Council, Department of Physics Applied to Aeronautical Engineering of the Polytechnic University in Madrid, and the Department of Mathematics and SpaceDyS at the University of Pisa. The survey results are based on the expert opinions of the participating individuals and do not necessarily reflect the official positions of their parent institutions. The authors would also like to express their gratitude to the editor and anonymous reviewers whose suggestions, comments, and remarks have allowed them to enhance the quality of this paper.

References

[1] D. E. Brownlee, "The origin and properties of dust impacting the Earth," in *Accretion of Extraterrestrial Matter Throughout Earth's History*, B. Peucker-Ehrenbrink and B. Schmitz, Eds., pp. 1–12, Kluwer Academic/Plenum, New York, NY, USA, 2001.

[2] N. Anthony and M. R. Emami, "Asteroid engineering: the state-of-the-art of near-earth asteroids science and technology," *Progress in Aerospace Sciences*, vol. 100, pp. 1–17, 2018.

[3] R. A. F. Grieve, "Logan medallist 4. Large-scale impact and earth history," *Geoscience Canada*, vol. 44, no. 1, pp. 1–26, 2017.

[4] M. B. E. Boslough and D. A. Crawford, "Shoemaker-levy 9 and plume-forming collisions on earth," *Annals of the New York Academy of Sciences*, vol. 822, no. 1, pp. 236–282, 1997.

[5] S. W. Paek, O. de Weck, J. Hoffman, R. Binzel, and D. Miller, "Optimization and decision-making framework for multi-staged asteroid deflection campaigns under epistemic uncertainties," *Acta Astronautica*, vol. 167, pp. 23–41, 2020.

[6] O. P. Popova, P. Jenniskens, V. Kartashova et al., "Chelyabinsk airburst, damage assessment, meteorite recovery, and characterization," *Science*, vol. 342, no. 6162, pp. 1069–1073, 2013.

[7] M. B. E. Boslough, "Tsunami from plume-forming collisional airbursts," *IAA Planetary Defense Conference*, Sandia National Laboratories (SNL-NM), Albuquerque, NM, USA, 2013.

[8] M. I. Gritsevich, V. P. Stulov, and L. I. Turchak, "Consequences of collisions of natural cosmic bodies with the Earth's atmosphere and surface," *Cosmic Research*, vol. 50, no. 1, pp. 56–64, 2012.

[9] H. Hammel, R. Beebe, A. Ingersoll et al., "HST imaging of atmospheric phenomena created by the impact of comet shoemaker-levy 9," *Science*, vol. 267, no. 5202, pp. 1288–1296, 1995.

[10] J. G. Hills and M. P. Goda, "The fragmentation of small asteroids in the atmosphere," *The Astronomical Journal*, vol. 105, no. 3, pp. 1114–1144, 1993.

[11] S. Glasstone and P. J. Dolan, *The Effects of Nuclear Weapons*, Department of Defense, Department of Energy, Washington, DC, USA, 1977.

[12] E. A. Silber, M. Boslough, W. K. Hocking, M. Gritsevich, and R. W. Whitaker, "Physics of meteor generated shock waves in the Earth's atmosphere—a review," *Advances in Space Research*, vol. 62, no. 3, pp. 489–532, 2018.

[13] NEO Basics, *Center for Near Earth Object Studies (CNEOS)*Jet Propulsion Laboratory, California Institute of Technology and NASA, Pasadena, CA, USA, 2020, https://cneos.jpl.nasa.gov/about/neo_groups.html.

[14] N. Thiry and M. Vasile, "Statistical multi-criteria evaluation of non-nuclear asteroid deflection methods," *Acta Astronautica*, vol. 140, pp. 293–307, 2017.

[15] C. R. Chapman, "The hazard of near-Earth asteroid impacts on earth," *Earth and Planetary Science Letters*, vol. 222, no. 1, pp. 1–15, 2004.

[16] Asteroid Redirect Mission, NASA, 2020, https://www.nasa.gov/content/what-_is-_nasa-_s-_asteroid-_redirect-_mission.

[17] New Space Policy Directive Calls for Human Expansion across Solar System, 2020, https://www.nasa.gov/press-_release/new-_space-_policy-_directive-_calls-_for-_human-_expansion-_across-_solar-_system.

[18] Double Asteroid Redirection Test (DART) Mission, NASA, 2020, https://www.nasa.gov/planetarydefense/dart.

[19] J. M. Sánchez-Lozano, M. Fernández-Martínez, A. A. Saucedo-Fernández, and J. M. Trigo-Rodriguez, "Evaluation of NEA deflection techniques. A fuzzy multi-criteria decision making analysis for planetary defense," *Acta Astronautica*, vol. 176, pp. 383–397, 2020.

[20] J. M. Sánchez-Lozano, M. Fernández-Martínez, and M. T. Lamata, "Near-Earth asteroid impact dates: a reference ideal method (RIM) approach," *Engineering Applications of Artificial Intelligence*, vol. 81, pp. 157–168, 2019.

[21] J. M. Sánchez-Lozano and M. Fernández-Martínez, "Near-Earth object hazardous impact: a Multi-Criteria Decision Making approach," *Scientific Reports*, vol. 6, Article ID 37055, 2016.

[22] L. A. Zadeh, "Fuzzy sets," *Information and Control*, vol. 8, no. 3, pp. 338–353, 1965.

[23] A. Mardani, A. Jusoh, and E. K. Zavadskas, "Fuzzy multiple criteria decision-making techniques and applications—two decades review from 1994 to 2014," *Expert Systems with Applications*, vol. 42, no. 8, pp. 4126–4148, 2015.

[24] K. T. Atanassov, "Intuitionistic fuzzy sets," *Fuzzy Sets and Systems*, vol. 20, no. 1, pp. 87–96, 1986.

[25] R. R. Yager, "Pythagorean fuzzy subsets," in *Proceedings of the 2013 Joint IFSA World Congress and NAFIPS Annual Meeting (IFSA/NAFIPS)*, pp. 57–61, Edmonton, AB, Canada, June 2013.

[26] R. R. Yager, "Pythagorean membership grades in multicriteria decision making," *IEEE Transactions on Fuzzy Systems*, vol. 22, no. 4, pp. 958–965, 2014.

[27] R. R. Yager, "On the theory of bags," *International Journal of General Systems*, vol. 13, no. 1, pp. 23–37, 1986.

[28] K. Atanassov and G. Gargov, "Interval valued intuitionistic fuzzy sets," *Fuzzy Sets and Systems*, vol. 31, no. 3, pp. 343–349, 1989.

[29] F. Smarandache, *A Unifying Field in Logics: Neutrosophic Logic. Neutrosophy, Neutrosophic Set, Neutrosophic Probability and Statistics*, InfoLearnQuest, Philadelphia, PA, USA, 6th edition, 2007.

[30] S. Zeng, S. Asharf, M. Arif, and S. Abdullah, "Application of exponential jensen picture fuzzy divergence measure in multi-criteria group decision making," *Mathematics*, vol. 7, no. 2, p. 191, 2019.

[31] B. C. Cuong, "Picture fuzzy sets," *Journal of Computer Science and Cybernetics*, vol. 30, no. 4, pp. 409–420, 2014.

[32] S. Ashraf and S. Abdullah, "Spherical aggregation operators and their application in multiattribute group decision-making," *International Journal of Intelligent Systems*, vol. 34, no. 3, pp. 493–523, 2019.

[33] F. K. Gündoğdu and C. Kahraman, "Spherical fuzzy sets and spherical fuzzy TOPSIS method," *Journal of Intelligent & Fuzzy Systems*, vol. 36, no. 1, pp. 337–352, 2019.

[34] Y. Jin, S. Ashraf, and S. Abdullah, "Spherical fuzzy logarithmic aggregation operators based on entropy and their application in decision support systems," *Entropy*, vol. 21, no. 7, p. 628, 2019.

[35] S. Ashraf, S. Abdullah, M. Aslam, M. Qiyas, and M. A. Kutbi, "Spherical fuzzy sets and its representation of spherical fuzzy t-norms and t-conorms," *Journal of Intelligent & Fuzzy Systems*, vol. 36, no. 6, pp. 6089–6102, 2019.

[36] H. Jin, S. Ashraf, S. Abdullah, M. Qiyas, M. Bano, and S. Zeng, "Linguistic spherical fuzzy aggregation operators and their applications in multi-attribute decision making problems," *Mathematics*, vol. 7, no. 5, p. 413, 2019.

[37] S. Ashraf, S. Abdullah, and L. Abdullah, "Child development influence environmental factors determined using spherical fuzzy distance measures," *Mathematics*, vol. 7, no. 8, p. 661, 2019.

[38] M. Rafiq, S. Ashraf, S. Abdullah, T. Mahmood, and S. Muhammad, "The cosine similarity measures of spherical fuzzy sets and their applications in decision making," *Journal of Intelligent & Fuzzy Systems*, vol. 36, no. 6, pp. 6059–6073, 2019.

[39] J. M. Sánchez-Lozano and O. Naranjo Rodríguez, "Application of Fuzzy Reference Ideal Method (FRIM) to the military advanced training aircraft selection," *Applied Soft Computing Journal*, vol. 88, Article ID 106061, 2020.

[40] L. A. Zadeh, "The concept of a linguistic variable and its application to approximate reasoning-I," *Information Sciences*, vol. 8, no. 3, pp. 199–249, 1975.

[41] K. T. Atanassov, "Geometrical interpretation of the elements of the intuitionistic fuzzy objects, mathematical foundations of artificial intelligence seminar, Sofia," *International Journal Bioautomation*, vol. 20, no. S1, pp. S27–S42, 1989.

[42] F. K. Gündoğdu and C. Kahraman, "A novel fuzzy TOPSIS method using emerging interval-valued spherical fuzzy sets," *Engineering Applications of Artificial Intelligence*, vol. 85, pp. 307–323, 2019.

[43] Z. Gong, X. Xu, Y. Yang, Y. Zhou, and H. Zhang, "The spherical distance for intuitionistic fuzzy sets and its application in decision analysis," *Technological and Economic Development of Economy*, vol. 22, no. 3, pp. 393–415, 2016.

[44] Y. Yang and F. Chiclana, "Intuitionistic fuzzy sets: spherical representation and distances," *International Journal of Intelligent Systems*, vol. 24, no. 4, pp. 399–420, 2009.

[45] B. Oztaysi, C. Kahraman, S. C. Onar, and I. Otay, "Indoor location tracking technology evaluation by using spherial fuzzy TOPSIS method," *Developments of Artificial Intelligence Technologies in Computation and Robotics*, vol. 24, pp. 173–181, 2020.

[46] F. K. Gündoğdu and C. Kahraman, "Optimal site selection of electric vehicle charging station by using spherical fuzzy TOPSIS method," in *Decision Making with Spherical Fuzzy*

Sets. Studies in Fuzziness and Soft Computing, C. Kahraman and F. Kutlu Gündoğdu, Eds., vol. 392, Cham, Switzerland, Springer, 2021.

[47] E. Szmidt and J. Kacprzyk, "Distances between intuitionistic fuzzy sets," *Fuzzy Sets and Systems*, vol. 114, no. 3, pp. 505–518, 2000.

[48] X. Zhang and Z. Xu, "Extension of TOPSIS to multiple criteria decision making with pythagorean fuzzy sets," *International Journal of Intelligent Systems*, vol. 29, no. 12, pp. 1061–1078, 2014.

[49] C. Weisbin, W. Lincoln, B. Wilcox, J. Brophy, P. Chodas, and B. Muirhead, "Comparative analysis of asteroid-deflection approaches," in *Proceedings of the 2015 IEEE Aerospace Conference*, pp. 1–16, Big Sky, MT, USA, March 2015.

[50] T. J. Ahrens and A. W. Harris, "Deflection and fragmentation of near-Earth asteroids," *Nature*, vol. 360, no. 6403, pp. 429–433, 1992.

[51] NASA, Deep Impact Website, 2020, https://www.jpl.nasa.gov/missions/deep-_impact/.

[52] C. Bombardelli, E. J. Calero, and J. L. Gonzalo, "Deflection of fictitious asteroid 2017 PDC: ion beam vs. kinetic impactor," *Acta Astronautica*, vol. 156, pp. 301–307, 2019.

[53] C. Bombardelli and J. Peláez, "Ion beam shepherd for asteroid deflection," *Journal of Guidance, Control, and Dynamics*, vol. 34, no. 4, pp. 1270–1272, 2011.

[54] M. C. F. Bazzocchi and M. R. Emami, "Comparative analysis of redirection methods for asteroid resource exploitation," *Acta Astronautica*, vol. 120, pp. 1–19, 2016.

[55] C. R. McInnes, "Near earth object orbit modification using gravitational coupling," *Journal of Guidance, Control, and Dynamics*, vol. 30, no. 3, pp. 870–873, 2007.

[56] M. Vasile and C. A. Maddock, "Design of a formation of solar pumped lasers for asteroid deflection," *Advances in Space Research*, vol. 50, no. 7, pp. 891–905, 2012.

[57] J. R. Wertz, D. F. Everett, and J. J. Puschell, *Space Mission Engineering: The New SMAD*, Microcosm Press, Hawthorne, CA, USA, 2011.

[58] J. C. Mankins, "Technology readiness and risk assessments: a new approach," *Acta Astronautica*, vol. 65, no. 9-10, pp. 1208–1215, 2009.

[59] NASA, *Risk Management Reporting-GSFC-STD-0002, Tech. Report*, Goddard Space Flight Center, Greenbelt, MD, USA, 2009.

[60] B. Oztaysi, S. C. Onar, and C. Kahraman, "A dynamic pricing model for location based systems by using spherical fuzzy AHP scoring," *Journal of Intelligent & Fuzzy Systems*, vol. 39, no. 5, pp. 6293–6302, 2020.